

Advances in Astronomy

Recent Advances in Lunar Exploration Using Radar and Microwave Techniques

Lead Guest Editor: Jing Li

Guest Editors: Zhiguo Meng and Alexander Gusev





Recent Advances in Lunar Exploration Using Radar and Microwave Techniques

Advances in Astronomy

Recent Advances in Lunar Exploration Using Radar and Microwave Techniques

Lead Guest Editor: Jing Li

Guest Editors: Zhiguo Meng and Alexander Gusev



Copyright © 2019 Hindawi. All rights reserved.

This is a special issue published in “Advances in Astronomy.” All articles are open access articles distributed under the Creative Commons Attribution License, which permits unrestricted use, distribution, and reproduction in any medium, provided the original work is properly cited.

Editorial Board

Lorenzo Amati, Italy
Miguel De Avillez, Portugal
Damien A. Easson, USA
Elmetwally Elabbasy, Egypt
Dean Hines, USA
John Hughes, USA

Wing-Huen Ip, Taiwan
Geza Kovacs, Hungary
Michael Kueppers, Spain
Ch. C. Moustakidis, Greece
Zdzislaw E. Musielak, USA
Valery Nakariakov, UK

George Pavlov, USA
Alexei S. Pozanenko, Russia
Somak Raychaudhury, India
Wenwu Tian, China
Roberto Turolla, Italy
Yue Wang, China

Contents

Recent Advances in Lunar Exploration Using Radar and Microwave Techniques

Jing Li , Zhiguo Meng , and Alexander Gusev

Editorial (2 pages), Article ID 4794258, Volume 2019 (2019)

Structural Analysis of Lunar Regolith from LPR CH-2 Data Based on Adaptive f - x EMD: LPR Data Processed by Adaptive f - x EMD

Bin Hu , Deli Wang , Ling Zhang , and Zhaofa Zeng

Research Article (13 pages), Article ID 1528410, Volume 2019 (2019)

Several Geological Issues of Schrödinger Basin Exposed by CE-2 CELMS Data

Z. G. Meng , H. H. Wang, Y. C. Zheng , Y. Z. Wang , H. Miyamoto, Z. C. Cai, J. S. Ping, and Y. Z. Zhu

Research Article (13 pages), Article ID 3926082, Volume 2019 (2019)

Disk-Integrated Lunar Brightness Temperatures between 89 and 190 GHz

Martin J. Burgdorf , Stefan A. Buehler, Imke Hans, and Marc Prange

Research Article (8 pages), Article ID 2350476, Volume 2019 (2019)

Lunar Radiometric Measurement Based on Observing China Chang'E-3 Lander with VLBI—First Insight

SongTao Han , ZhongKai Zhang, Jing Sun, JianFeng Cao, Lue Chen, Weitao Lu, and WenXiao Li

Research Article (10 pages), Article ID 7018620, Volume 2019 (2019)

Study of Chang'E-2 Microwave Radiometer Data in the Lunar Polar Region

Fan Yang , Yi Xu , Kwing Lam Chan, Xiaoping Zhang, Guoping Hu, and Yong Li

Research Article (10 pages), Article ID 3940837, Volume 2019 (2019)

Editorial

Recent Advances in Lunar Exploration Using Radar and Microwave Techniques

Jing Li ¹, Zhiguo Meng ¹ and Alexander Gusev²

¹College of GeoExploration Science and Technology, Jilin University, Changchun 130021, China

²Kazan Federal University, Kazan, Russia

Correspondence should be addressed to Jing Li; inter.lijing@gmail.com

Received 17 June 2019; Accepted 17 June 2019; Published 7 July 2019

Copyright © 2019 Jing Li et al. This is an open access article distributed under the Creative Commons Attribution License, which permits unrestricted use, distribution, and reproduction in any medium, provided the original work is properly cited.

Since the successful launch of China's Chang'E (CE), Japan's SELENE, India's Chandrayaan, and America's LRO lunar orbiters, especially the Yutu rover onboard CE-3 mission, we have gained a further understanding about the Moon. Compared to the previous lunar missions, the microwave techniques have been paid more attention in recent mission, such as the lunar radar sounder (LRS) onboard SELENE, microwave sounder (CELMS) onboard CE-1/2, miniature synthetic aperture radar (Mini-SAR) onboard Chandrayaan, and Miniature Radio-Frequency (Mini-RF) instrument onboard LRO lunar orbiters, and the lunar penetrating radar (LPR) on board the Yutu rover in CE-3 mission. The microwave signal can penetrate the lunar regolith to some depth, and it is sensitive to the regolith thermophysical parameters. In the last five years, abundant exciting results have been revealed by the microwave data. However, the comparison among the findings using different data sources is critically absent. How to synthesize the microwave data, including the orbital and in situ measurements, to further understand the substrate thermophysical features of the Moon is one of the important research topics for the current lunar exploration. In this special issue, a few papers that address such issues are included.

11 papers were received before the deadline time. After strict review, 5 papers were accepted, and the other 6 were rejected. Prof. Li mainly sponsored 5 papers about the lunar penetration radar, Prof. Meng mainly sponsored 2 papers about the microwave observations of the Moon, and the others were processed by Prof. Gusev.

Of the 5 received papers, one addresses the structural analysis of lunar regolith from LPR CH-2 data based on

adaptive f-x empirical mode decomposition (EMD). B. Hu et al. used the adaptive f-x EMD based dip filter to extract the rock in the regolith indicating the degree of rock enrichment and highlighting regolith-basement interface. Their results locate the position of each rock and highlight the contact interface of regolith and the basement rock.

The paper "Disk-Integrated Lunar Brightness Temperatures Between 89 and 190 GHz" presents the measurements of the disk-integrated brightness temperature of the Moon at 89, 157, 183, and 190 GHz which are presented for phase angles between -80° and 50° relative to full Moon. M. J. Burgdorf et al. demonstrate the potential of weather satellites for fine-tuning models and establishing the Moon as an extremely accurate calibration reference.

In the paper "Study of the Chang'E-2 Microwave Radiometer Data in the Lunar Polar Region," F. Yang et al. used four-channel microwave radiometer (MRM) data with frequencies of 9.3 GHz, 7.8 GHz, 19.35 GHz, and 37 GHz to investigate the properties of lunar surface such as regolith thickness, dielectric constant, and titanium abundance within a depth of several meters in middle and low latitudes. The purpose of this work is to take a close look at MRM data in the polar regions of the Moon and analyze the characteristics of the brightness temperature (TB) in permanently shadowed regions (PSRs), especially where evidence of water ice has been found.

The paper "Several Geological Issues of Schrödinger Basin Exposed by CE-2 CELMS Data" evaluates the thermophysical features of Schrödinger basin using the Chang'E-2 microwave sounder (CELMS) data. Z. G. Meng et al. gave a new geological view according to the brightness temperature

and emissivity maps and proved the applicability of the CELMS data applying in high latitude regions to a certain extent.

In the paper “Lunar Radiometric Measurement Based on Observing China Chang’E-3 Lander with VLBI—First Insight,” Han et al. presented the current status and preliminary result of the OCEL, mainly focusing on the determination of the lander position. This accurate analysis is useful for optimizing OCEL sessions of the Chang’E-3 lunar lander.

Conflicts of Interest

All authors declare that there are no conflicts of interest regarding the publication of this article.

Jing Li
Zhiguo Meng
Alexander Gusev

Research Article

Structural Analysis of Lunar Regolith from LPR CH-2 Data Based on Adaptive f - x EMD: LPR Data Processed by Adaptive f - x EMD

Bin Hu ^{1,2}, Deli Wang ^{1,2}, Ling Zhang ^{1,2} and Zhaofa Zeng^{1,2}

¹College of Geo-Exploration Science and Technology, Jilin University, Changchun 130026, China

²Ministry of Land and Resources Key Laboratory of Applied Geophysics, Jilin University, Changchun 130026, China

Correspondence should be addressed to Deli Wang; wangdeli@jlu.edu.cn

Received 5 December 2018; Accepted 3 June 2019; Published 1 July 2019

Academic Editor: Michael Kueppers

Copyright © 2019 Bin Hu et al. This is an open access article distributed under the Creative Commons Attribution License, which permits unrestricted use, distribution, and reproduction in any medium, provided the original work is properly cited.

The Lunar Penetrating Radar (LPR) is one of the important scientific payloads in China's Chang'E-3 (CE-3) to image within 100 m below the lunar surface. The acquired LPR data is significant for the research of lunar geological structure. Based on the sedimentary mechanism of lunar regolith, the regolith contains many rocks with different sizes. These local anomalies appear as diffraction in LPR data, which reduces the data quality and limits the structural analysis of lunar regolith. According to the kinematics characteristics of rock caused diffraction, we transform these problems to a problem of steep dip decreasing. To reach this goal, we adopt a data preprocessing workflow to improve the quality of the radar image, firstly. Then, a dip filter based on adaptive f - x empirical mode decomposition (EMD) is proposed to extract the rocks in the regolith and the corresponding removed IMF map indicates the degree of rock enrichment and highlights regolith-basement interface. Both simulation and LPR CH-2 data present a great performance. Finally, according to the processed result, we locate the position of each rock and highlight the contact interface of regolith and the basement rock.

1. Introduction

Chang'E-3 landed at 340.4875°E, 44.1189°N on the Moon on 14 December 2013 on a new region that has not been explored before in the largest basin, the Mare Imbrium [1]. The dual-frequency Lunar Penetrating Radar aboard the Yutu Rover provides a unique opportunity to map the subsurface structure to a depth of several hundreds of metres from the low-frequency channel (CH-1, 60 MHz) and the near-surface stratigraphic structure of the regolith from the high-frequency channel (CH-2, 500 MHz). The LPR also provides an accurate detection result with high resolution from high-frequency observations [2].

LPR data processing and initial results are first presented by NAOC [3]. Initial analysis of the LPR observations, especially that from the CH-1, indicates that there are more than nine subsurface layers from the surface to a depth of ~360m [1]. The onboard Lunar Penetrating Radar conducted a 114-m-long profile, which measured a thickness of ~5 m

of the lunar regolith layer and detected three underlying basalt units at depths of 195, 215, and 345 m. The radar measurements suggest an underestimation of the global lunar regolith thickness by other methods and reveal a vast volume from the last volcanic eruption [4]. Fa et al., Lai et al., and Zhang et al. speculated the near surface structure by processing the raw CH2 data [5–7]. Dong et al. and Zhang et al. calculated the parameters of regolith [8, 9].

The previous papers mainly studied on the geological stratification and parameter inversion. The quantity and location of rocks in regolith have not been researched. The quantity and location of rocks in regolith not only help to understand the evolution of regolith on the landing site, but also provide a priori information for the further CE-5 plan of regolith collection. The rocks in lunar regolith are the break point, causing diffractions in LPR data. The kinematics characteristics of these diffractions are quite different from those of main reflections, which is expressed as hyperbola [10, 11]. The vertex position of the diffractions can

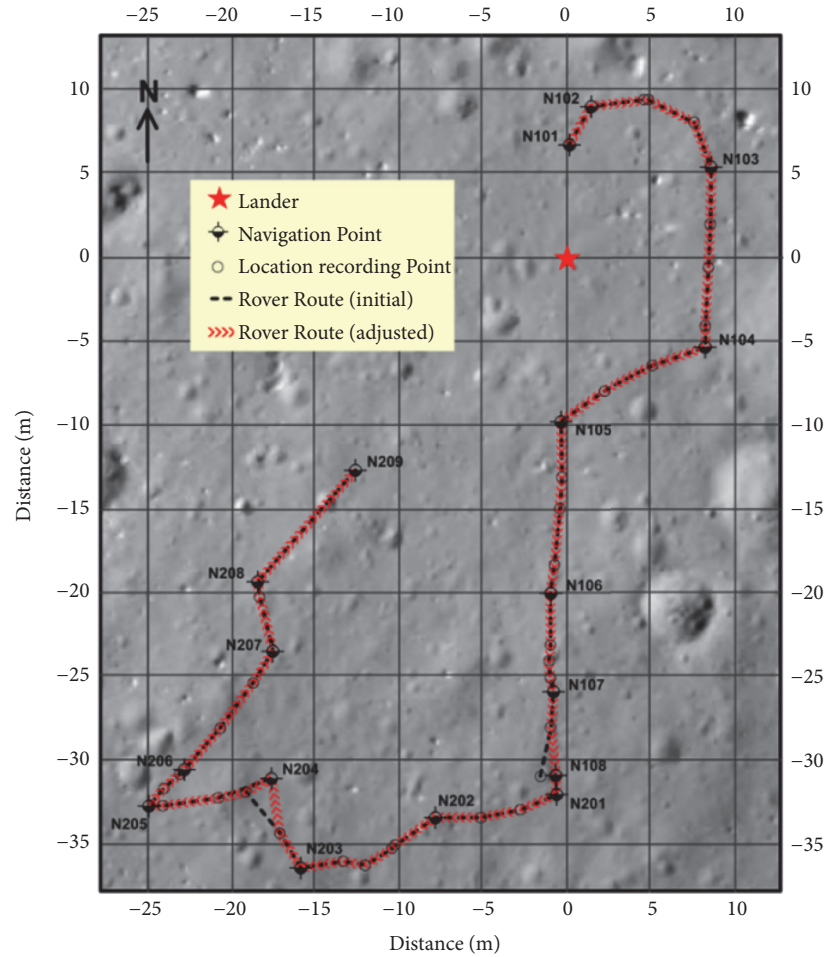


FIGURE 1: Yutu's path on the Moon. The context image was taken by the descent camera on the CE-3 lander. Red star shows the landing site. The inset lines show the initial path (black dotted line) read directly from the LPR data and the adjusted path (red line).

indicate the location of rocks. Therefore, we can suppress high wavenumber components of diffractions to locate the rock.

Huang et al. [12] use empirical mode decomposition (EMD) to prepare stable input for the Hilbert transform. The aim of EMD is stabilizing a nonstationary signal and decomposing the nonstationary signal into fast and slow oscillation components, called intrinsic mode functions (IMFs). 1D EMD can be an adaptive band-pass filter, dividing the dataset into the IMFs with different frequency range. Due to the property of EMD, Bekara and van der Baan [13] propose f - x EMD to attenuate the random and coherent noise. Cai et al. [14] propose the guideline of t - f - x EMD denoising. Chen et al. [15] add autoregressive (AR) model to f - x EMD to improve the applicable conditions and propose an EMD based dip filter. Chen et al. [16] apply randomized-order EMD to attenuate multiple reflections using randomized-order EMD. Chen et al. [17–19] introduce EMD into the framework of Seislet transform and low-rank approximation, which expanded the applications of EMD, such as signal enhancement, rank reduction, etc.

In this paper, a processing workflow is designed to image the LPR CH-2 data. Then, an adaptive f - x EMD, which can extract the rock in the regolith, is adopted. We apply the

removed IMF map as a reference in highlighted regolith-basement interface. An integrated regolith model helps to verify that this method is suitable for LPR data. Finally, according to the processed result, we locate the position of each rock and highlight the contact interface of regolith and the basement rock.

2. Data Preprocessing

Yutu Rover was released by CE-3 on 14 December 2013. The Yutu Rover explored the surface and subsurface of the landing site in the northern part of the Mare Imbrium using its four main instruments: the Panoramic Camera, Lunar Penetrating Radar (LPR), Visible–Near Infrared Spectrometer (VNIS), and Active Particle-Induced X-ray Spectrometer (APXS). Its track extends to 114.8 metres near a young crater. Figure 1 demonstrates Yutu's path on the Moon (reproduced from Bin Hu et al [20]).

The dual-frequency Lunar Penetrating Radar aboard the Yutu Rover provides a unique opportunity to map the subsurface structure to a depth of several hundreds of metres from the low-frequency channel (CH-1, 60 MHz) and the near-surface stratigraphic structure of the regolith from the

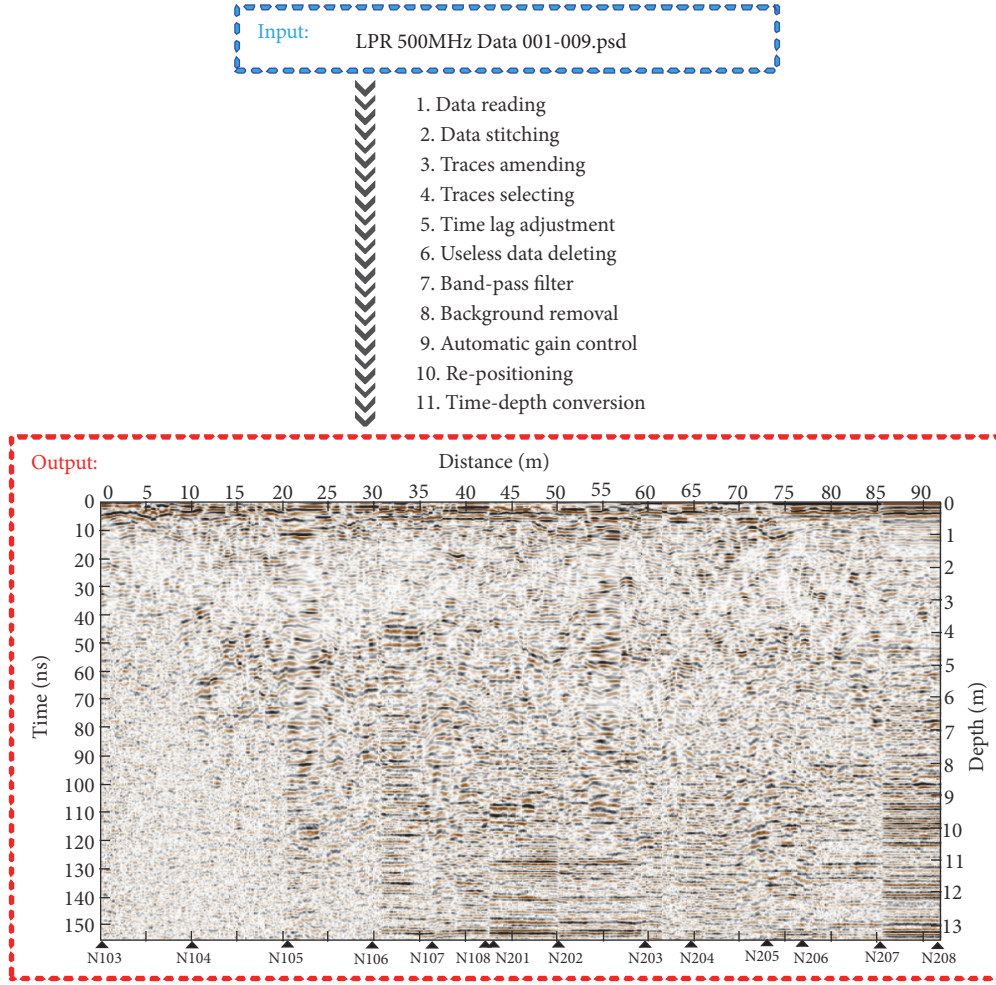


FIGURE 2: A workflow chart of CH-2 LPR data processing. The relative dielectric constant is set to be 3. N103-N209 denote the positions where the LPR was rebooted.

high-frequency channel (CH-2, 500 MHz). CH-2 data is selected to determine the near-surface stratigraphic structure of the regolith. According to the acquisition parameters, the actual situation, and the data quality, the LPR CH-2 data preprocessing workflow is designed (Figure 2). A radar image with high resolution is accessible after data preprocessing.

Analysis of the stratified structure of regolith layer and the location of each anomalous rock will help us understand the geological information of the CE-3 landing site and carry on the future lunar exploration program. However, there are some problems of the LPR data (Figure 2).

(1) The structure of the regolith layer is not clear. The current consensus is that generally the thickness of the regolith is ~ 5 m in the mare areas but the average thickness is approximately 10-15 m in older highland regions [21]. Theoretically, a uniform fine-grained regolith over an intact basement rock would produce an intense reflection, but there is nothing in LPR data.

(2) The location of each rock is not easy to determine. And the number of the rocks for each area will not be easily quantified.

Based on the above problems, it is considered that further processing is required. Adaptive f - x EMD is a reasonable approach that will help us deal with the above problems.

3. Methods

3.1. 1D t - x Domain EMD. EMD can provide an empirical decomposition of a nonstationary signal. These decomposed subsignals are separated based on oscillation frequency and called IMFs. A stable IMF has a constant instantaneous frequency and narrow-band waveform, satisfying two conditions [12]: (1) the numbers of extremes and zero crossings in the data series either are equal or differ by one, and (2) at any point, the mean value of the envelope defined by the local maxima and the local minima is zero.

In 1D case, the signal is decomposed into several subsignals $c_n(t)$ with different frequency range, which can be written as

$$s(t) = \sum_{n=1}^N c_n(t) + r(t), \quad (1)$$

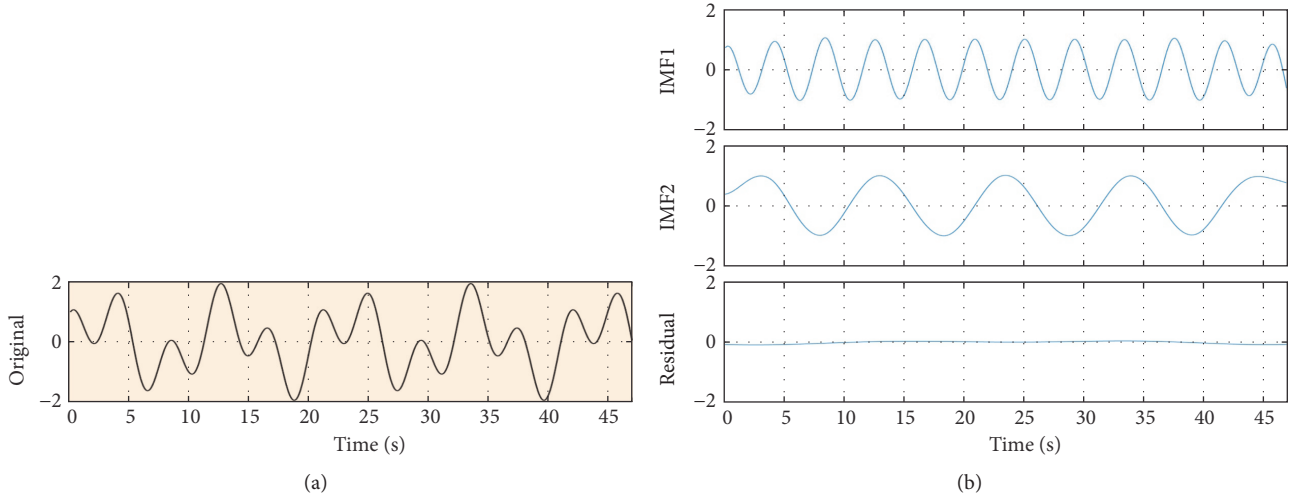


FIGURE 3: Demonstration of a decomposition using 1D EMD. (a) The synthetic signal, (b) first IMF, (c) second IMF, (d) residual.

where $s(t)$ are the input signal and $c_n(t)$ are the decomposed IMFs. $r(t)$ denotes the residual and N is the IMF number.

Figure 3 demonstrates the decomposition of a synthetic data series using EMD in t - x domain. The generated signal is the sum of two trigonometric functions (i.e., $s(t) = \cos(0.5\pi t) + \sin(0.16\pi t)$). The frequency components of the signal are 0.25 and 0.08 Hz. From Figure 3, we see that EMD successfully separates the signal into two IMFs with different frequency. Due to the advantages of frequency separation, EMD has been adopted in random noise attenuation [22, 23]. The denoising principle is the frequency difference between noise and signal, which random noise mainly locates on the high frequency components. By removing these IMFs, random noise can be attenuated.

3.2. f - x Domain EMD Based Dip Filter. Bekara and van der Baan [13] adopt EMD in f - x domain to suppress random noise and steep dip coherent noise. They consider the noise energy is dominant in the high wavenumber portion in the f - x domain. The high wavenumber portion presents the fast oscillation of each frequency slice. Based on the separation between noise and signal, noise can be attenuated by simply removing IMF1 from noisy data. The detailed process is shown as follows:

- (1) Set the size of the time window.
- (2) Pick a time window and adopt 1D forward Fourier transform along the time direction.
- (3) Pick a frequency slice and separate it into real and imaginary parts.
- (4) Compute IMF1s for real and imaginary parts and subtract them to obtain the filtered parts, respectively.
- (5) Compose the filtered frequency slice.
- (6) Repeat (4)-(5) for each frequency slice.
- (7) Adopt 1D reverse Fourier transform along the time direction.
- (8) Repeat (2)-(7) for each time window.

The two advantages of f - x EMD is convenience and stability. The f - x EMD is data-driven f - k filter and does not require the predefined muting zone in f - k domain, which is easily embedded into field data processing. Moreover, unlike convolutional operator based denoising methods (such as f - x predictive filter), f - x EMD can deal with irregular spatial sampling dataset [13, 24]. For data acquisition of LPR, irregular spatial sampling is inevitable because of the complex terrain, finite time, and expensive cost. Therefore, f - x EMD is a promising tool in LPR data processing.

It should also be noted that the choice of the removed IMFs can be more than one. It is determined by dispersion of high wavenumber components and noise level. When the target noise is located in high wavenumber components or noise level is low, the number of removed IMFs can be small. Conversely, more IMFs should be removed.

Due to the advantage of wavenumber separation, f - x EMD can be used as dip filter [15]. The different IMFs present different dip angle range; i.e., high dip components locate in the low IMFs and low dip components locate in the high IMFs. If we divide the IMF set into several subsets, the dataset is separated by the dip angle. Therefore, we define the dip filter using f - x EMD as follows:

$$\tilde{u}_i(f, x) = \begin{cases} \varepsilon_1 u_i(f, x) & i \in D_1 \\ \varepsilon_2 u_i(f, x) & i \in D_2 \\ \vdots & \vdots \\ \varepsilon_m u_i(f, x) & i \in D_m \end{cases} \quad (2)$$

$$\Lambda(f, x) = \sum_{i=1}^N \tilde{u}_i(f, x), \quad (3)$$

where $\Lambda(f, x)$ is the filtered frequency slice and $u_i(f, x)$ is the i th separated IMF. D_i is the i th dip subsets and m is the number of divided subsets. ε_i denotes the weighting factors.

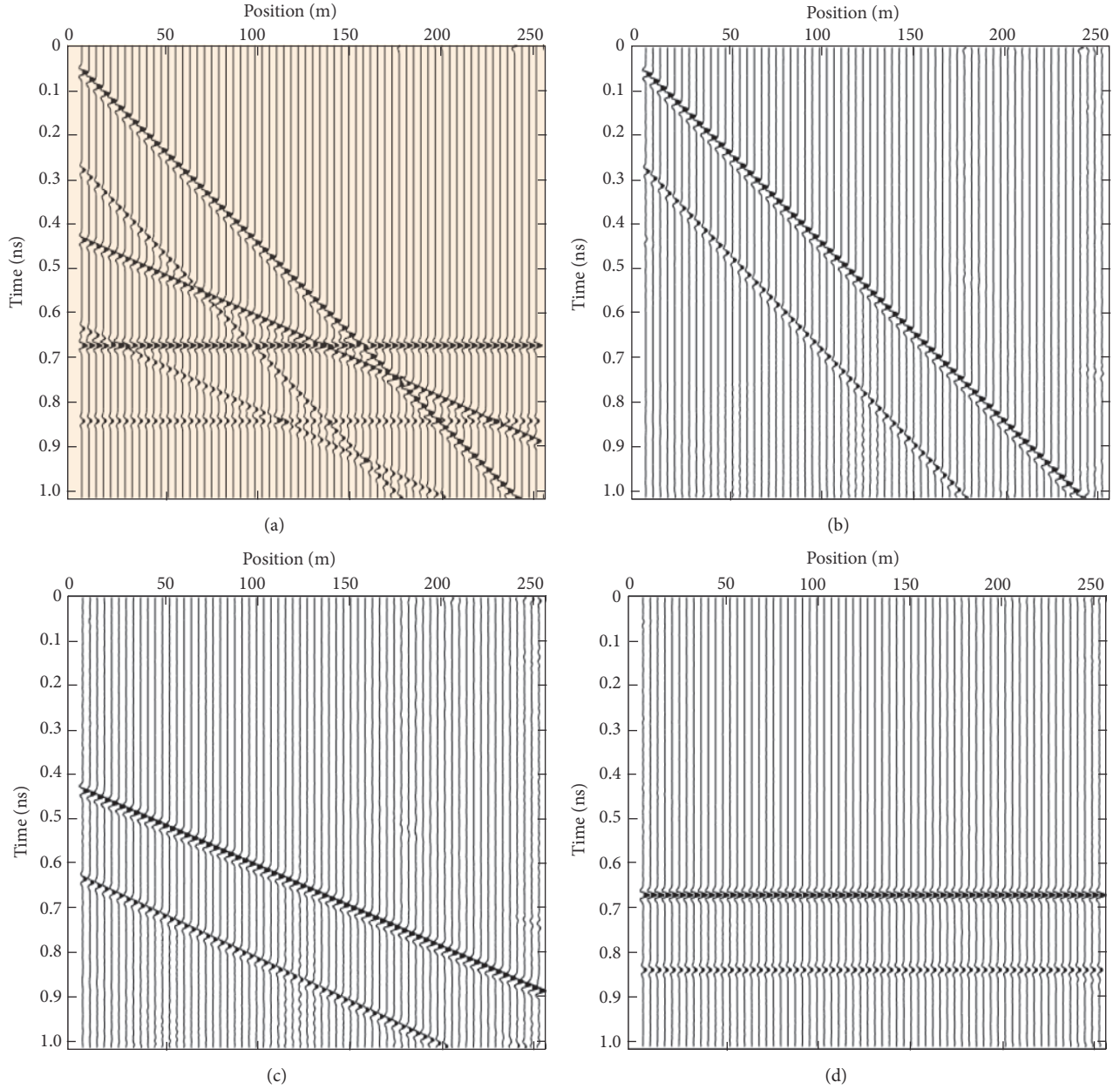


FIGURE 4: Demonstration of dip filter using f - x EMD. (a) The synthetic data, (b) high-pass dip filtered data, (c) mid-pass dip filtered data, (d) low-pass dip filtered data.

Figure 4 demonstrates the results of three types of dip filter (high-pass, mid-pass, and low-pass) working on a plane wave model (reproduced by Bin Hu et al. [20]). In the synthetic data (Figure 4(a)), it contains three dip sets. After the three dip filters, different dip events (Figures 4(b)–4(d)) are well extracted. Table 1 shows the detailed parameters of the three filter. The LPR data are acquired in constant-offset way, whose source can be considered as wave plane. The kinematics characteristics of the main reflection events are similar to those of the terrain. The rocks in lunar regolith are the break point, causing diffractions in LPR data. The kinematics characteristics of these diffractions are hyperbola. In a word, the reflection events are low dip and smooth,

whereas the diffraction events are high dip. The diffraction point extraction can be transformed into a problem of steep dip decreasing. Therefore, we should select a simple low-pass dip filter, with $m = 0$, $\varepsilon_1 = 0$, $\varepsilon_2 = 1$, $D_1 = \{1, p\}$, $D_2 = \{p + 1, \dots, N\}$. The key parameter is the number of removed IMFs p .

3.3. Adaptive f - x Domain EMD Based Dip Filter. According to the kinematics of diffractions, the goal of diffraction point extraction is to attenuate as much steep dip components as possible while maintaining the horizontal components in hyperbolic apex. Because of the complexity of rock distribution in lunar regolith, the distribution of different dip

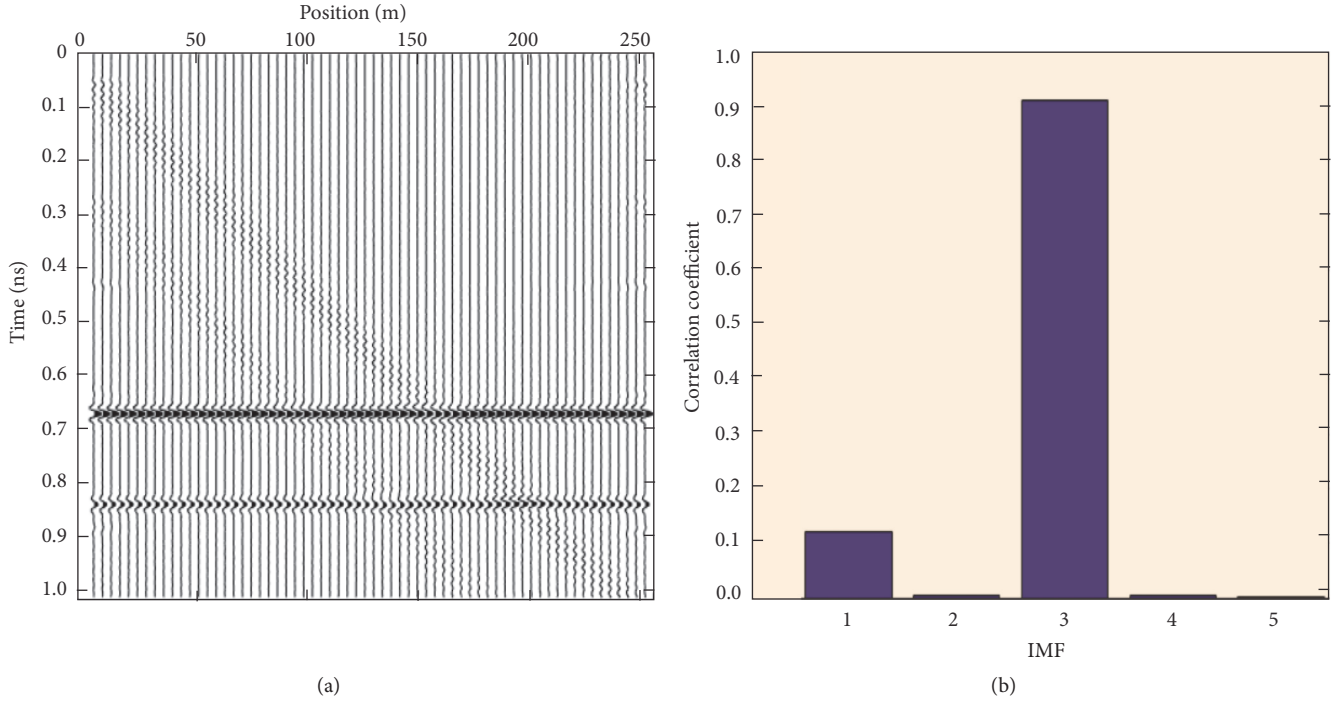


FIGURE 5: Demonstration of the choice in removing IMFs. (a) Reference dip filtered data by f - x filter, (b) correlation coefficients of different IMFs.

TABLE 1: Comparison of the SNR before and after applying the proposed approach.

Type	N	m	ε_i	D_i
High-pass	6	2	$\varepsilon_1 = 1, \varepsilon_2 = 0$	$D_1 = \{1\}, D_2 = \{2, \dots, 6\}$
Mid-pass	6	3	$\varepsilon_1 = 0, \varepsilon_2 = 1, \varepsilon_3 = 0$	$D_1 = \{1\}, D_2 = \{2\}, D_3 = \{3, \dots, 6\}$
Low-pass	6	2	$\varepsilon_1 = 0, \varepsilon_2 = 1$	$D_1 = \{1, 2\}, D_2 = \{3, \dots, 6\}$

components is various. Therefore, it is necessary to develop a method in selecting removed IMFs adaptatively.

In our method, we adopt f - k filtering result as a reference and gradually subtract smaller IMFs. After every subtraction, we calculate the correlation coefficient between subtracted IMF and reference data. The correlation coefficient r is calculated as follows:

$$r = \frac{\sum_f \sum_x (u_i(f, x) - \bar{\mathbf{u}})(d_{fk}(f, x) - \bar{\mathbf{d}})}{\sqrt{(\sum_f \sum_x (u_i(f, x) - \bar{\mathbf{u}})^2)(\sum_f \sum_x (d_{fk}(f, x) - \bar{\mathbf{d}})^2)}} \quad (4)$$

where \mathbf{u} , \mathbf{d} denote the i th IMF and the reference data in f - x domain, respectively, and $\bar{\cdot}$ denotes the mean of input data. The IMF according to the maximum of correlation coefficient present the horizontal component; then the number of removed IMF p can be defined as

$$p = i_{\max} - 1, \quad (5)$$

where i_{\max} denotes the number of IMF according to the maximum of correlation coefficient. The detailed steps are shown as follows:

- (1) Set the size of the time window and obtain rough denoised data by f - k filter.
- (2) Pick a time window and adopt 1D forward Fourier transform along the time direction.
- (3) Pick a frequency slice and separate it into real and imaginary parts.
- (4) Compute one IMF for real and imaginary parts and subtract them to obtain the filtered parts, respectively.
- (5) Compose the filtered frequency slice.
- (6) Repeat (4)-(5) for each frequency slice.
- (7) Calculate the correlation coefficient between subtracted IMF and rough denoised data in f - x domain.
- (8) Repeat (3)-(7) till finding the maximum of correlation coefficient.
- (9) Adopt 1D reverse Fourier transform along the time direction.
- (10) Repeat (2)-(7) for each time window.

Figure 5 shows the demonstration of the choice in removing IMFs. We calculated the correlation coefficients (Figure 5(b)) between the first 5 IMFs (Figure 4) and denoised data with

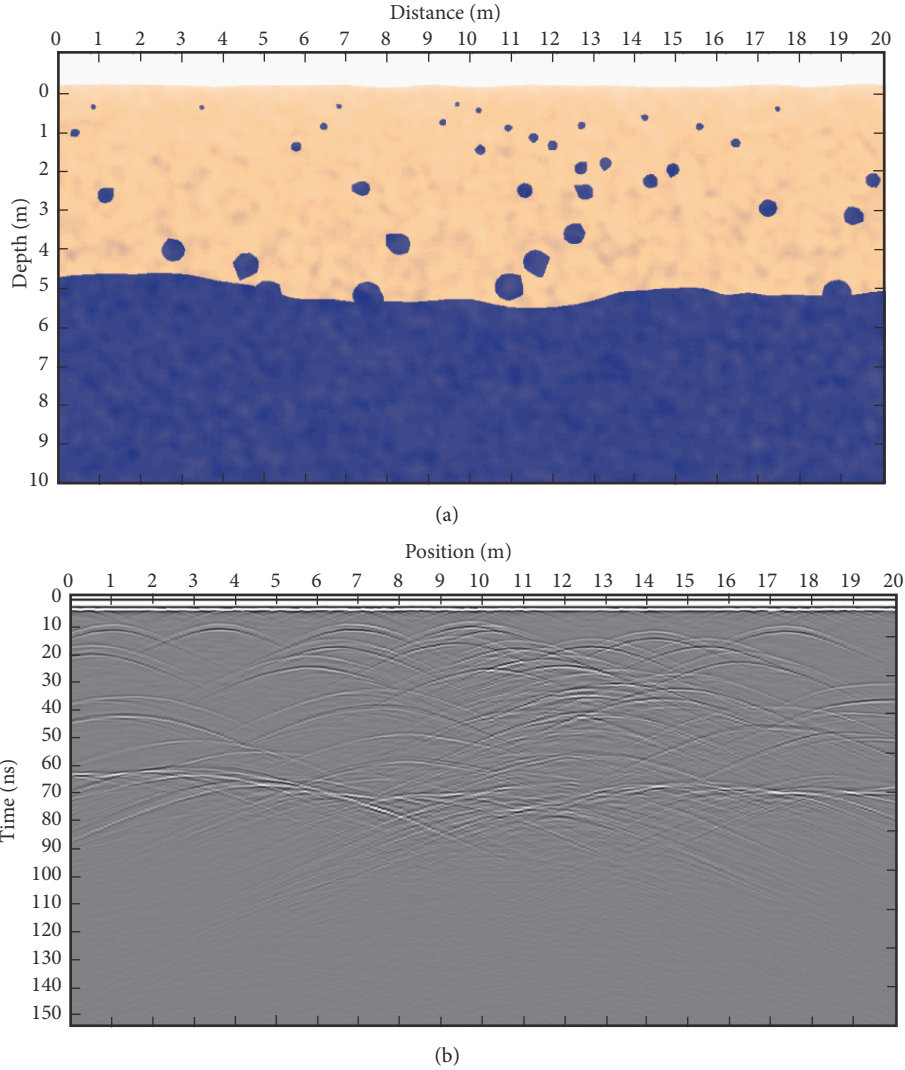


FIGURE 6: The integrated regolith model and its forward simulation result.

$f-k$ filter. We can see that correlation coefficient of IMF3 is largest; i.e., we should remove the first 2 IMFs to extract the horizontal components. We also see the correlation coefficient of IMF1 is larger than other IMFs. The reason is the high wavenumber components residual caused by $f-k$ filter. Note that the muting zone can be defined casually. The dip band divided by $f-x$ EMD is smooth and stable. The high dip components residuals or muting artefacts (red arrows) in reference data have small influence on the calculation of correlation coefficient. Compare with conventional $f-x$ EMD based dip filter; the proposed method is suitable for more complex conditions to highlight horizontal components.

4. Regolith Simulations

In order to verify whether this method is suitable for LPR data, we build a complex model (Figure 6). This model considers many factors: random medium, undulating interface, and anomalous body. The modeling method is

referenced from [25–27]. FDTD is applied for the simulation of the simple model [28]. According to the actual acquisition parameters of LPR [2], the simulated parameters are shown in Table 2. The forward result is obtained in Figure 6.

Figure 7 shows the results of the rocks extraction (left) and the map of corresponding removed IMFs number (right). Note that singularity should be taken out before using the factor to avoid local discontinuities in the extraction results. The comparison of $f-k$ spectrum (Figure 8) demonstrates the effectiveness of the proposed method, and the high-wavenumber components of the simulated data are effectively suppressed. From Figure 9, we see that the dip components are separated, and the remaining horizontal components indicate the location of the rock. Moreover, the IMFs map can reveal the degree of rock enrichment to a certain extent. The reason is that the order of the horizontal components is positively related to the complexity of the dip component, which indicates the intensity of the rock.

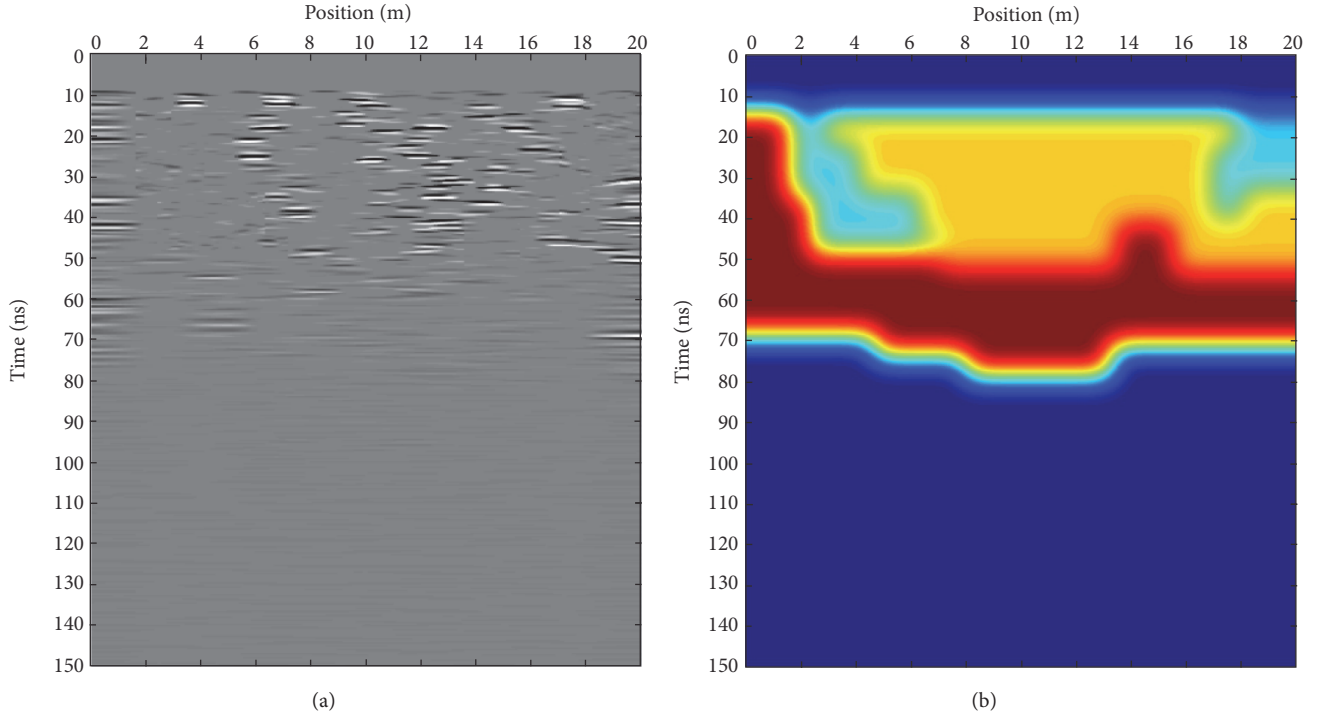


FIGURE 7: (a) Adaptive f - x EMD result of the integrated model, (b) the map of corresponding removed IMFs number.

TABLE 2: Simulation Parameters.

<i>Antennas</i>	Dominant frequency	500 MHz
	Source type	Point source
	Waveform	Ricker wavelet
<i>Absorbing boundary</i>	Type	C-PML
	Thickness	0.11 m
<i>Discretization grid</i>		0.005 m * 0.005 m
<i>Time step</i>		0.040434 ns
<i>Time window</i>		150ns
<i>CPU</i>	Intel(R) Core(TM) i5-4590 CPU @3.30GHz	
<i>RAM</i>	8.00 GB	
<i>Time</i>	20.4824 hours	

Figure 9 shows the interpretation of the integrated model result. According to the adaptive f - x EMD result of the integrated model, we locate the position of each rock block (Figure 9(a)); except for several redundant rocks (shown by red dots) and missing rocks (shown by the green dot), the position of the rock block is matched with the original model (Figure 6(a)). The IMFs map on the one hand helps to divide the area according to the number of rock blocks. On the other hand, it also helped us to get the interface of regolith and bedrock, which is not clear in the radar image. The Chang'E-5 mission will drill and collect the regolith from the moon [29], which requires that there are no rocks below the drilling point; otherwise the drilling machine will be damaged. The adaptive f - x EMD method and its IMFs map can help us select the drilling point, as shown in Figure 8(b) (2m and 18m), which will greatly reduce the probability of machine damage.

5. Results and Discussion

It is proven that the adaptive f - x EMD is suitable for LPR data processing. The processing results are shown in Figure 10. And the corresponding f - k spectrums (Figure 11) also show the effectiveness of high-wavenumber components suppression. We can observe that there are some artefacts in the deep section of the preprocessed data (Figure 2). These artefacts have certain continuity and gentle dip angle, which will affect the recognition of the rock, so we mute the section of deep artefacts. The processing result shows the location of the rock (left) and the degree of the rock enrichment (right).

In order to further explain the processing results, we extract the rocks (Figure 12) based on the feature of the processed LPR data. After the extraction of each rock, the extracted rocks are superimposed with Figure 12(b). The red area has the largest number of rock blocks, the yellow

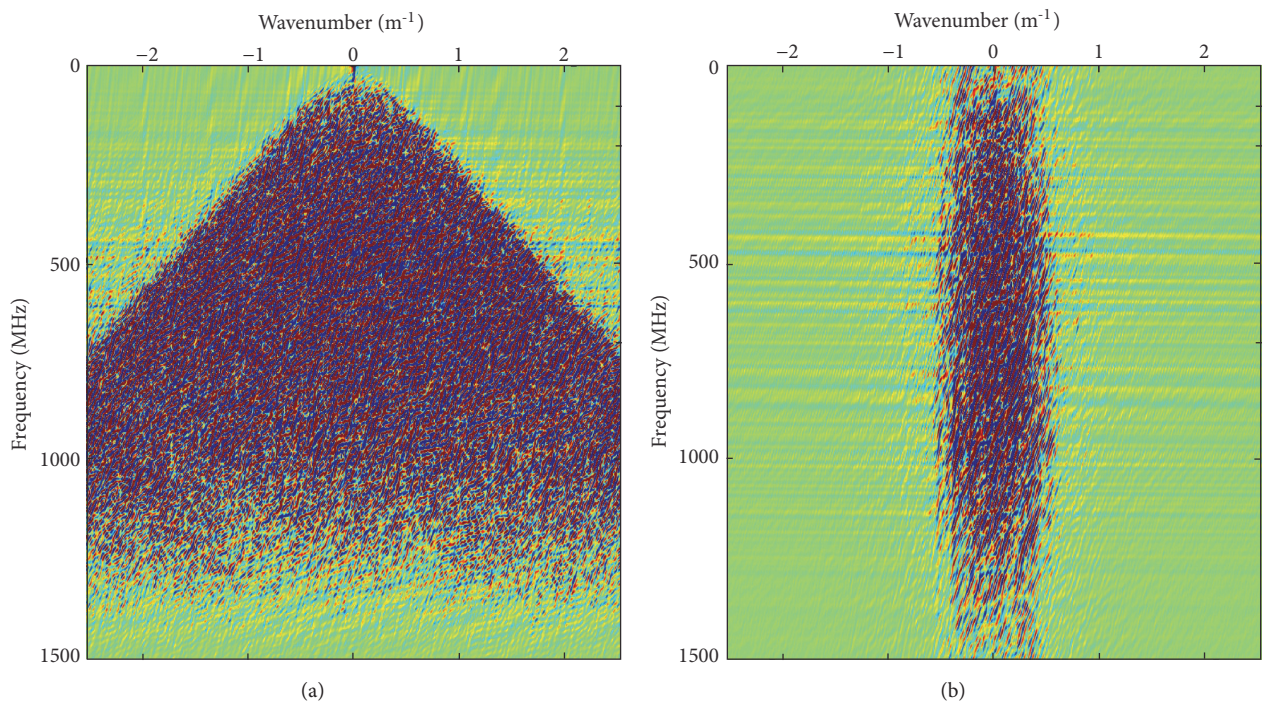


FIGURE 8: The comparison of f-k spectrum. (a) Forward simulation result; (b) adaptive f-x EMD result.

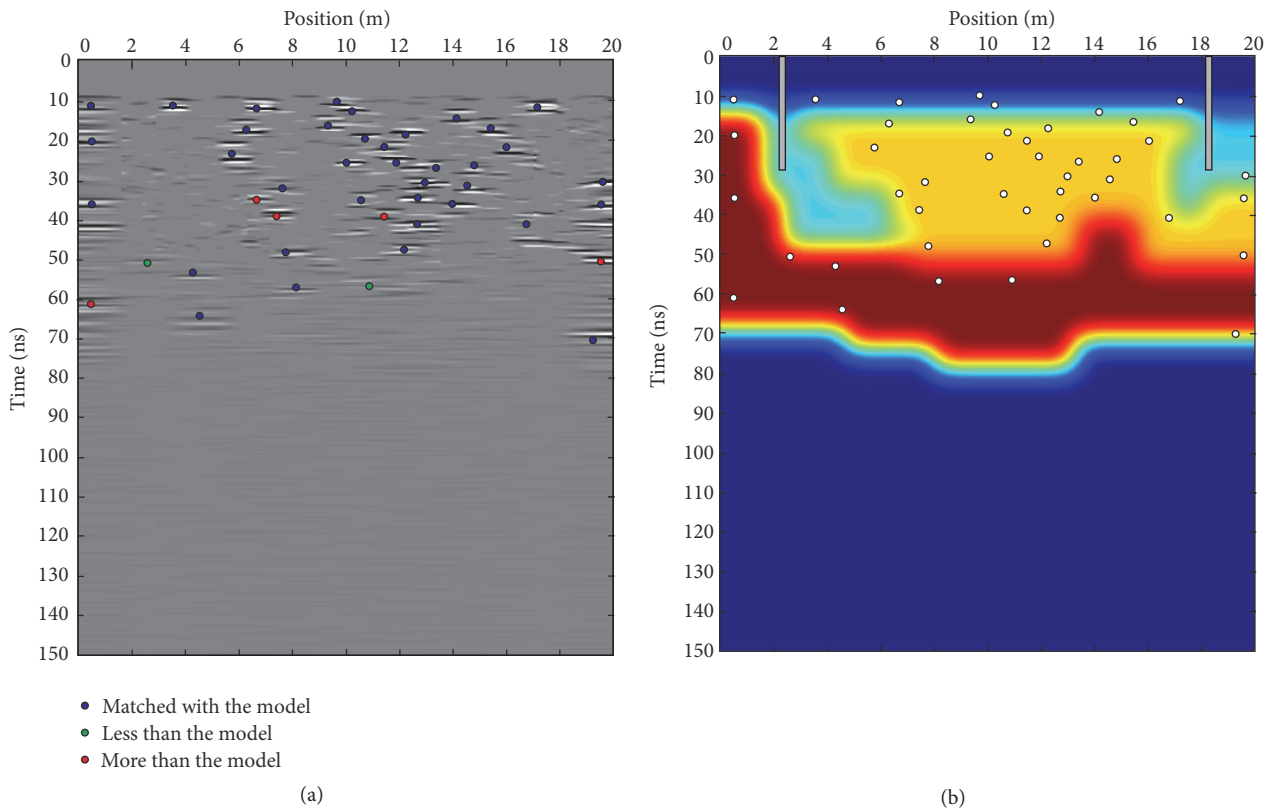


FIGURE 9: Interpretation of the integrated model result.

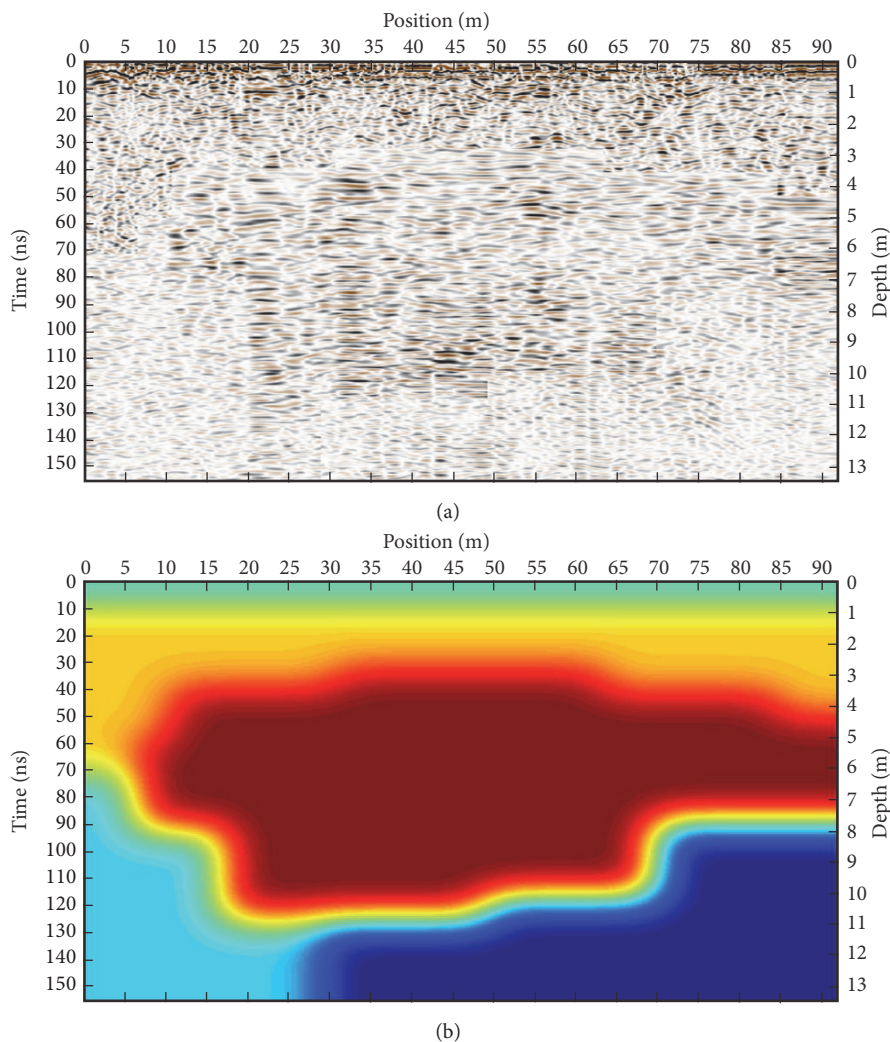


FIGURE 10: (a) Adaptive f-x EMD result of LPR CH-2 data. (b) The IMFs map of LPR CH-2 data.

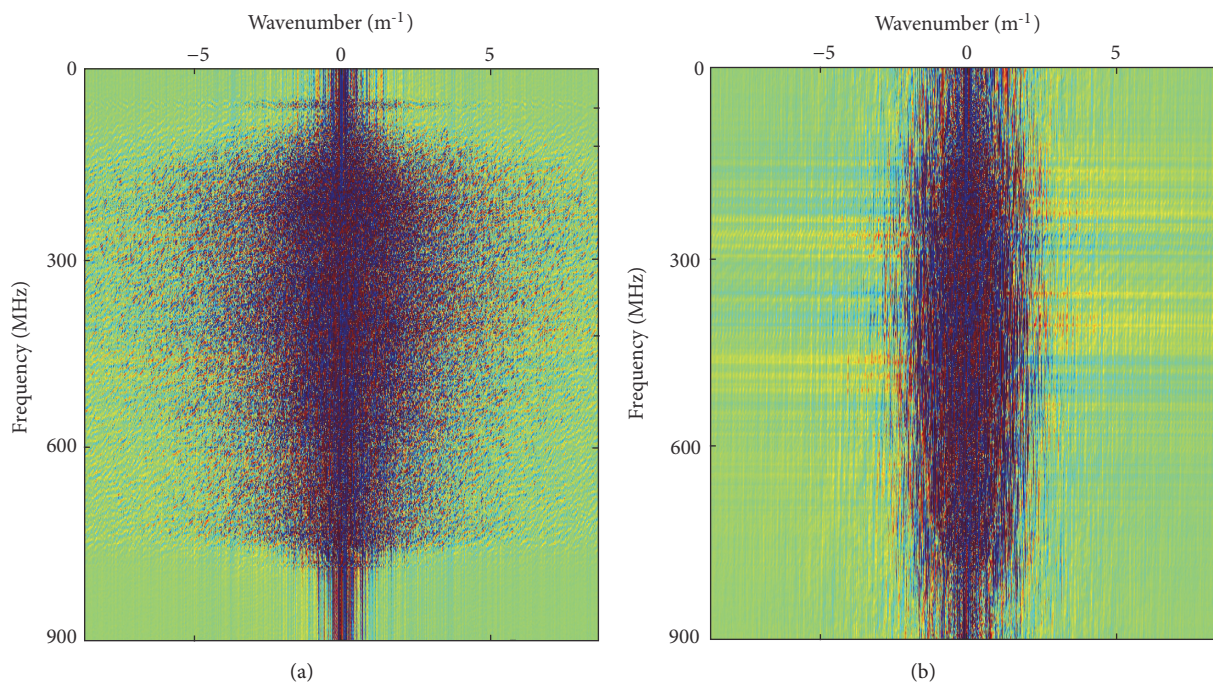


FIGURE 11: The comparison of f - k spectrum. (a) LPR CH-2 data. (b) Adaptive f-x EMD result.

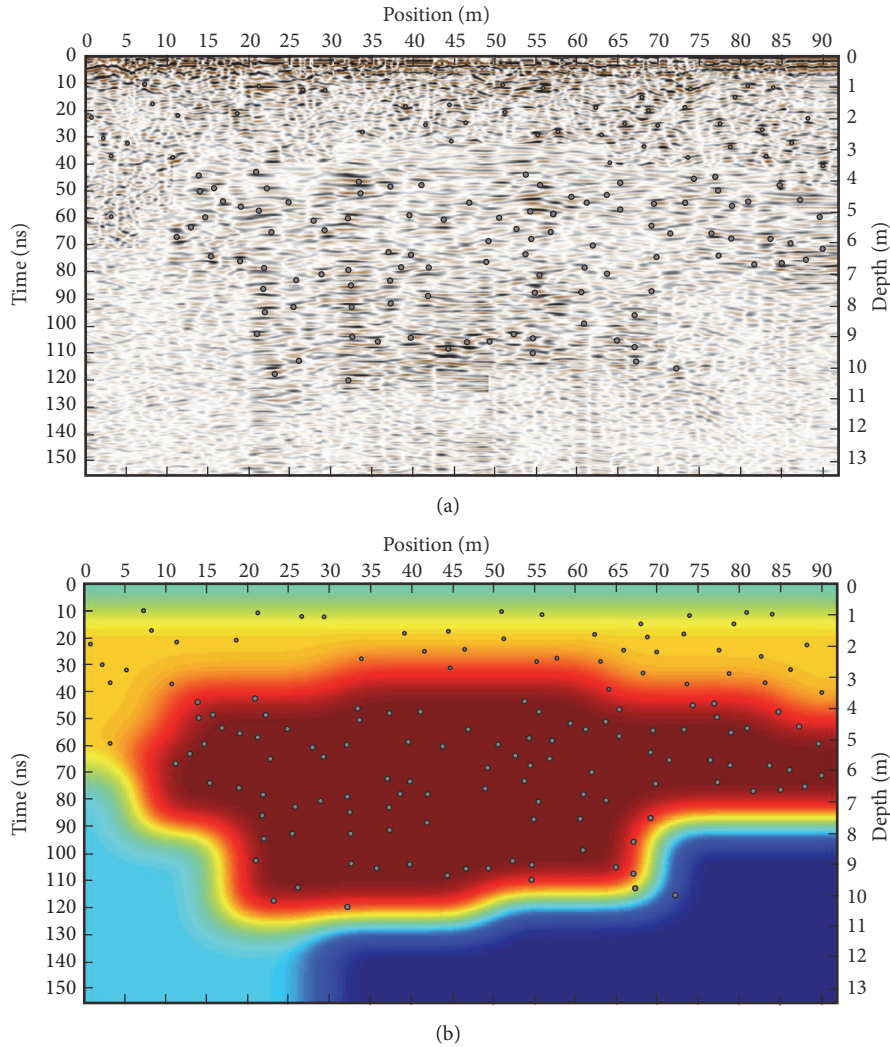


FIGURE 12: (a) The position of each rock and (b) the interface of LPR CH-2 data.

area is the second, and the blue area is the least, which is consistent with the above simulation results. The dividing lines in Figure 12(b) also help us to stratify the regolith layer and divide the LPR data into three layers.

After the above processing, we give an interpretation according to the formation of the lunar regolith and the former results. The LPR data are divided into three layers (Figure 13).

(1) Bedrock (below ~ 9 m). This layer is basalt, which is the product of the last basalt covering.

(2) Deep regolith (between ~ 3 m and ~ 9 m). This regolith layer contains a lot of rock fragments, because, after the formation of paleo-regolith, the small meteorite can not penetrate the upper regolith layer, leading to a lower degree of weathering, a larger grain size, and more rock masses.

(3) Shallow regolith (up ~ 3 m). This regolith layer has a higher degree of weathering, regardless of the impact of the meteorites or other weathering factors, such as the effect of space particles and electromagnetic radiation, etc., which can all affect the shallow regolith layer, thus decreasing the number and size of the rock blocks.

6. Conclusions

The LPR equipped on Yutu Rover detected the lunar geological structure in the Northern Imbrium. A data preprocessing workflow is designed to solve some types of issues, such as repeated and waste traces and noise. The position of each rock and the contact interface of regolith is still difficult to recognize. On the basis of good preprocessing, we propose an adaptive f-x EMD to locate the rocks in the regolith. The corresponding removed IMF map can reveal the degree of rock enrichment to a certain extent and the contact interface of regolith and the basement rock, which can provide a preference in data interpretation.

Based on the processed LPR CH-2 data, we locate the position of each rock and highlight the contact interface of regolith and the basement rock. The LPR data are divided into three layers: bedrock (below ~ 9 m), deep regolith (between ~ 3 m and ~ 9 m), and shallow regolith (up ~ 3 m). The bedrock is basalt, which is the product of the last basalt covering. The deep regolith contains a lot of rock fragments with a lower degree of weathering. The shallow regolith layer has

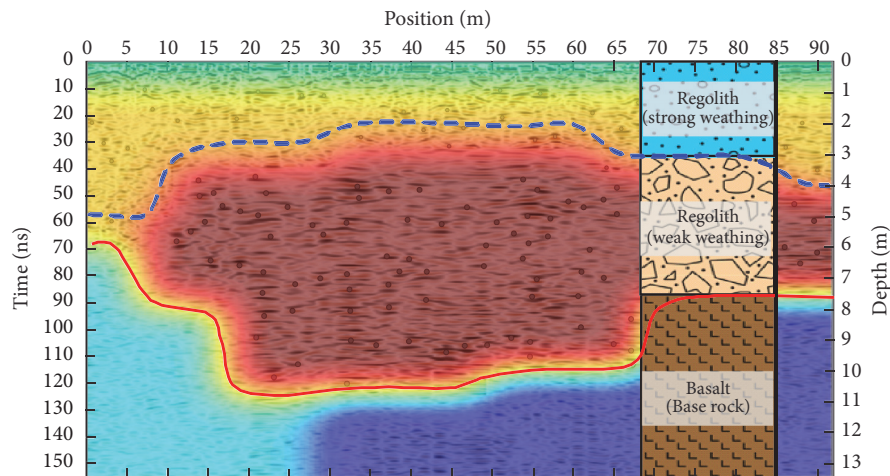


FIGURE 13: Interpretation of CH-2 data.

a higher degree of weathering with a few number of the rocks.

These results provide valuable information regarding our understanding of the modification of the lunar surface and the evolution of the regolith, and the results are also important as a reference for future lunar sample return missions.

Data Availability

Data are hosted by National Astronomical Observatories, Chinese Academy of Sciences. Please visit: <http://moon.bao.ac.cn>.

Conflicts of Interest

The authors declare that they have no conflicts of interest.

Acknowledgments

The authors acknowledge Madagascar software for the open-source code and the open-source data in <http://moon.bao.ac.cn>. This work was supported by the Major Projects of the National Science and Technology of China (Grant No. 2016ZX05026-002-003), the National Natural Science Foundation of China (41374108, 41574097, and 41504083), the National Key Research Development Program (2016YFC06001104), and the Graduate Innovation Fund of Jilin University (2018090).

References

- [1] L. Xiao, P. Zhu, G. Fang et al., "A young multilayered terrane of the northern Mare Imbrium revealed by Chang'E-3 mission," *Science*, vol. 347, no. 6227, pp. 1226–1229, 2015.
- [2] G.-Y. Fang, B. Zhou, Y.-C. Ji et al., "Lunar penetrating radar onboard the Chang'e-3 mission," *Research in Astronomy and Astrophysics*, vol. 14, no. 12, pp. 1607–1622, 2014.
- [3] Y. Su, G.-Y. Fang, J.-Q. Feng et al., "Data processing and initial results of Chang'e-3 lunar penetrating radar," *Research in Astronomy and Astrophysics*, vol. 14, no. 12, pp. 1623–1632, 2014.
- [4] J. Zhang, W. Yang, S. Hu et al., "Volcanic history of the Imbrium basin: a close-up view from the lunar rover Yutu," *Proceedings of the National Academy of Sciences of the United States of America*, vol. 112, no. 17, pp. 5342–5348, 2015.
- [5] W. Fa, M. Zhu, T. Liu, and J. B. Plescia, "Regolith stratigraphy at the Chang'E-3 landing site as seen by lunar penetrating radar," *Geophysical Research Letters*, vol. 42, no. 23, pp. 179–187, 2016.
- [6] J. Lai, Y. Xu, X. Zhang, and Z. Tang, "Structural analysis of lunar subsurface with Chang'E-3 lunar penetrating radar," *Planetary and Space Science*, vol. 120, pp. 96–102, 2016.
- [7] L. Zhang, Z. Zeng, J. Li et al., "A story of regolith told by lunar penetrating radar," *Icarus*, vol. 321, pp. 148–160, 2019.
- [8] Z. Dong, G. Fang, Y. Ji, Y. Gao, C. Wu, and X. Zhang, "Parameters and structure of lunar regolith in Chang'E-3 landing area from lunar penetrating radar (LPR) data," *Icarus*, vol. 282, pp. 40–46, 2016.
- [9] L. Zhang, Z. Zeng, J. Li et al., "Parameter estimation of lunar regolith from lunar penetrating radar data," *Sensors*, vol. 18, no. 9, 2018.
- [10] A. W. Trorey, "A simple theory for seismic diffractions," *Geophysics*, vol. 35, no. 5, pp. 1961–1983, 1970.
- [11] E. De Bazelaire, "Normal moveout revisited: inhomogeneous media and curved interfaces," *Geophysics*, vol. 53, no. 2, pp. 143–157, 1988.
- [12] N. E. Huang, Z. Shen, S. R. Long et al., "The empirical mode decomposition and the Hilbert spectrum for nonlinear and non-stationary time series analysis," *Proceedings A*, vol. 454, pp. 903–995, 1998.
- [13] M. Bekara and M. van der Baan, "Random and coherent noise attenuation by empirical mode decomposition," *Geophysics*, vol. 74, no. 5, pp. V89–V98, 2009.
- [14] H.-P. Cai, Z.-H. He, and D.-J. Huang, "Seismic data denoising based on mixed time-frequency methods," *Applied Geophysics*, vol. 8, no. 4, pp. 319–327, 2011.
- [15] Y. Chen and J. Ma, "Random noise attenuation by f - x empirical-mode decomposition predictive filtering," *Geophysics*, vol. 79, no. 3, pp. V81–V91, 2014.

- [16] W. Chen, J. Xie, S. Zu, S. Gan, and Y. Chen, "Multiple-reflection noise attenuation using adaptive randomized-order empirical mode decomposition," *IEEE Geoscience and Remote Sensing Letters*, vol. 14, no. 1, pp. 18–22, 2016.
- [17] Y. Chen, "Dip-separated structural filtering using seislet transform and adaptive empirical mode decomposition based dip filter," *Geophysical Journal International*, vol. 206, no. 1, pp. 457–469, 2016.
- [18] Y. Chen and S. Fomel, "EMD-seislet transform," *Geophysics*, vol. 83, no. 1, pp. A27–A32, 2018.
- [19] Y. Chen, Y. Zhou, W. Chen, S. Zu, W. Huang, and D. Zhang, "Empirical low-rank approximation for seismic noise attenuation," *IEEE Transactions on Geoscience and Remote Sensing*, vol. 55, no. 8, pp. 4696–4711, 2017.
- [20] B. Hu, D. Wang, L. Zhang, and Z. Zeng, "Rock location and quantitative analysis of regolith at the change 3 landing site based on local similarity constraint," *Remote Sensing*, vol. 11, no. 5, pp. 530–548, 2019.
- [21] S. David, G. Taylor, P. Warren, and G. Ryder, *The Lunar Regolith, in Lunar Source-Book: A User's Guide to the Moon*, G. Heiken, D. Vaniman, and B. French, Eds., Cambridge University Press, New York, NY, USA, 1991.
- [22] Y. Mao and P. Que, "Noise suppression and flaw detection of ultrasonic signals via empirical mode decomposition," *Russian Journal of Nondestructive Testing*, vol. 43, no. 3, pp. 196–203, 2007.
- [23] Y. Kopsinis and S. McLaughlin, "Development of EMD-based denoising methods inspired by wavelet thresholding," *IEEE Transactions on Signal Processing*, vol. 57, no. 4, pp. 1351–1362, 2009.
- [24] M. Bekara and M. Van der Baan, "Local singular value decomposition for signal enhancement of seismic data," *Geophysics*, vol. 72, no. 2, pp. V59–V65, 2007.
- [25] L. Zhang, Z. Zeng, J. Li et al., "Simulation of the lunar regolith and lunar-penetrating radar data processing," *IEEE Journal of Selected Topics in Applied Earth Observations and Remote Sensing*, vol. 11, no. 2, pp. 655–663, 2018.
- [26] L. Zhang, Z. F. Zeng, J. Li, and J. Y. Lin, "Study on regolith modeling and lunar penetrating radar simulation," in *Proceedings of the 16th International Conference of Ground Penetrating Radar, GPR 2016*, pp. 1–5, IEEE, Hong Kong, June 2016.
- [27] J. Li, Z. Zeng, C. Liu, N. Huai, and K. Wang, "A Study on lunar regolith quantitative random model and lunar penetrating radar parameter inversion," *IEEE Geoscience and Remote Sensing Letters*, vol. 14, no. 11, pp. 99–103, 2017.
- [28] J. Irving and R. Knight, "Numerical modeling of ground-penetrating radar in 2-D using MATLAB," *Computers & Geosciences*, vol. 32, no. 9, pp. 1247–1258, 2006.
- [29] Y. Li, W. Lu, G. Fang, and S. Shen, "The imaging method and verification experiment of change-5 lunar regolith penetrating array radar," *IEEE Geoscience and Remote Sensing Letters*, vol. 15, no. 7, pp. 1006–1010, 2018.

Research Article

Several Geological Issues of Schrödinger Basin Exposed by CE-2 CELMS Data

Z. G. Meng ^{1,2,3}, H. H. Wang,¹ Y. C. Zheng ³, Y. Z. Wang ¹, H. Miyamoto,⁴
Z. C. Cai,² J. S. Ping,³ and Y. Z. Zhu¹

¹College of Ge exploration Science and Technology, Jilin University, Changchun 130026, China

²State Key Laboratory of Lunar and Planetary Sciences, Macau University of Science and Technology, Macau

³Key Laboratory of Lunar and Deep Space Exploration, National Astronomical Observatories, Chinese Academy of Sciences, Beijing 100101, China

⁴The University Museum, University of Tokyo, Bunkyo-ku, Tokyo 113-0033, Japan

Correspondence should be addressed to Y. C. Zheng; zyc@bao.ac.cn and Y. Z. Wang; iamwangyongzhi@126.com

Received 2 February 2019; Revised 5 May 2019; Accepted 26 May 2019; Published 1 July 2019

Academic Editor: Josep M. Trigo-Rodríguez

Copyright © 2019 Z. G. Meng et al. This is an open access article distributed under the Creative Commons Attribution License, which permits unrestricted use, distribution, and reproduction in any medium, provided the original work is properly cited.

The study on the Schrödinger basin may provide important clues about the formation of South Pole-Aitken (SPA) basin. In this paper, the thermophysical features of Schrödinger basin were evaluated using the Chang'E-2 microwave sounder (CELMS) data. The results are as follows. (1) The geological units are reevaluated with the CELMS data and a new geological view was provided according to the brightness temperature and emissivity maps. (2) The surface topography plays an important role in the observed CELMS data. (3) The hot anomaly in the basin floor indicates a warm substrate. (4) The pyroxene-bearing anorthosite is probably an important cause for the cold anomaly over the lunar surface. Also, the study proves the applicability of the CELMS data applying in high latitude regions to a certain extent.

1. Introduction

Schrödinger basin is the best preserved basin of its size and laid in the southwest corner of the South Pole-Aitken (SPA) basin (Figure 1(a)), the largest and oldest impact crater on the Moon [1, 2]. The basin is superposed on the floor of SPA basin and it may likely excavate the materials from the lower crust or upper mantle [2–4]. Thus, the diversity of the materials and the special mare volcanism in the basin could provide some important information about the formation of Schrödinger basin and even SPA basin.

Schrödinger basin, centered at (76°S, 134°E), is about 334 km in diameter. It also has an inner peak ring of 168 km in diameter represented by a discontinuous ring of mountains [5]. Wilhelms et al. [6] firstly provided the geological mapping effort of this basin at 1:5M scale based on Lunar Orbiter data. Thereafter, Shoemaker et al. [7] improved the geological interpretation with the Clementine UV-VIS data. Using the data from the Lunar Reconnaissance Orbiter, Clementine, Lunar Prospector, and Lunar

Orbiter, Mest [2] evaluated the contacts and structures of geological units and at last identified three groups including nine distinct units (Figure 1(b)), indicating that Schrödinger basin comprises the pre-Schrödinger crustal materials, the mafic and anorthositic materials, and the volcanic materials. Additionally, abundant fractures occur in the basin floor, some of which extend to a few hundred kilometers long. Shankar et al. [8] verified a heterogeneous distribution of both anorthositic and basaltic materials in the basin floor. Using remote sensing data and impact crater modeling, Kramer et al. [9] reevaluated the composition of materials that make up the basin wall, impact melt, and peak ring, providing a new understanding of basin-forming processes. Through analyzing the LRO LOLA data and the Chandrayaan data, Kumar et al. [10] concluded the boulder falls in the basin floor triggered by the recent shallow moonquakes and impact events, indicating that this is geologically active zone until now. Therefore, Schrödinger basin presents an appropriate place to evaluate the thermophysical features of the diverse materials forming the SPA and Schrödinger basins and the

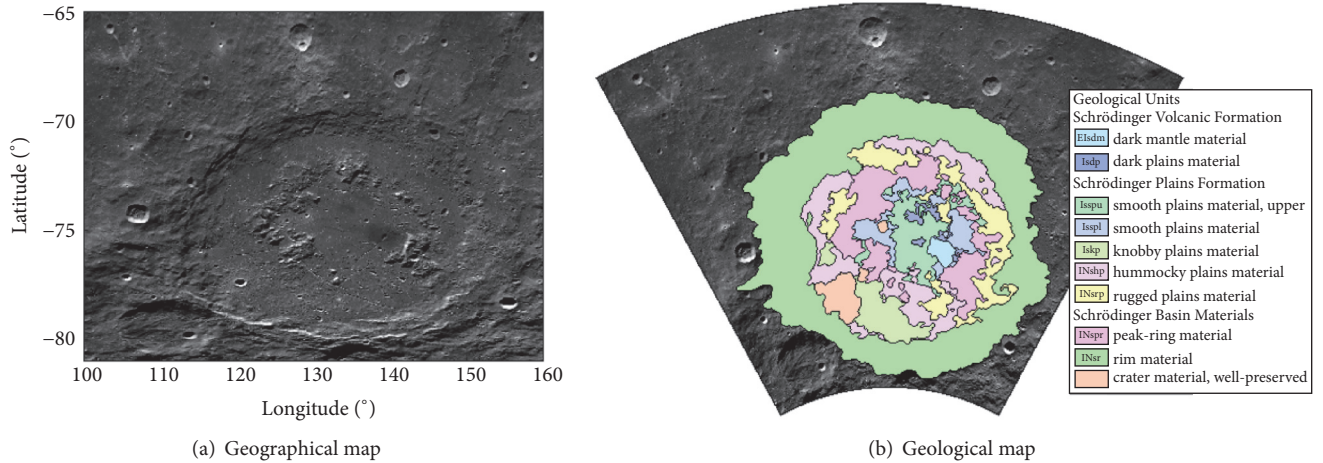


FIGURE 1: WAC image (a) and geological map (b) of Schrödinger basin. Note: Figure 1(a) was downloaded from <http://wms.lroc.asu.edu/lroc/search>. Figure 1(b) geological map is interpreted by Mest [2].

substrate thermal features related to the tectonic activities. This is also the motivation for us to study the basin with the microwave sounder (CELMS) data.

The CELMS instrument was onboard Chinese Chang'E-2 (CE-2) satellite, which is designed to measure the thermal emission of the shallow lunar surface in microwave domain. The CELMS data are of special significance in the current lunar geological study, which has been proved by Meng et al. [11] and Hu et al. [12] through evaluating the mare volcanism in Mare Imbrium. Meng et al. [13] also gave a distinctly different view about Mare Crisium using the CE-2 CELMS data compared to the optical data and indicated a new understanding about the mare volcanism there. This hints to the potential applications of the CELMS data to better understand the thermal evolution of the Moon.

However, Schrödinger basin is located in high latitude regions, which has harsh topographic and illuminating conditions. To testify the applicability of the CELMS data in such conditions is also our motivation. In this paper, Section 2 thoroughly describes the processing of the CELMS data. Section 3 analyses the MTE features of the geological units in the basin. The geological applications are discussed in Section 4. Section 5 presents the conclusions.

2. Data Processing

Schrödinger basin is totally located in the high latitude region with fairly complex topographic and illuminating conditions, which makes it difficult to select and process the CELMS data [14–16].

2.1. CELMS Data Processing. The CELMS data used in the study were collected from the CE-2 satellite, which operated at 3.0, 7.8, 19.35, and 37 GHz channels. The observation time was from October 2010 to May 2011. The incident angle is 0° , and the temperature sensitivity is better than 0.5 K. A detailed description of the CELMS data was given by Cai and Lan [17] and Meng et al. [18].

According to the range of Schrödinger basin, more than 600 tracks of swath CELMS data were acquired. For the brightness temperature (T_B) is heavily influenced by the surface temperature, or surface illumination [12, 16], the hour angle is introduced to describe the measured T_B in different time spans [11, 13, 15, 19, 20]. Additionally, the quantity of the selected CELMS data is more than five times as that with a similar area in low latitude regions [18]. However, after overlying the obtained CELMS data on Schrödinger basin (Figure 2), 1° spatial resolution along the latitude and very high spatial resolution along the longitude are clearly presented.

The soundly large quantity of the CELMS data means that the T_B maps at multiple time periods can be generated (Figure 3). But just as in Figure 3, we may obtain the CELMS data at 8 and 14 o'clock. Unfortunately, there occurs an apparent position problem in Figure 3, which is indicated by the red line. The position of the T_B in the left side of the red line apparently does not match that of the T_B in the right side, hinting that the CELMS data at this time are not proper. After carefully checking the original CELMS data, the CELMS data at 0 and 10 o'clock are proper to generate the T_B maps of Schrödinger basin, which can represent the T_B at nighttime and daytime.

Thereafter, the CELMS data processing procedure is similar to that suggested by Meng et al. [11]. For the linear interpolation method can slightly alter the original data, it is employed to generate the T_B maps with a spatial resolution of $0.25^\circ \times 0.25^\circ$ (Figure 4).

Figure 4 presents that the T_B distribution is strongly latitude-dependent. E.g., the T_B variation at 37 GHz with latitude from the north to the south is more than 100 K at daytime and about 90 K at midnight. But the T_B in the central basin floor is only about 10 K higher than its vicinity. That is, the T_B variation with the latitude is much larger than that resulted from the thermophysical parameters of the lunar regolith [13]. Therefore, this latitude-dependent impact must be eliminated before using the generated T_B maps.

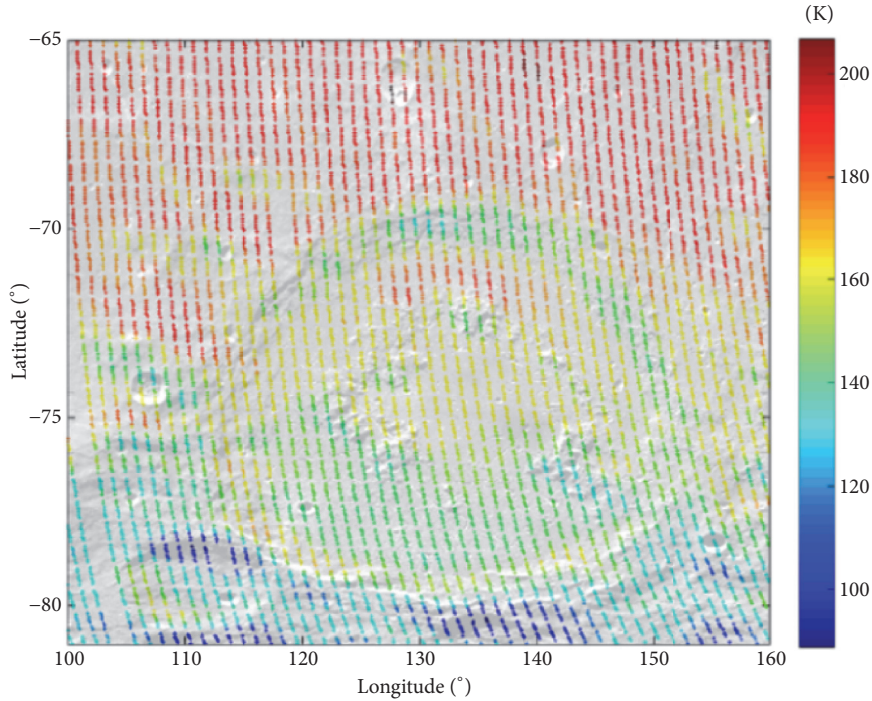


FIGURE 2: Scatter map of the 37-GHz CELMS data at noon overlaid on WAC image.

Thus, the standard T_B of every latitude is proposed. Firstly, one T_B is selected for every latitude on the condition that the $(\text{FeO}+\text{TiO}_2)$ abundance, surface slope, and rock abundance are similar in all selected positions. Here, the selection criteria are same as Meng et al. [13]. The composition, surface slope, and rock abundance data are referred through JMARS software. The selected T_B for every channel is presented as a dash line in Figure 5. Thereafter, a fitting curve is made according to the selected T_B , which is defined as the standard TB for every latitude (Figure 5).

Finally, the normalized T_B (nT_B) can be calculated using the T_B divided by the standard T_B along the corresponding latitude. Figure 6 is the 37-GHz nT_B maps at 10 and 0 o'clock, which shows that the latitude-dependent effect of the T_B maps is well eliminated.

2.2. Image Cut and Overlaying. Figure 6 indicates a new different view about Schrödinger basin compared to the optical data, hinting at the potential geological applications of the CELMS data in high latitude regions. Largely, the nT_B behaviors show a good correlation with the topography, e.g., the northern interior wall with reduced solar illumination, and the composition, e.g., in the peak ring with relatively higher nT_B . However, the nT_B difference among the geological units is still not distinct. This mainly resulted from the nT_B values in Granswindt crater (111.2°E , 79.4°S) in the southwest and Nefed'ev crater (135.8°E , 81.1°S) in the south, whose nT_B is lowest in the selected regions, and from the southern interior wall of Grotrian crater (128.3°E , 66.2°S), whose nT_B is almost highest at daytime. Fortunately, the three mentioned regions are all situated beyond Schrödinger basin. Thus, to better understand the thermophysical features of the

geological units, only the nT_B within Schrödinger basin is kept, which is cut according to the boundary given by Mest [2] (Figures 7 and 8). Figures 7 and 8 show that the difference among the geological units is well strengthened compared to that in Figure 6.

What is more, the geological units have been fully studied by Mest [2] and Kramer et al. [9]. To improve the understanding of the geological meanings of the nT_B maps, the interpretation result by Mest [2] is vectorized and overlaid on the nT_B maps in black line. Also, the WAC image is overlaid by the 37-GHz-channel nT_B at daytime and midnight to postulate the detailed distribution of the nT_B values (Figure 9). The coincidence between the nT_B performances and the geological units as well as the topographic terrains is largely good, indicating the rationality of the generated nT_B maps.

2.3. Emissivity Maps Generation. In high latitude regions, the CELMS data will experience harsher solar illumination conditions compared to the low latitude regions [14, 15, 19]. This phenomenon is obviously indicated by the lowest values in the northern wall and by the highest values in the southern wall. Thus, how to eliminate the topographic impact is a crucial issue for the applications of the CELMS data.

Up to now, the surface temperature has been fully studied by means of the numerical simulation by Meng et al. [16], He et al. [21], and Hu et al. [22]. Therefore, the surface temperature was simulated with improved Racca model [16] using the CE-1 LAM data, which was recommended by Hu et al. [23] for its coincidence with the footprint of the CELMS data. For the parameters used, the reader can be referred to [16]. The original solar irradiance is the average

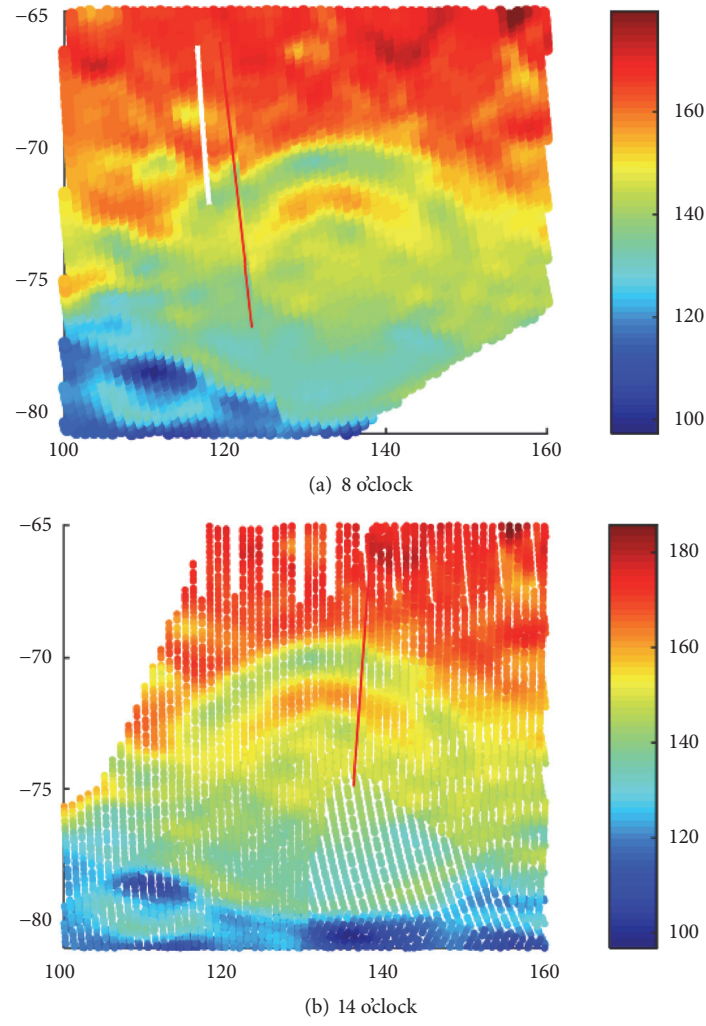


FIGURE 3: CELMS data at 8 (a) and 14 (b) o'clock (unit: K).

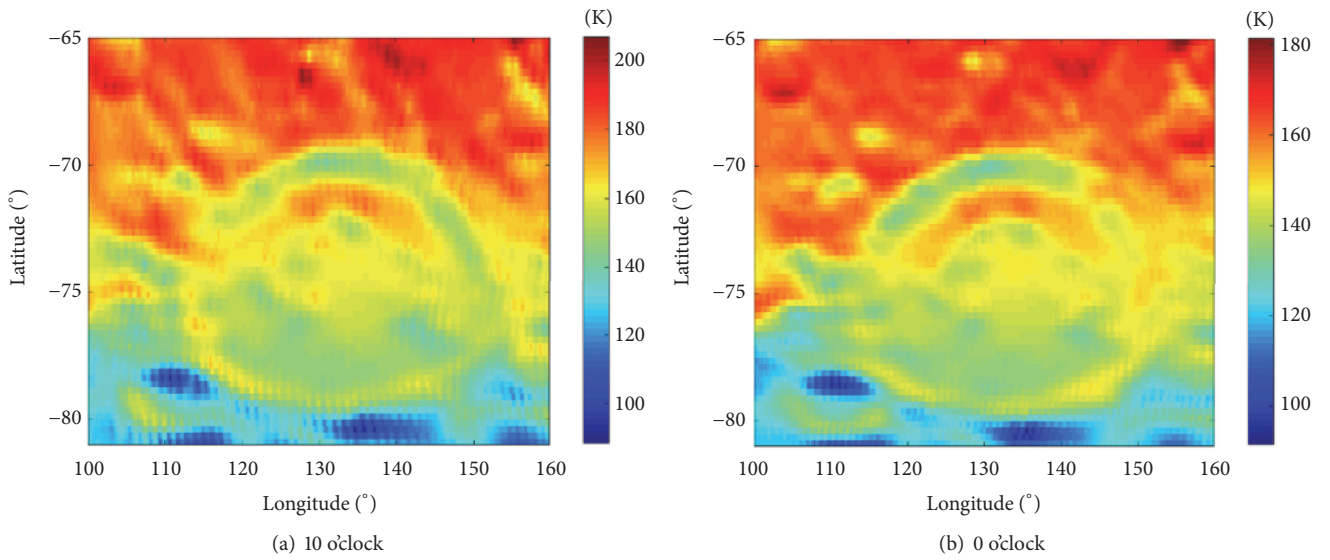


FIGURE 4: T_B distribution map of Schrödinger basin at 37 GHz.

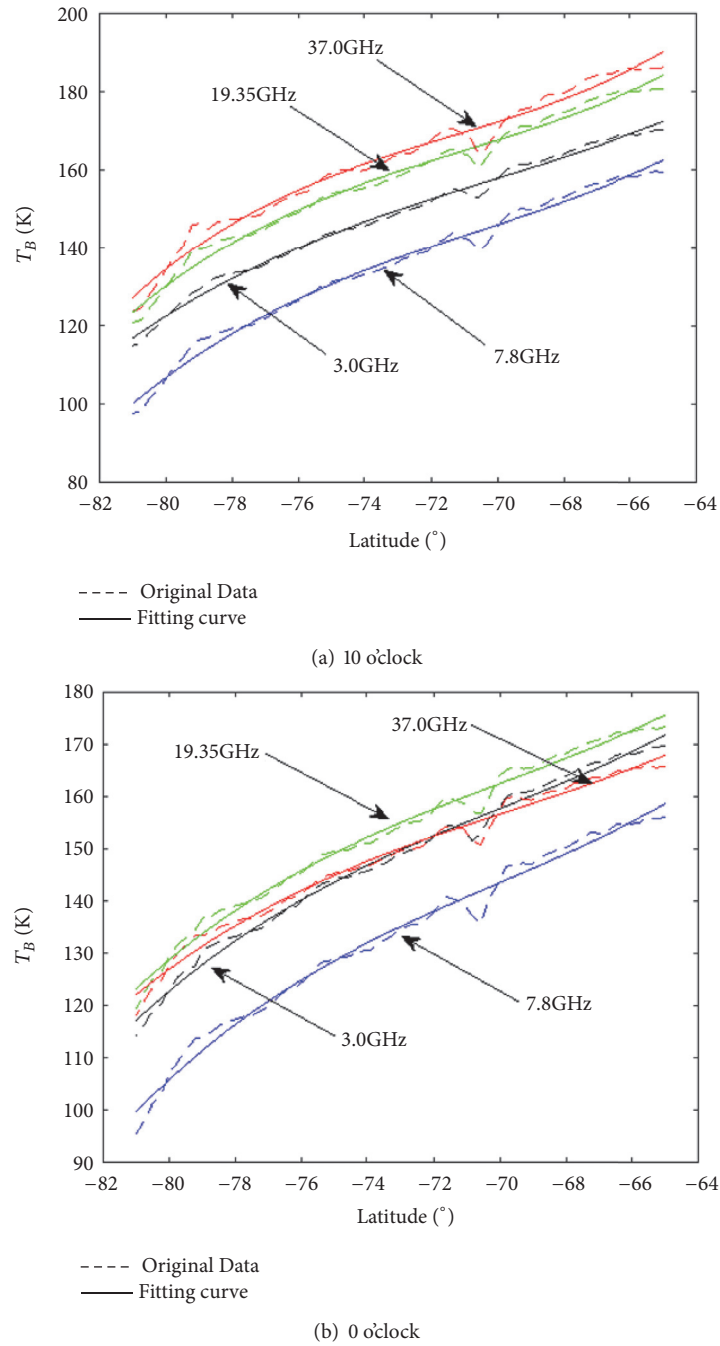


FIGURE 5: Generation of the standard T_B .

value. Moreover, the time used is at 10 o'clock, which is corresponding to the daytime CELMS data used in this study. Then, the ratio between the generated T_B and the surface temperature is the emissivity of the lunar regolith at the corresponding channel (Figure 10).

Compared to Figure 7, Figure 10 indicates that the influence from the surface topography is weakened to some extent, which can be expressed by the emissivity in the northern and southern interior walls. Thus, the emissivity map is also employed to provide supplements to improve understanding of the MTE features of the regolith units.

However, the simulated surface temperature is in ideal conditions, which is not suitable for the real environment during the CELMS observation. Thus, the introduction of the surface temperature and the estimated emissivity are employed only for referring.

3. MTE Features of Schrödinger Basin

Mest [2] identified three groups in Schrödinger basin, including Schrödinger basin materials, Schrödinger plains

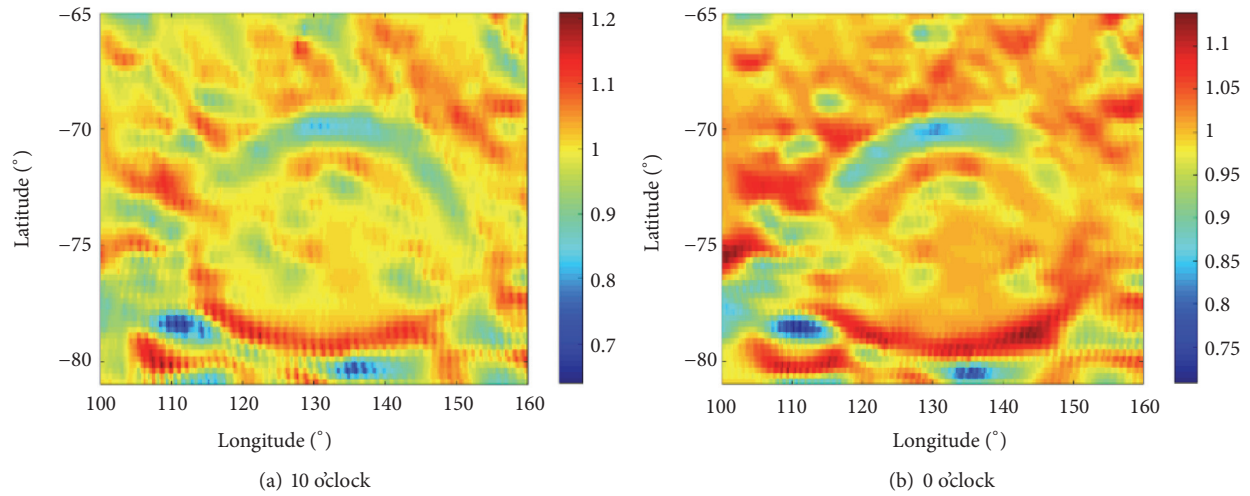


FIGURE 6: nT_B map of Schrödinger basin at 37 GHz.

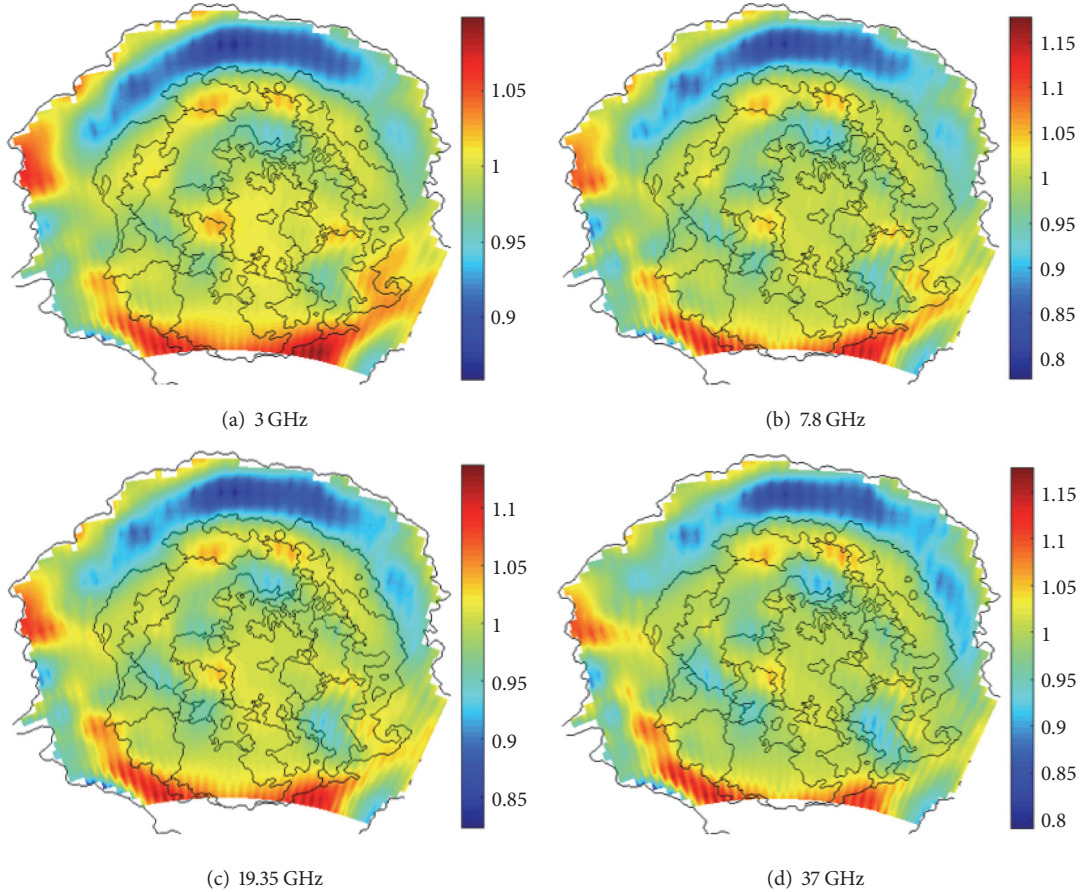


FIGURE 7: nT_B maps of the Schrödinger basin at 10 o'clock.

formation, and Schrödinger volcanic formation. Figures 7 and 8 indicate similar nT_B behaviors about Schrödinger basin. That is, though the T_B at daytime is higher than that at nighttime, the region with relatively higher nT_B at daytime also shows relatively higher values at nighttime and vice versa.

This presents special microwave thermal emission (MTE) features about the materials in the basin.

3.1. Schrödinger Basin Materials Group. Schrödinger basin materials comprise the peak-ring unit (INspr) and basin rim

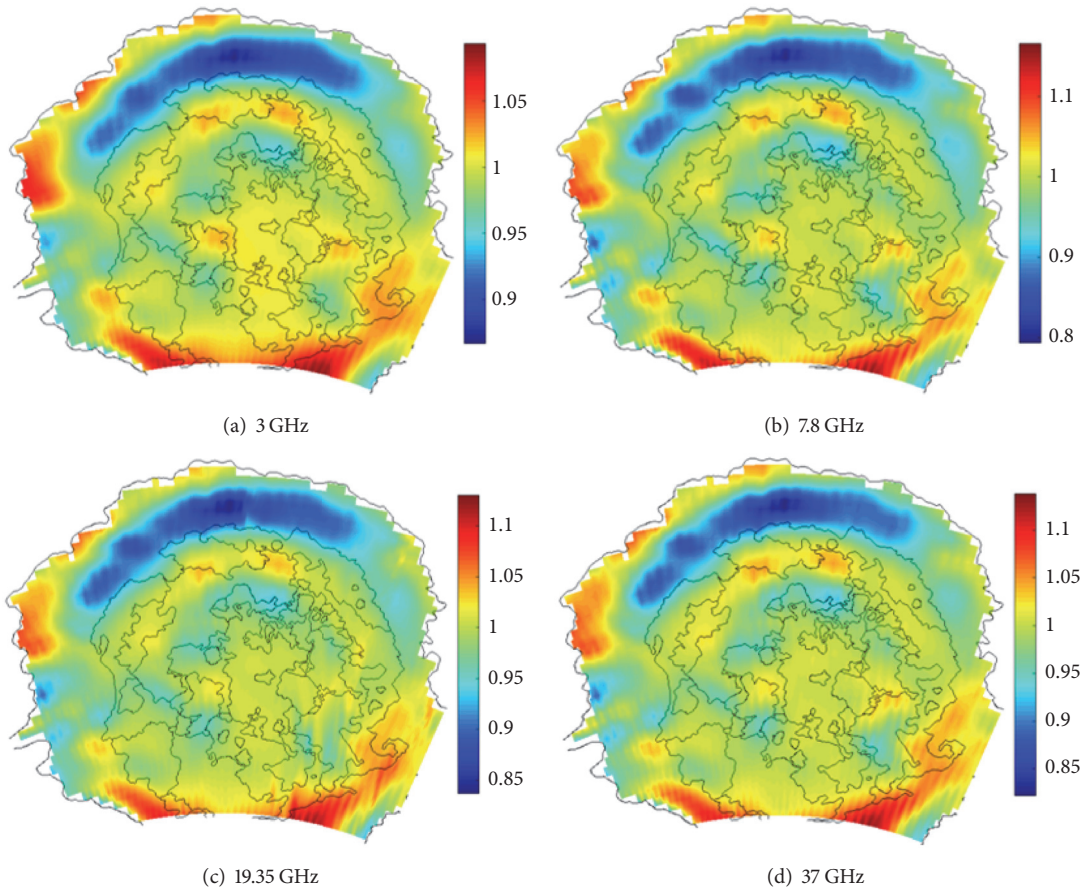


FIGURE 8: nT_B maps of the Schrödinger basin at 0 o'clock.

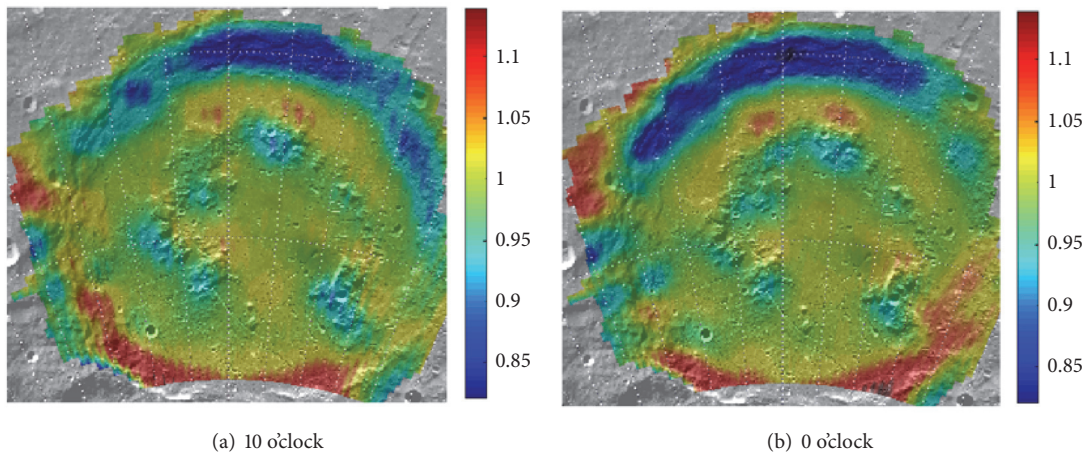


FIGURE 9: 37-GHz nT_B map overlays on WAC image with 60% transparency.

unit (INsr) (Figure 1(b)), which is interpreted to consist of pre-Schrödinger crustal materials [2].

Unit INspr is the incomplete peak ring of mountainous terrain, which displays moderate albedo in Clementine images but is mottled in high-resolution LROC images [2]. Figures 7 and 8 indicate that the unit has rather low nT_B values at daytime and midnight, especially at 3.0 GHz maps.

The regions with low nT_B apparently form an incomplete ring, coinciding well with its terrain. But, several regions around (127.3°E, 72.3°S), (129.0°E, 75.3°S), (134.4°E, 71.6°S), and (143.0°E, 75.2°S) present the relatively higher nT_B than their vicinities. Combined with the topography map, such regions are slopes originating to the solar illumination, indicating the strong influence of the topography on the

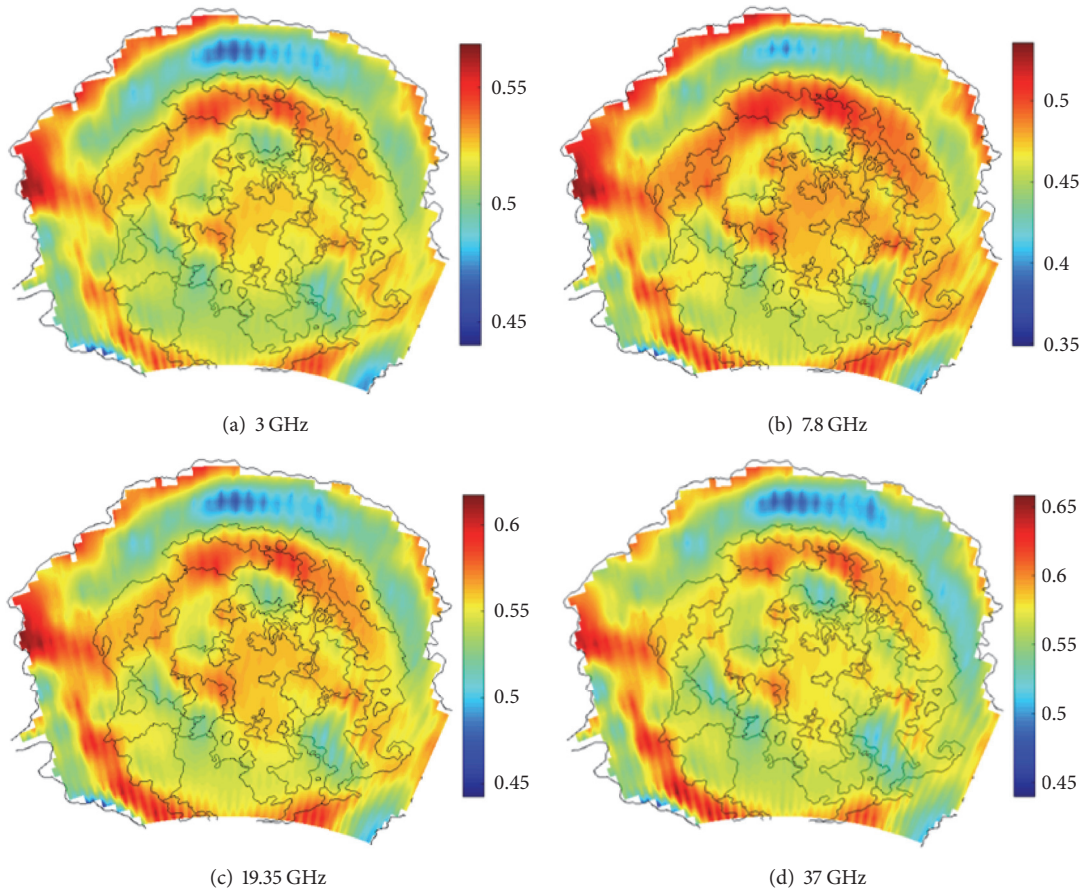


FIGURE 10: Emissivity maps of Schrödinger basin.

nT_B . Even so, much more regions of the unit show considerably low nT_B values, implying that the material of the unit can be represented by the low MTE feature. Zheng et al. [15] and Meng et al. [24] proposed that the low MTE is directly related to the low (FeO + TiO₂) abundance (FTA). This means that the material of the unit will be severely low in FTA. Figure 10 indicates that the unit has a low emissivity, indicating a high density of the material in this unit combined with the relationships expressed by [25].

Unit INsr includes the materials that form the topographic rim crest and the interior wall of Schrödinger basin. But the nT_B in the unit is heavily impacted by the surface topography. At daytime, the nT_B in the north interior wall is lowest within the study area, while the south interior wall indicates the highest nT_B . A similar phenomenon occurs in the nighttime nT_B maps. Such phenomenon also exists in Tycho crater [26, 27], indicating the cold and hot T_B anomalies over the lunar surface. This makes it difficult to recognize the MTE features of the material in this unit.

3.2. Schrödinger Plains Group. The floor of Schrödinger basin is identified as five plains-forming units, including the rugged plains material (INsrp), hummocky plains material (INshp), the lower member of the smooth plains material (Isspl), the

upper member of the smooth plains material (Isspu), and the knobby plains material (Iskp) [2].

Unit INsrp is mainly distributed outside of the peak ring, which is stratigraphically the oldest plains material on the basin floor. The unit shows relatively higher nT_B in the northern, western, and southern parts, while the nT_B changes greatly from north portion to the south and with frequency. The great change of the nT_B performance makes it difficult to recognize the MTE features of the material in this unit.

Unit INshp occupies much of the basin floor along the northern and western walls, and in the south where the peak ring is most discontinuous. The nT_B and emissivity performances of the unit are similar to that of unit INsrp in the close areas, indicating the uniformity of the materials MTE features in the two units.

Unit Isspu primarily occurs in the center of Schrödinger basin, which presents as lower and slightly less cratered than unit Isspl. Interestingly, the unit has the second highest nT_B within the basin floor, which is just lower than the regions with enhanced solar illumination. This indicates that the unit can be represented by the high MTE feature and the material here is fairly high in FTA. Figure 10 indicates that the emissivity is high here, indicating a relatively lower density of the material in this unit.

Unit Isspl is found just inside the peak ring, displaying moderate to high albedo with a small number of superposed craters. Interestingly, nearly in all boundaries between this unit and unit INspr, the nT_B and emissivity differences are not clear. A similar phenomenon also occurs in the boundaries between this unit and unit Isspu. Generally, Figure 10 indicates that the emissivity in most part of the unit is similar to that in unit Isspu, implying the uniformity of the densities of the materials in two units.

Unit Iskp is located along the southern basin wall with fairly high albedo. The nT_B distribution of the unit is obviously affected by the surface topography, which is higher in the southern portion near the south interior wall but lower in the northern portion. Even so, the nT_B is lower than the nearby regions along the same latitude, indicating that the unit should be represented by the low MTE feature. Moreover, the nT_B and emissivity performances of the unit are similar to that of unit Inspr in the close areas, indicating the uniformity of the materials MTE features in the two units.

3.3. Schrödinger Volcanic Formation. Volcanic materials are concentrated in the northern and eastern parts of the basin inside the peak ring. The formation is made up of four patches of dark plains materials unit (Isdp) and dark mantle material unit (Elsdm) [2].

The largest patch of unit Isdp is mainly located along the northern part of the peak ring, and other three patches of this unit are located around unit Elsdm. The unit displays smooth, relatively featureless, low-albedo surfaces. But, not only at nT_B maps but also at emissivity map is the difference between this unit and unit Isspu not clear, indicating the uniformity of the materials MTE features in the two units.

Unit Elsdm is located in the southeastern part of the basin floor within the peak ring, which has a relatively smooth, lightly cratered surface with low albedo. There exists an ovoidal cone, which has been identified as the source of pyroclastic eruptions [7, 28]. In nT_B and emissivity maps, the values in this unit are apparently lower than the nearby unit Isspu, particularly at 3.0 GHz channel, while the nT_B values are apparently higher than those in unit INspr. This not only indicates the difference of the materials MTE features in these regions, but also hints at the applicability of the CELMS data in the high latitude regions.

4. Geological Applications

Figures 7 and 8 postulate a new view about the geological units in Schrödinger basin.

4.1. Potential Geological Applications. The nT_B behaviors present a distinctly different view about Schrödinger basin compared to the visible images.

To basin materials formation, unit INspr indicates the low nT_B and emissivity values, hinting the existence of the materials with high density.

To plains formation, the difference between units INspr and INshp is not clear both in nT_B maps and in emissivity maps. Though the nT_B and emissivity values change greatly

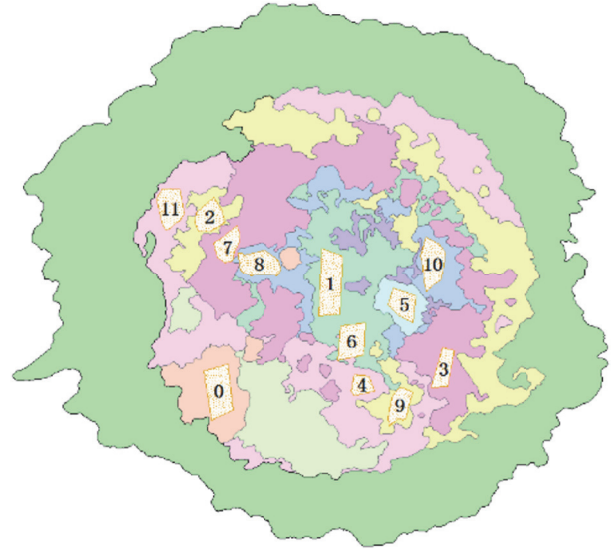


FIGURE 11: Samples for statistics.

from the south to north part of the basin, they show identical features in the close regions. This means the uniformity of the materials in the two units.

Also, the difference between units Isspl and Isspu is not clear, indicating the uniformity of the materials in the microwave range. Additionally, the nT_B and emissivity performances make it difficult to identify the MTE features of units INspr and INshp, but the emissivity values in unit Isspl are apparently higher than those in unit INspr in the southern part of the basin floor, indicating that the materials in units Isspl and Isspu are different from units INspr and INshp.

To volcanic formation, unit Isdp is hard to identify from the unit Isspu in the nT_B and emissivity maps. That is, units Isdp and Isspl indicate the similar nT_B and emissivity performances as unit Isspu, indicating the uniformity of the materials in the three units in microwave range.

Here, unit Elsdm indicates the special nT_B and emissivity performances compared to the other units. The material here is identified as the dark mantle deposit or pyroclastic deposit [2, 29]. Thus, the nT_B and emissivity maps indicate the special thermophysical features of the deposits in high latitude regions.

To better understand the previous expression, the special regions mentioned above are sampled in Figure 11 and the corresponding statistics are presented in Table 1.

Table 1 indicates a small difference in nT_B values among the geological units, indicating some interesting information about the geological units as follows. First, unit INspr represented by Positions 2 and 9 has the highest nT_B values. Interestingly, unit INshp represented by Positions 4, 6, and 11 has similar statistics to unit INspr. Second, unit Isspu represented by Position 1 is lower than that in unit INspr. Third, unit Elsdm represented by Position 5 has the third highest nT_B values. Fourth, unit INspr represented by Positions 3 and 7 apparently has the lowest nT_B values. Finally, the change of the nT_B with frequency in unit Isspl represented by Position

TABLE 1: nT_B statistics of samples at daytime.

Frequency Position	3 GHz		7.8 GHz		19.35 GHz		37 GHz	
	Mean	Std	Mean	Std	Mean	Std	Mean	Std
2	1.0071	0.0020	1.0124	0.0041	1.0177	0.0025	1.0147	0.0034
4	1.0041	0.0008	1.0068	0.0012	1.0082	0.0012	1.0105	0.0017
6	1.0092	0.0010	1.0119	0.0019	1.0120	0.0014	1.0141	0.0020
9	1.0001	0.0054	0.9994	0.0063	0.9997	0.0072	1.0003	0.0074
11	1.0023	0.0095	1.0025	0.0122	1.0013	0.0090	1.0061	0.0069
1	1.0064	0.0016	1.0076	0.0018	1.0078	0.0024	1.0086	0.0036
5	0.9989	0.0018	0.9960	0.0044	0.9973	0.0031	0.9965	0.0046
0	0.9759	0.0027	0.9545	0.0063	0.9596	0.0030	0.9498	0.0034
3	0.9719	0.0066	0.9518	0.0149	0.9542	0.0120	0.9410	0.0172
7	0.9762	0.0055	0.9511	0.0101	0.9555	0.0065	0.9421	0.0080
8	0.9712	0.0069	0.9609	0.0114	0.9630	0.0089	0.9447	0.0120
10	0.9562	0.0060	0.9651	0.0105	0.9640	0.0082	0.9517	0.0102

8 is similar to that of unit INsrp, indicating the difference in material MTE features. Combined with the emissivity map, unit Isspl is consistent with unit Isspu.

Therefore, a new geological understanding about Schrödinger basin can be obtained based on nT_B and emissivity maps and statistics of sample regions (Table 1). Here, at least in microwave range, the basin floor can be categorized into four geological zones. The first zone comprises the previous units INsrp and INshp. The second zone comprises the previous units INspr and Iskp. The third zone includes the previous units Isspl, Isspu, and Isdp. And the fourth zone is unit Eldsm.

The new geological understanding also means that though the surface features are not identical for the nearby geological unit, the MTE parameters of the materials are consistent. However, the strong topographic effect and the rather small nT_B differences among the geological units hint that the CELMS data are not suitable to study the regolith thermophysical features and the mare volcanism in high latitude regions.

4.2. nT_B Anomalies. At least four nT_B anomalies occur in Schrödinger basin. Two anomalies are hot, which mainly include the southern interior wall and the central part of the basin floor. The other two are cold, including the northern interior wall and unit INspr.

Hot and cold T_B anomalies are always an interesting topic in the current lunar study [12, 15, 19, 27, 30, 31], but the causes for the cold anomaly have long been in intense debate. Gong and Jin [32] and Hu et al. [12] attributed the hot and cold T_B anomaly to the existence of the rocks. But Salisbury and Hunt [33] and Meng et al. [27] thought that the surface topography and its orientation are the decisive factors for T_B anomaly. The nT_B behaviors in Schrödinger basin apparently prove the latter explanation, because the cold nT_B anomaly in the northern interior wall obviously resulted from the deficiency of the solar heating in a day, while the hot anomaly in the southern interior wall is apparently brought by the enhanced solar heating. Moreover, combined with the simulation results, the hot anomaly in the regions

around (127.3°E, 72.3°S), (129.0°E, 75.3°S), (134.4°E, 71.6°S), and (143.0°E, 75.2°S) also validates the strong influence of the solar heating on the anomaly of this kind.

However, there also exists another kind of hot and cold anomaly.

Firstly, in the central and southern parts of the basin floor, the nT_B is high no matter at daytime and at midnight, indicating a hot anomaly here. A similar phenomenon also exists in the basin floors of Orientale, Hertzsprung, and Crisium [13, 18, 20]. Using the theoretical model and the CE-2 CELMS data, Meng et al. [13, 20] attributed the hot T_B anomaly to the probably warm substrate.

However, to verify the conclusion, the influence of the surface topography and regolith composition must be eliminated at first. Interestingly, the emissivity maps and the topography both indicate a relatively flat surface in this region, indicating the negligible impact of the topography. Moreover, Meng et al. [24] and Hu et al. [12] suggested the strong influence of the ilmenite content on the local T_B . Similar findings are also proved by the observed CELMS data in Mare Imbrium and Orientale, where the mare basalts with higher ilmenite content indicate a higher T_B at daytime [11, 20]. The regolith in these regions is more mafic than the nearby regions [2], but the nT_B behaviors are opposed to the simulation results by Meng et al. [24] and Hu et al. [12] and observations in Mare Imbrium and Orientale [11, 20]. Thus, the regolith composition also cannot interpret the hot anomaly.

Again, the only left cause for the hot nT_B anomaly is the warm substrate.

Additionally, Lu et al. [34] found two apparent mascons in the central and south parts of Schrödinger basin. The formation of the mascons is always related to the volcanic activity in lower crust or upper mantle [35, 36]. Thus, the existence of the two mascons hints at an ever-existing strong volcanic activity in the deep lunar crust in Schrödinger basin. What is more, there occur abundant fractures in the basin floor, some of which have been proved to be related to the volcanic activity in depth [10]. This is a new evidence of the ever-existed strong tectonic activities in Schrödinger basin.

The hot anomaly, the abundant fractures, and the occurrence of the mascons indicate a new view about the volcanic activity in Schrödinger basin. This may provide some interesting information about the formation of the SPA basin and the mare volcanism of the lunar farside, deserved to be further studied with more sources of data in future.

Secondly, in unit INspr, the nT_B is always lower than the nearby units, while the solar illumination here is not apparently lower than the nearby regions, indicating the existence of a cold anomaly here. The causes for the low nT_B anomaly are still under debate until now.

First, the cold anomaly is obviously not related to the surface topography, for it is widely distributed in the peak ring. Some regions of the peak ring are originating to the solar illumination, while the nT_B here is still rather low.

Second, Gong and Jin [32] and Hu et al. [12] suggested that the rock abundance is responsible for the cold anomaly at night using the theoretical model. They also suggested that the cold anomaly at night should be a hot anomaly at noon. But the nT_B here is low both at daytime and at night, indicating that the rock abundance does not interpret the cold anomaly.

Third, Hu et al. [12] thought the ilmenite content is one of the main causes for the T_B anomalies found in the CELMS map. Also, Meng et al. [13] evaluated the relationship between the nT_B performances in the cold anomalies surrounding Mare Crisium and the corresponding rock abundance and ilmenite content, and the results also hint that a special material with rather low ilmenite should also be responsible for the cold anomaly. Furthermore, the T_B behaviors around Copernicus crater verified that the cold anomaly is likely brought by a special material with rather low ilmenite content [37].

That is, the composition should undertake the main cause for the low nT_B anomaly.

Therefore, the existence of the cold nT_B anomaly in unit INspr indicates that the source material, pyroxene-bearing anorthosite [28], is probably an important cause for the cold anomaly of the lunar surface, which also deserved to be further studied in future.

One more phenomenon should be paid attention to. Such cold anomaly is not only limited in unit INspr. The crater ejecta in the southwest part of the basin floor and just inside the peak ring also shows low nT_B and emissivity values as unit INspr, even if the regions are close to the southern interior wall. Additionally, the nT_B and emissivity in unit Iskp are apparently lower than the vicinity along the same latitude, indicating that the material in this unit should be represented by low values. The nT_B and emissivity in the northern part of unit Iskp are also similar to unit INspr. The crater ejecta represents the materials from the depth layer. Therefore, combined with the previous discussions, this phenomenon means that the materials in the depth layer of the basin floor excavated by the crater are similar to the peak ring. This is helpful to better understand the formation of Schrödinger basin and even the SPA basin according to the crater formation mechanism, which deserves to be further studied with more sources of data and even in situ observations.

5. Conclusions

In this paper, the nT_B maps derived from CE-2 CELMS data were systematically used to study the microwave thermophysical features of Schrödinger basin, which give some different aspects compared to the previous understandings. The main results are as follows.

(1) The geological units are reevaluated with the CE-2 CELMS data and the statistics of typical regions, which shows a different geological perspective compared to the visible results.

(2) The nT_B anomalies in the interior basin wall indicate the strong influence of the topography and its orientation.

(3) The hot nT_B anomaly in the basin floor indicates the likely warm substrate. Combined with the existence of the mascons and abundant floor fractures, the strong tectonic activity should ever exist in Schrödinger basin, which will be helpful to improve understanding the formation of the Schrödinger basin and even the SPA basin.

(4) The cold nT_B anomaly in unit INspr indicates that the pyroxene-bearing anorthosite is probably an important cause for the cold anomaly over the lunar surface.

Generally, the CELMS data are feasible to study the thermophysical features of the geological units in high latitude regions to some extent, which will expand our knowledge about the south and north poles. However, the surface topography strongly alters the T_B and nT_B performances, and more work should be done to further understand the important findings in this study.

Data Availability

The CELMS data can be downloaded from the website <http://www.clep.org.cn/>. The processed CELMS data and the brightness temperature maps about Schrödinger basin can be freely shared by email.

Conflicts of Interest

The authors declare that there are no conflicts of interest regarding the publication of this paper.

Acknowledgments

The authors express their gratitude to the National Natural Science Foundation of China under Grants [41490633, 41590851, and 41802246], the opening fund of State Key Laboratory of Lunar and Planetary Sciences (Macau University of Science and Technology) [No. 119/2017/A3], and the Science and Technology Development Fund of Macau [Grant 0012/2018/A1]. Thanks are also due to the graduate Lele Hou for preparing the resulting images of the manuscript. The WAC image was downloaded from <http://wms.lroc.asu.edu/lroc/search>.

References

- [1] P. D. Spudis, "Early crustal evolution. book reviews: the geology of multi-ring impact basins. the moon and other planets," *Science*, vol. 264, pp. 1180-1181, 1994.

- [2] S. C. Mest, "The geology of Schrödinger basin: insights from post-Lunar Orbiter data," *Geological Society of America*, vol. 477, pp. 95–115, 2011.
- [3] I. Garrick-Bethell and M. T. Zuber, "Elliptical structure of the lunar South Pole-Aitken basin," *Icarus*, vol. 204, no. 2, pp. 399–408, 2009.
- [4] K. Uemoto, M. Ohtake, J. Haruyama et al., "Purest anorthosite distribution in the lunar South Pole-Aitken basin derived from SELENE multiband imager," in *Proceedings of the 41st Lunar and Planetary Science Conference*, 2010.
- [5] D. A. Kring, G. Y. Kramer, and P. W. K. Potter, "Interpreting the depth of origin of the Schrödinger peak ring and implications for other impact basins," *Lpi Contributions*, 2013.
- [6] D. E. Wilhelms, K. A. Howard, and H. G. Wilshire, "USGS Map I-1162 US Geological Survey," Washington, DC, USA, 1979.
- [7] E. M. Shoemaker, M. S. Robinson, and E. M. Eliason, "The south pole region of the moon as seen by Clementine," *Science*, vol. 266, no. 5192, pp. 1851–1854, 1994.
- [8] B. Shankar, G. R. Osinski, I. Antonenko, and C. D. Neish, "A multispectral geological study of the schrödinger impact basin," *Canadian Journal of Earth Sciences*, vol. 50, no. 1, pp. 44–63, 2013.
- [9] G. Y. Kramer, D. A. Kring, A. L. Nahm, and C. M. Pieters, "Spectral and photogeologic mapping of Schrödinger Basin and implications for post-South Pole-Aitken impact deep subsurface stratigraphy," *Icarus*, vol. 223, no. 1, pp. 131–148, 2013.
- [10] P. S. Kumar, U. Sruthi, N. Krishna et al., "Recent shallow moonquake and impact-triggered boulder falls on the Moon: New insights from the Schrödinger basin," *Journal of Geophysical Research Planets*, vol. 121, no. 2, pp. 147–179, 2016.
- [11] Z. Meng, S. Hu, T. Wang, C. Li, Z. Cai, and J. Ping, "Passive microwave probing mare basalts in mare imbrium using CE-2 CELMS data," *IEEE Journal of Selected Topics in Applied Earth Observations and Remote Sensing*, vol. 11, no. 9, pp. 3097–3104, 2018.
- [12] G. P. Hu, R. Bugiolacchi, K. L. Chan, Y. C. Zheng, and K. T. Tsang, "A new map of thermal variations within Oceanus Procellarum and Mare Imbrium using Chang'e (CE-2) microwave radiometers (MRMs) data," in *Proceedings of the 49th Lunar and Planetary Science Conference*, 2018.
- [13] Z. G. Meng, H. H. Wang, X. Y. Li et al., "Potential geological significations of Crisium basin revealed by CE-2 CELMS data," *International Archives of the Photogrammetry, Remote Sensing and Spatial Information Sciences*, vol. 42, no. XLII-3, pp. 1279–1284, 2018.
- [14] W. G. Zhang, J. S. Jiang, H. G. Liu et al., "Distribution and anomaly of microwave emission at Lunar South Pole," *Science China Earth Sciences*, vol. 53, no. 3, pp. 465–474, 2010.
- [15] Y. C. Zheng, K. T. Tsang, K. L. Chan et al., "First microwave map of the Moon with Chang'E-1 data: the role of local time in global imaging," *Icarus*, vol. 219, no. 1, pp. 194–210, 2012.
- [16] Z. G. Meng, Y. Xu, Z. C. Cai, S. B. Chen, Y. Lian, and H. Huang, "Influence of lunar topography on simulated surface temperature," *Advances in Space Research*, vol. 54, no. 10, pp. 2131–2139, 2014.
- [17] Z. Cai, T. Lan, and C. Zheng, "Hierarchical MK splines: algorithm and applications to data fitting," *IEEE Transactions on Multimedia*, vol. 19, no. 5, pp. 921–934, 2017.
- [18] Z. Meng, Q. Wang, H. Wang, T. Wang, and Z. Cai, "Potential geologic significances of hertzprung basin revealed by CE-2 CELMS data," *IEEE Journal of Selected Topics in Applied Earth Observations and Remote Sensing*, vol. 11, no. 10, pp. 3713–3720, 2018.
- [19] K. L. Chan, K. T. Tsang, B. Kong, and Y.-C. Zheng, "Lunar regolith thermal behavior revealed by Chang'E-1 microwave brightness temperature data," *Earth and Planetary Science Letters*, vol. 295, no. 1-2, pp. 287–291, 2010.
- [20] Z. Meng, J. Zhang, Z. Cai, J. Ping, and Z.-S. Tang, "Microwave thermal emission features of mare orientale revealed by CELMS data," *IEEE Journal of Selected Topics in Applied Earth Observations and Remote Sensing*, vol. 10, no. 6, pp. 2991–2998, 2017.
- [21] L. He, L. Lang, Q. Li, and W. Zheng, "Effect of surface roughness on microwave brightness temperature from lunar surface: numerical analysis with a hybrid method," *Advances in Space Research*, vol. 51, no. 1, pp. 179–187, 2013.
- [22] G. P. Hu, Y. C. Zheng, A. A. Xu, and Z. S. Tang, "Lunar surface temperature of global moon: preparation of database with topographic and albedo effects," *IEEE Geoscience and Remote Sensing Letters*, vol. 13, no. 1, pp. 110–114, 2016.
- [23] G. P. Hu, Y. C. Zheng, A. A. Xu, and Z. S. Tang, "Qualitative verification of CE-2's microwave measurement: relative calibration based on brightness temperature model and data fusion," *IEEE Transactions on Geoscience and Remote Sensing*, vol. 54, no. 3, pp. 1598–1609, 2016.
- [24] Z. G. Meng, G. D. Yang, J. S. Ping et al., "Influence of (FeO+TiO₂) abundance on the microwave thermal emissions of lunar regolith," *Science China Earth Sciences*, vol. 59, no. 7, pp. 1498–1507, 2016.
- [25] G. H. Heiken, D. T. Vaniman, and B. M. French, *A User's Guide to the Moon*, Cambridge Univ. Press, London, UK, 1991.
- [26] R. W. Shorthill and J. M. Saari, "Nonuniform cooling of the eclipsed moon: a listing of thirty prominent anomalies," *Science*, vol. 150, no. 3693, pp. 210–212, 1965.
- [27] Z. G. Meng, R. Zhao, Z. C. Cai et al., "Microwave thermal emission at Tycho area and its geological significance," *IEEE Journal of Selected Topics in Applied Earth Observations and Remote Sensing*, vol. 10, no. 6, pp. 1–7, 2017.
- [28] L. R. Gaddis, M. I. Staid, J. A. Tyburczy, B. R. Hawke, and N. E. Petro, "Compositional analyses of lunar pyroclastic deposits," *Icarus*, vol. 161, no. 2, pp. 262–280, 2003.
- [29] D. A. Kring, G. Y. Kramer, G. S. Collins, R. W. K. Potter, and M. Chandnani, "Peak-ring structure and kinematics from a multi-disciplinary study of the Schrödinger impact basin," *Nature Communications*, Article ID 13161, 2016.
- [30] Z. G. Meng, L. Cui, T. X. Wang, Z. C. Cai, and J. S. Ping, "Cold behavior of moon surface demonstrated by typical copernican craters using CE-2 CELMS data," in *Proceedings of the International Geoscience and Remote Sensing Symposium*, IEEE, July 2018.
- [31] B. C. Murray and R. L. Wildey, "Surface temperature variations during the lunar nighttime," *The Astrophysical Journal*, vol. 139, no. 5, pp. 734–750, 1964.
- [32] X. H. Gong and Y. Q. Jin, "Diurnal change of thermal emission with 'hot spots' and 'cold spots' of fresh lunar craters observed by Chinese Chang'E-1," *Scientia Sinica*, vol. 42, no. 8, p. 923, 2012.
- [33] J. W. Salisbury and G. R. Hunt, "Infrared images of Tycho on dark moon," *Science*, vol. 155, no. 3766, pp. 1098–1100, 1967.
- [34] Y. Lu, J. S. Ping, and V. V. Shevchenko, "Volcanic activity of the Mare Moscoviense and Schrödinger basin," in *Proceedings of the Lunar and Planetary Science Conference*, 2013.
- [35] P. D. Spudis, B. Bussey, J. Plescia, J.-L. Joset, and S. Beauvivre, "Geology of shackleton crater and the south pole of the moon," *Geophysical Research Letters*, vol. 35, no. 14, pp. 63–72, 2008.

- [36] A. J. Dombard, S. A. Hauck II, and J. A. Balcerski, "On the origin of mascon basins on the Moon (and beyond)," *Geophysical Research Letters*, vol. 40, no. 1, pp. 28–32, 2013.
- [37] Z. G. Meng, X. Y. Li, S. B. Chen et al., "Thermophysical features of shallow lunar crust demonstrated by typical Copernican craters using CE-2 CELMS data," *IEEE Journal of Selected Topics in Applied Earth Observations and Remote Sensing*, vol. 99, pp. 1–10, 2019.

Research Article

Disk-Integrated Lunar Brightness Temperatures between 89 and 190 GHz

Martin J. Burgdorf ¹, Stefan A. Buehler,¹ Imke Hans,² and Marc Prange¹

¹Universität Hamburg, Faculty of Mathematics, Informatics and Natural Sciences, Department of Earth Sciences, Meteorological Institute, Bundesstraße 55, 20146 Hamburg, Germany

²EUMETSAT, Eumetsat Allee 1, 64295 Darmstadt, Germany

Correspondence should be addressed to Martin J. Burgdorf; martin.burgdorf@uni-hamburg.de

Received 30 November 2018; Revised 7 March 2019; Accepted 2 May 2019; Published 2 June 2019

Guest Editor: Zhiguo Meng

Copyright © 2019 Martin J. Burgdorf et al. This is an open access article distributed under the Creative Commons Attribution License, which permits unrestricted use, distribution, and reproduction in any medium, provided the original work is properly cited.

Measurements of the disk-integrated brightness temperature of the Moon at 89, 157, 183, and 190 GHz are presented for phase angles between -80° and 50° relative to full Moon. They were obtained with the Microwave Humidity Sounder (MHS) on NOAA-18 from 39 instances when the Moon appeared in the deep space view of the instrument. Polynomials were fitted to the measured values and the maximum temperature and the phase angle of its occurrence were determined. A comparison of these results with the predictions from three different models or rather parametrical expressions by Keihm, Mo & Kigawa, and Yang et al. revealed significantly larger phase lags for the lower frequencies in the measurements with MHS. As the Moon has appeared thousands of times in the field of view of all microwave sounders combined, this investigation demonstrates the potential of weather satellites for fine tuning models and establishing the Moon as extremely accurate calibration reference.

1. Introduction

In the year 1998 the first member of the fifth generation of satellites for Earth observation on polar orbits was launched by the National Oceanic and Atmospheric Administration (NOAA): NOAA-15. It carried two new microwave instruments, viz., AMSU-A and AMSU-B (Advanced Microwave Sounding Unit-A/B). When analyzing the data of AMSU-A, it became apparent that the calibration of this instrument is occasionally corrupted by the presence of the Moon in its field of view [1]. This is because AMSU-A points during every scan not only at Earth but also at an internal calibration target (ICT) of known temperature and into deep space. An interpolation between the counts from either reference source allows the calculation of the flux received from the Earth scenes. Sometimes it happens that the Moon is at the very position in the sky where AMSU-A or -B is observing space as cold reference for calibration (see Figure 1). As the instrument receives in this case the radiation of the Moon on top of the cosmic background radiation, it produces too high an output signal, which causes on its part a too low value for the gain of the receiver.

Mo & Kigawa [1] derived an effective brightness temperature (T_B) of the Moon as a function of phase angle from the intrusions of the Moon in the deep space view (DSV) of AMSU-A on NOAA-18. Their (4) is a rather rough approximation, where the disk-integrated T_B is the same for all frequencies, and it reaches its maximum value at full Moon. Since the 1960s, however, it is known that the maximum temperature of the Moon as measured in the wavelength range between 0.4 and 9.6 cm, corresponding to the frequency range 75–3.1 GHz, has a significant phase shift [2]. It is due to the fact that the radiation does not originate in the top layer of the surface, but it is rather emitted from a depth of tens of cm, where the heating from the Sun is delayed. AMSU-A covers a frequency range of 23.8–89 GHz; i.e., the phase shift found with ground-based observations of the Moon should be present in the data from the satellite as well.

Yang et al. [4] carried out a similar investigation with the Advanced Technology Microwave Sounder (ATMS) on the SNPP (Suomi National Polar-orbiting Partnership) satellite. They found a somewhat different relationship between phase angle and brightness temperature, which they assumed to

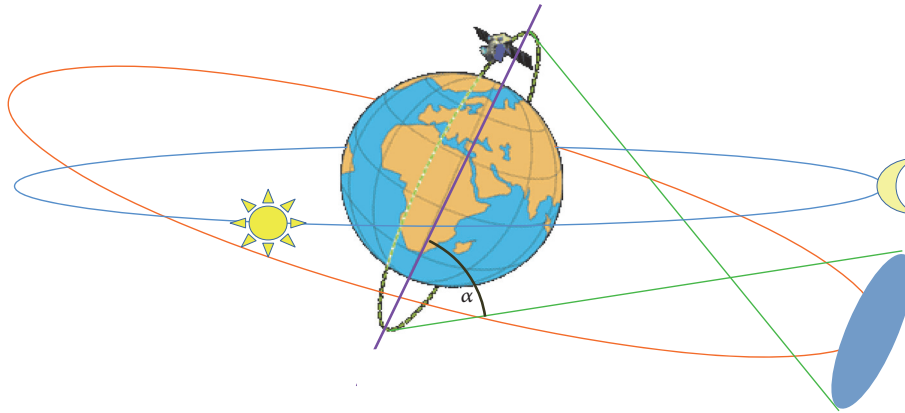


FIGURE 1: Pointing direction of the deep space view (green) compared to the celestial equator (red) and the ecliptic (blue). The slight tilt of the Moon's orbit against the ecliptic and of the orbital axis of the weather satellite against the equator is not shown for the sake of simplicity. The DSV points some 75° away from nadir—angle α in (3)—and describes a circle in the sky during an orbit of the satellite. When the Moon touches this circle, it appears in the DSV [3].

reach its maximum, however, again at full Moon. An important detail of these investigations is that the observations of the Moon were limited in both cases to phase angles φ between -75° and -60° relative to the full Moon. The reason is that both NOAA-18 before the year 2008 and SNPP crossed the equator in northern direction at about 13:30 local time. As the Moon can only appear in the DSV when it is positioned close to the orbital axis of the artificial satellite and more than 90° away from the Sun, the equator crossing time puts a tight constraint on the phase angles suitable for observation. This is shown schematically in Figure 1.

NOAA-18 changed its local equator crossing time between the years 2008 and 2018 by more than six hours. This peculiarity makes it possible now to calculate the brightness temperature of the Moon over a range of phase angles larger than 125° by analyzing its intrusions in the DSV of MHS (Microwave Humidity Sounder) on this satellite. As these measurements were carried out with both waxing and waning Moon, they allowed determining the phase angle of maximum brightness temperature with high accuracy for all channels of MHS, i.e., 89, 157, 183, and 190 GHz.

2. Materials and Methods

2.1. Identification of Moon's Presence in the Centre of the DSV. The first step on the way of calculating the brightness temperature of the Moon was to find its intrusions in the DSV of MHS on NOAA-18. Compared to other microwave sounders and other satellites, this one is particularly suited for this purpose because of the following reasons:

- (i) MHS on NOAA-18 is recommended by FIDUCEO (<http://www.fiduceo.eu>) (FIDelity and Uncertainty of Climate data records from Earth Observations) and GSICS (<https://gsics.wmo.int/en/welcome>) (Global Space-based Inter-Calibration System) for use as reference instrument. Systematic calibration errors of other instruments are identified by comparison to this

one. This means that the photometric stability of MHS on NOAA-18 is very high.

- (ii) NOAA-18 was launched on May 20, 2005. All channels of MHS on this satellite worked flawlessly until 20 October 2018, when the scan mechanism failed.
- (iii) As mentioned above, NOAA-18 turned from an afternoon to a morning satellite. This means that NOAA-18 provided data from a large range of phase angles around full Moon.
- (iv) MHS has a smaller field of view than AMSU-A and therefore achieves a better signal-to-noise ratio with its observations of the Moon.

The method for identifying the Moon intrusions in the DSV was described in detail in Burgdorf et al. [5]. It starts with calculating the minimum distance between the pointing direction of the DSV and the position of the Moon for all orbits of the whole mission with a program called *mhscl* that is part of AAPP (ATOVS [Advanced TIROS {Television and Infrared Observation Satellite} Operational Vertical Sounder] and AVHRR [Advanced Very High Resolution Radiometer] Pre-processing package). In the first step, events, where this distance is a small fraction of a degree, are selected. There is an uncertainty, however, of about 0.3° in the calculated pointing direction and a discrepancy of similar size in the alignment of the different channels [6]. Hence, in the second step, we have taken advantage of the fact that in every scan there are four measurements of the signal from deep space at slightly different directions, each of them with its own "light" curve, i.e., the signal s as a function of time t as the DSV moves over the Moon in the cross-scan direction (see Figure 1 in [6]). Considering those intrusions, where the Moon gave the maximum signal in the DSV pixel with number $n = 2$ or 3 , and identifying those instances, where it gave almost the same signal in the neighbouring DSV pixels $n-1$ and $n+1$, we obtained a collection of events, where the Moon came closer than 0.1° to the centre of DSV n . This way we made sure that the maximum signal was measured with

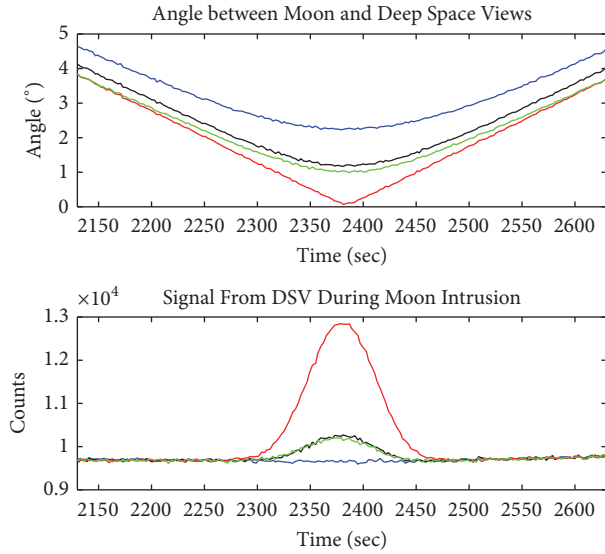


FIGURE 2: Moon intrusion event in different deep space views on 15 November 2010, with channel H1 of MHS on NOAA-18; blue: DSV 1; black: DSV 2; red: DSV 3; green: DSV 4. Top: angle between Moon and space view as calculated with AAPP. Bottom: space view counts. The time is given in seconds after 17:23 UT, the time of the first scan in the raw data file (level 1b). The angles calculated with AAPP are not quite accurate, and this is why DSV 2 gives a slightly larger signal than DSV 4 [7].

the Moon always at the same position in the beam pattern (see Figure 2).

2.2. Evaluation of the “Light” Curve Produced by the Presence of the Moon in the DSV. The “light” curve can be well fitted with a Gaussian in MATLAB (see Figure 3):

$$s = ae^{-((t-b)/c)^2} \quad (1)$$

where a is the amplitude, b is the centroid (Moon closest to centre of DSV), and c is related to the peak width. The relationship between c and the full duration at half maximum ($FDHM$) of the intrusion of the Moon in the DSV is

$$FDHM = 2\sqrt{\ln 2}c \quad (2)$$

a is the number of counts when the Moon is closest to the centre of the beam.

As the reference sources used for calibration—the internal blackbody and the cosmic microwave background—are quite extended, while the Moon fills only a fraction of the field of view of MHS, it is necessary to know the beam size with high accuracy. The full width at half maximum ($FWHM$) has been measured during the ground tests of MHS at DASA with an alleged accuracy of 0.01° , according to [8]. Employing these values in the calculation of the brightness temperature of the Moon, however, produces discrepancies between the sounding and the window channels too large to be explained by the differences in frequency (the $FWHM$ claimed by DASA implies a *maximum* disk-integrated T_B^{Moon} , i.e., soon after full Moon, of only 210 K at 183 GHz). We have therefore

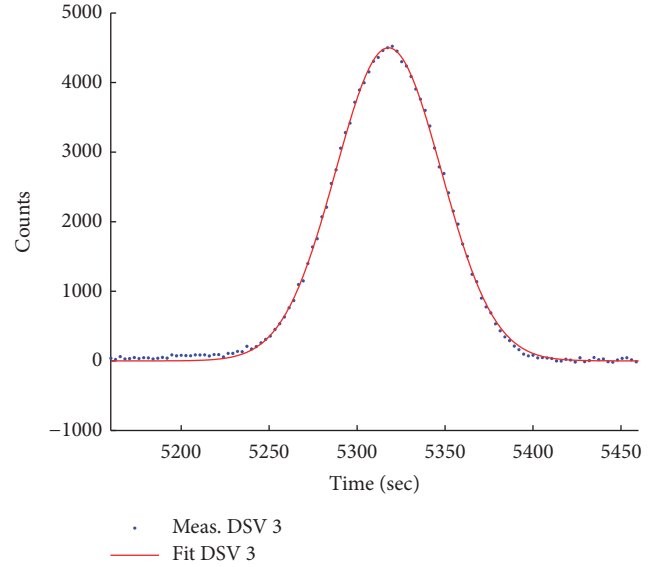


FIGURE 3: Moon intrusion event in deep space view 3 on 29 September 2018 (last Moon intrusion considered), with channel H1 of MHS on NOAA-18; blue dots: measured signal from each scan; red line: Gaussian fit to the measured points. The “light” curve resembles very closely a Gaussian.

determined $FWHM_{ch}$ for each channel of MHS from the width of the Gaussians fitted to the “light” curve of the Moon intrusions in the DSV. The relationship between these physical quantities is

$$FWHM_{ch} = \frac{360^\circ \cdot 2 \cdot \sqrt{\ln 2} \cdot c \cdot \cos \alpha}{P} \quad (3)$$

The elements of this equation are defined as follows:

- (i) α = angular distance between the pointing direction of the DSV and the orbital plane of NOAA-18 (72.1° for pixel 1, 73.2° for pixel 2, 74.3° for pixel 3, 75.4° for pixel 4, the orientation of the DSV is always away from the Sun, see Figure 1);
- (ii) P = orbital period of NOAA-18 (6078 sec).

Equation (3) is basically the same as the second equation in [9], with an orbital angular velocity of $360^\circ \cos \alpha / P$ and the peak width replacing the channel displacement.

We assume in the following that the beam of MHS is rotationally symmetric; i.e., that the $FWHM$ we have determined in the cross-scan direction is the same as the $FWHM$ in the scan direction, which one cannot determine with high accuracy from the Moon intrusions. This assumption is justified by the characterization of the shape of the beam that was carried out on ground [8].

Equation (3) might slightly overestimate $FWHM_{ch}$, because the Moon is an extended source and has therefore a longer presence in the DSV than a point-like object. As the diameter of the Moon is less than half the $FWHM$ (or Θ_{3dB} , as it is called in the reports of the ground tests) of the beam of MHS (see Table 1), however, and the origin of its flux is concentrated in the warmest region of its surface

TABLE 1: Antenna performance—space view—centre frequencies (values from [8], except for the last column, where values were calculated for a point-like lunar emission and, in brackets, a $FWHM_{Moon}$ of 0.4°).

Channel	Ground test frequency [GHz]	Beam efficiency	$\Theta_{3dB} [^\circ]$ (ground test)	$\Theta_{3dB} [^\circ]$ (Moon)
H1	89.3	0.941±0.001	1.09±0.01	1.20(1.13)±0.02
H2	157.3	0.997±0.001	1.03±0.01	1.09(1.01)±0.02
H34	184.3	0.971±0.001	1.05±0.01	1.25(1.18)±0.01
H5	190.6	0.961±0.001	1.05±0.01	1.27(1.20)±0.01

(see, for example, figures in [10]), any systematic error in (3) must be small. We assume $FWHM_{Moon} = 0.4^\circ$ for the radiance distribution of the lunar disk. This value is representative for phases close to full Moon, at quarter Moon it would be smaller. The values for $(FWHM_{ch}^2 - FWHM_{Moon}^2)^{0.5}$, i.e., the beam size after correction for the fact that it was determined with an extended source instead of a point source, are given in brackets in the last column of Table 1. Only $FWHM_{Moon} \approx 0.4^\circ$ results in beam sizes that are compliant with specifications ($1.1^\circ \pm 0.11^\circ$) for each channel. But whatever the error of our value for Θ_{3dB} is, it is the same for all measurements and does therefore not affect the ratio between brightness temperatures at different phase angles.

2.3. Calibration of the Measurements Made with the DSV of MHS on NOAA-18. As intrusions of the Moon in the DSV are not suitable for the standard processing of data obtained with MHS, we started the calculation of brightness temperatures with the output signal expressed in digital counts that is available in the level 1b database. A polynomial of degree two was fitted to the counts from the DSV as a function of time before and after the appearance of the Moon and then used to calculate the counts that would have been obtained, if the Moon had not been present, i.e., only from the cosmic microwave background. These counts and the ones obtained on the ICT in combination with the known temperatures of the cosmic microwave background and the ICT were then used to calculate a linear relationship between counts and spectral radiance. A “cold load correction factor” of 0.24 K, as given in the file `mhs_clparams.dat` of AAPP, was added. No warm load or band correction was applied, because they were considered negligible on the basis of the values given in AAPP. See [11] for a detailed discussion of these and other instrumental effects.

The Gaussian is fitted to the light curve of the Moon in counts from the DSV after subtraction of the “baseline” with the polynomial determined in the previous step. This way not only the contribution from the cosmic microwave background is removed, but also the slightly variable thermal emission from the mirror [12] and the platform. It can be seen from Figure 2, where the raw counts before subtraction of the baseline flux are plotted, that the in-orbit variations are quite small and variable on time scales much larger than the duration of the Moon intrusion. Every light curve we used was carefully inspected for sudden jumps in the counts, which, however, happened only very rarely.

The amplitude of the Gaussian fit is divided by the gain of the relevant channel and the fraction of the field of view covered by the Moon, under the assumption that the beam

can be described by a two-dimensional Gaussian function, and the Moon moves through the centre of the pixel. In this case the fraction of the beam covered by the Moon F_{ch} follows from (1) by replacing time with distance from the centre of the beam r and integration of the beam pattern over the area covered by the Moon:

$$F_{ch} = \frac{1}{2\pi} \int_0^{r_{Moon}/c} \int_0^{2\pi} e^{-r^2/2} r d\omega dr = - \left[e^{-r^2/2} \right]_{r=0}^{r_{Moon}/c} \quad (4)$$

2π is the value of the integral with upper border $r = \infty$. Equation (4) is only valid at one point of the “light” curve: its maximum. With F_{ch} it is possible to calculate the spectral radiance of the Moon:

$$B_\nu^{Moon} = \frac{a}{G\eta F_{ch}} + B_\nu^{CMB} \quad (5)$$

The elements of these equations are defined as follows:

- (i) $B_\nu^{Moon/CMB}$ = spectral radiance of the Moon/cosmic microwave background;
- (ii) G = gain of the instrument in counts per unit of spectral radiance;
- (iii) η = beam efficiency as measured on ground [8];
- (iv) F_{ch} = fraction of the beam covered by the Moon = $e^{4 \ln 2 r_{Moon}^2 / FWHM_{ch}^2} - 1$, derived from (2) and (4);
- (v) r_{Moon} = radius of the Moon as seen from the spacecraft at the time of maximum signal.

F_{ch} , just like G and η , takes slightly different values with different channels, except for three and four, which share the same “quasi-optical” path in MHS.

Equation (5) contains a term to correct for the part of the cosmic microwave background being blocked by the Moon, when an intrusion happens. It is needed, because the full microwave background was subtracted before the amplitude a of the “light” curve was calculated; see Figure 3. This way we make sure that B_ν^{Moon} cannot be negative, even in the hypothetical case of a Moon that does not emit any microwaves. The resulting spectral radiance is then converted to the brightness temperature of the Moon with an inverse Planck function.

3. Results and Discussion

3.1. Brightness Temperatures as a Function of Phase Angle. The brightness temperatures calculated with (5) and the inverse Planck function are plotted as a function of phase angle in

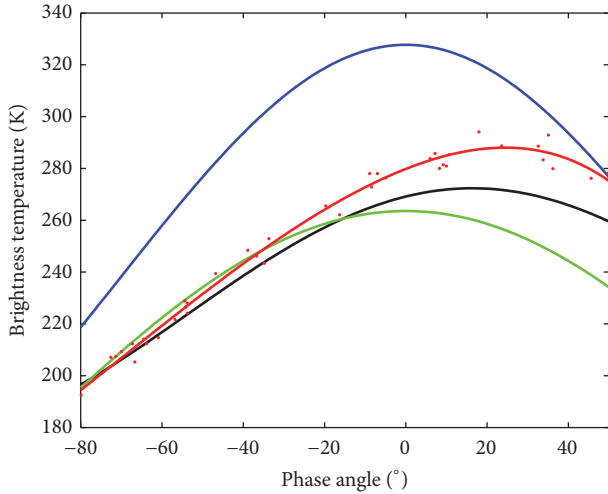


FIGURE 4: Disk-integrated brightness temperatures of the Moon for different phase angles relative to full Moon at 89 GHz. Blue: (4) in [1], green: (4) and Table II in [4], black: Keihm ([13], numbers from web page and personal communication), and red: MHS on NOAA-18, single measurements (dots) fitted with polynomial of order five.

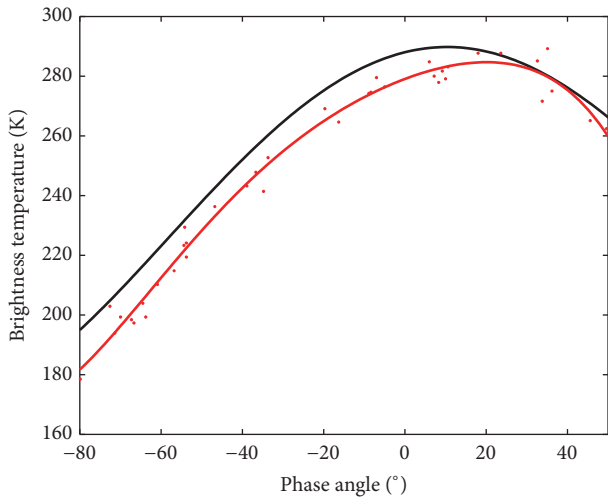


FIGURE 5: Disk-integrated brightness temperature of the Moon for different phase angles relative to full Moon at 157 GHz. Black: Keihm ([13], numbers from web page and personal communication); red: MHS on NOAA-18, single measurements (dots) fitted with polynomial of order five.

Figures 4–6. A polynomial of degree five was fitted to the measured values and is shown together with the predictions of three different models. These models are as follows:

- (i) Keihm [13]: a lunar regolith model, including depth and temperature dependencies of the relevant thermal and electrical properties, whose brightness temperatures are available on a web page (<http://lunar-model-brightness-temperatures.net>) or by request.

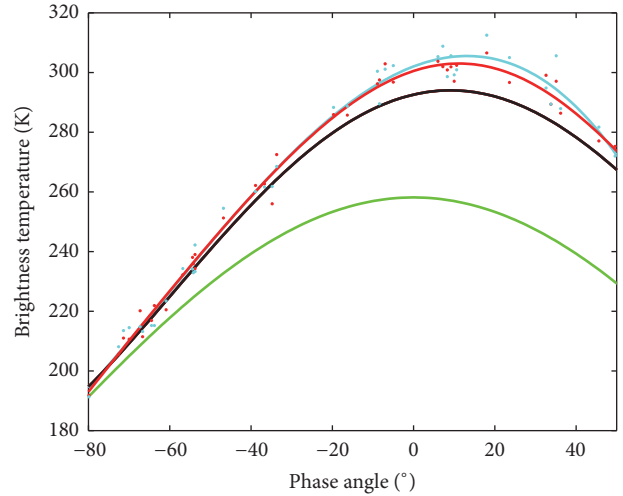


FIGURE 6: Disk-integrated brightness temperature of the Moon for different phase angles relative to full Moon. Green: Equation (4) and Table II in [4], 183.3 GHz, black: Keihm ([13], numbers for 183.3 GHz from web page and personal communication), red: MHS on NOAA-18, 183.3 GHz, and cyan: MHS on NOAA-18, 190.3 GHz, single measurements (dots) fitted with polynomial of order five.

- (ii) Mo & Kigawa [1]: a simple expression for the effective lunar surface brightness temperature for correcting the lunar contamination in AMSU-A data.
- (iii) Yang et al. [4]: a polynomial of degree two in $\cos \varphi$, similar to the one employed by Mo & Kigawa that is based on observations from the Diviner Lunar Radiometer Experiment and takes a wavelength-dependent surface emissivity of the Moon's disk into account.

According to (4) in [1], the effective Moon brightness temperature is the same for all channels of AMSU-A, i.e., in the range 23.8–89 GHz. As this assumption is certainly not valid for higher frequencies [14], we have plotted the values from this model only in Figure 4. The surface emissivity is, however, a factor in (4) of [4] and was therefore calculated for both channels that ATMS has in common with MHS, i.e., at 89 and 183.3 GHz.

The measured values for the brightness temperature in different channels and at different lunar phases, shown as dots in Figures 4–6, have uncertainties that can be calculated from the random scatter around the polynomial fit. We obtained a standard deviation of 3.2 K for the measurements in channel 1, 4.1 K for channel 2, 3.8 K for the average of channels 3 and 4, and 5.1 K for channel 5. These values are significantly larger than the noise of the receivers alone [15], given the fact that each point in the plots is the result of a Gaussian fit to measurements from about 100 different scans (see Figure 3). But it is only the measurements near the centroid that strongly constrain the amplitude of this fit, and even small outliers in the raw data can introduce an error.

A correlation of the scatter of the measurements with the liberation of the Moon or its distance from the Sun could not be found. If such a dependency exists, it must be negligible compared to the random uncertainty of the measurements.

TABLE 2: Maximum brightness temperature of the Moon at different frequencies and the phase of its occurrence.

Source	T_{89} [K]	Φ_{89}	T_{157} [K]	Φ_{157}	T_{183} [K]	Φ_{183}
Keihm	272±14	16°	290±15	10°	294±15	9°
Mo & Kigawa	328	0°	-	-	-	-
Yang et al.	264	0°	-	-	255	0°
MHS on N-18	288±4	24°	285±6	20°	303±5	11°

3.2. *Main Features of the Measurements with MHS on NOAA-18 and Models.* The relationship between the brightness temperature of the Moon and its phase as given by the measurements with MHS and the models is characterized by two key quantities: the maximum brightness temperature, averaged over the disk, and the phase lag between full Moon and the occurrence of this maximum temperature. Table 2 gives an overview of these values.

The uncertainties of the measured brightness temperatures in Table 2 were calculated from the scatter of the values for the diameter of the beam of each channel that were determined from the Moon intrusions in the DSV themselves, as explained above. The beam efficiency η , which is an expression for the losses of the main beam due to side lobes and which we took at face value from [8], contributes an additional, systematic uncertainty to the brightness temperatures measured with MHS. It should be less crucial than the uncertainty of the beam width, however, because η must be close to one and does not enter the calculation of the radiance in quadrature. The absolute uncertainty of the Apollo-based model predictions was calculated on the basis of the estimate given on Keihm's web page.

All things considered there are no significant differences between the maximum brightness temperatures obtained with MHS and the model by Keihm [13]. The mathematical expression given by Yang [4] for the maximum brightness temperature of the disk-integrated Moon, however, is not compatible with the values obtained with MHS on NOAA-18 at 183 GHz, and the same is true for the estimate provided by Mo & Kigawa [1] at 89 GHz.

With respect to the phase shift between full Moon and the time of maximum microwave brightness temperature, the measurements with MHS gave significantly higher values than all models, except for the one by Keihm at 183 GHz. It is noted that assuming a different beam diameter or efficiency has almost no effect on the phase lags measured with MHS, since they affect essentially all measurements the same way. Because of the excellent stability of MHS on NOAA-18 [16], the uncertainty of the phase lags is mainly due to the random scatter of the measurements.

4. Conclusions

Our investigation has produced two major, new findings:

- (1) The difference in beam size between the sounding channels and H2 is almost ten times as large as the value measured with the ground tests that were supposed to demonstrate the compliance with the requirements for MHS on NOAA-18. This is of particular relevance for the verification and check out

of MHS on Metop-C, which was launched on 7 Nov 2018, because it shows that the beam size has to be verified in flight.

- (2) The phase angle of the Moon, where the disk-integrated brightness temperature reaches its maximum, is at the lower frequencies larger than each of the models predicted, hence they do not reproduce the difference between waxing and waning Moon correctly. This is particularly relevant for the model by Keihm, because it is supposed to be used for the calibration of astronomical observations.

On top of that our investigation demonstrates that precise measurements from weather satellites can provide useful information also about objects other than Earth.

At 183.3 GHz, the frequency of the H₂O absorption at the $3_{1,3} \rightarrow 2_{2,0}$ resonance, there is agreement within the margins of uncertainty between the observations with MHS and the model by Keihm. This confirms the validity of the method employed to turn raw data from the deep space view into brightness temperatures. By the same token it is an additional proof for the existence of the microwave phase lag, which is absent in those functions relating T_B^{Moon} to phase angle φ that are based on observations over only a narrow range of phase angles at waxing Moon. One cannot identify the phase angle of maximum brightness temperature solely on the basis of the measurements presented in [1, 4]. The model by Yang et al., however, agrees with the values given by Keihm in the range $\varphi = -70^\circ \pm 10^\circ$ and has the advantage of a simple mathematical relationship between brightness temperature and phase angle, which makes it attractive for applications involving the processing of large amounts of data from afternoon satellites. Such applications are, for example, the removal of the contamination of the counts from the DSV by the presence of the Moon or checks of the stability of the photometric calibration [1, 4]. The model by Yang is based on actual measurements with ATMS at phase angles between -75° and -60° relative to the full Moon. Its very good agreement with the results we obtained with MHS at the same phases is proof of the high accuracy of the brightness temperature values achievable by analyzing the Moon intrusions in the DSV of meteorological research satellites. It also demonstrates the relevance of the Moon for cross calibration, because it enables the detection of biases between quite different instruments operating at quite different times, a weighty prerequisite for studies of climate change with satellite data.

The main strength of the observations of the Moon with MHS lies in the determination of the microwave phase lag effect and the corresponding asymmetry between the

brightness temperatures of waxing and waning Moon. This is because its characterization relies on differences between measured fluxes and not their absolute values so that most of the possible systematic errors, related, for example, to properties of the beam, cancel out. The fact that the phase lag found with the window channels of MHS is significantly larger than the one predicted by the models suggests that the thermophysical and electrical properties of the bulk regolith are not identical with the values derived from the returned Apollo samples.

This finding is important, because the Moon has been used as calibration reference by a large number of astronomical microwave projects, where assuming a wrong phase lag causes systematic errors. Interestingly enough a two-week, 5% lunar phase-dependent error appeared in the calibration of COBE (COsmic Background Explorer) at 53 GHz, when the brightness temperature of the Moon was calculated with Keihm's model [17]. The uncertainty of the phase lag can be reduced by analyzing more than the 39 intrusions of the Moon in the DSV that are the basis of the numbers given in Table 2. The Moon appeared altogether 1566 times in the DSV of MHS on NOAA-18 between May 2005 and October 2018, and this number is similar for other satellites. The uncertainty of the maximum brightness temperature of the Moon can be reduced by analyzing data from more satellites: there are five MHSs and three AMSU-Bs in orbit, and averaging their measurements would significantly mitigate the impact of systematic errors.

Taking advantage of the Moon as calibration reference is not limited to the microwave range of the spectrum. The Earth and the Moon are, for example, the only targets observed during the cruise phase of Hayabusa2, which can be used as calibrators for the TIR (Thermal InfraRed imager) [18]. As there are numerous instruments on satellites for Earth observation with mid-infrared channels, an accurate characterization of the lunar radiance in the infrared could be achieved by using a method analogous to the one described in this article for MHS.

Data Availability

The level 1b data from MHS presented in this manuscript are available from NOAA CLASS (Comprehensive Large Array-data Stewardship System).

Conflicts of Interest

The authors declare that they have no conflicts of interest.

Acknowledgments

The authors would like to thank Oliver Lemke for making the satellite data available and Roberto Bonsignori for providing information about MHS on NOAA-18. The characterization of the Moon as flux reference is part of an effort to quantify the uncertainty budget for microwave sounders undertaken within the H2020 project, Fidelity and Uncertainty in Climate data records from Earth Observation (FIDUCEO). FIDUCEO has received funding from the European Union's

Horizon 2020 Programme for Research and Innovation, under grant agreement no. 638822.

References

- [1] T. Mo and S. Kigawa, "A study of lunar contamination and on-orbit performance of the NOAA 18 advanced microwave sounding unit-A," *Journal of Geophysical Research: Atmospheres*, vol. 112, no. D20, 2007.
- [2] V. D. Krotikov and V. S. Troitskiĭ, "Radio Emission and Nature of the Moon," *Soviet Physics Uspekhi*, vol. 6, no. 6, pp. 841-871, 1964.
- [3] M. Burgdorf, S. A. Buehler, T. Lang, S. Michel, and I. Hans, "The Moon as a photometric calibration standard for microwave sensors," *Atmospheric Measurement Techniques*, vol. 9, no. 8, pp. 3467-3475, 2016.
- [4] H. Yang, J. Zhou, F. Weng et al., "Developing vicarious calibration for microwave sounding instruments using lunar radiation," *IEEE Transactions on Geoscience and Remote Sensing*, vol. 56, no. 11, pp. 6723-6733, 2018.
- [5] M. Burgdorf, I. Hans, M. Prange, T. Lang, and S. A. Buehler, "Inter-channel uniformity of a microwave sounder in space," *Atmospheric Measurement Techniques*, vol. 11, no. 7, pp. 4005-4014, 2018.
- [6] R. Bonsignori, "In-orbit verification of microwave humidity sounder spectral channels coregistration using the moon," *Journal of Applied Remote Sensing*, vol. 12, no. 02, 2018.
- [7] M. Burgdorf, T. Lang, and S. Michel, "The Moon as a diagnostic tool for microwave sensors," *GSICS Quarterly*, vol. 10, 2016.
- [8] C. A. Whatling, "Microwave Humidity Sounder Instrument End Item Data Package PFM Model," *Matra Marconi Space*, vol. 3, no. 2, 1999, <https://www.eumetsat.int/website/home/Satellites/CurrentSatellites/Metop/MetopDesign/MHS/index.html>.
- [9] R. Bonsignori, "In-orbit verification of MHS spectral channels co-registration using the moon," in *Proceedings of the SPIE*, vol. 10402, 2017.
- [10] R. J. Coates, "Note: lunar brightness variations with phase at 4.3-MM wave length," *The Astrophysical Journal*, vol. 133, 1961.
- [11] I. Hans, M. Burgdorf, S. Buehler, M. Prange, T. Lang, and V. John, "An uncertainty quantified fundamental climate data record for microwave humidity sounders," *Remote Sensing*, vol. 11, no. 5, 2019.
- [12] H. Yang, F. Weng, and K. Anderson, "Estimation of ATMS antenna emission from cold space observations," *IEEE Transactions on Geoscience and Remote Sensing*, vol. 54, no. 8, pp. 4479-4487, 2016.
- [13] S. J. Keihm, "Interpretation of the lunar microwave brightness temperature spectrum: feasibility of orbital heat flow mapping," *Icarus*, vol. 60, no. 3, pp. 568-589, 1984.
- [14] J. G. Mangum, "Main-beam efficiency measurements of the Caltech Submillimeter Observatory," *Publications of the Astronomical Society of the Pacific*, vol. 105, 1993.
- [15] I. Hans, M. Burgdorf, V. O. John, J. Mittaz, and S. A. Buehler, "Noise performance of microwave humidity sounders over their lifetime," *Atmospheric Measurement Techniques*, vol. 10, no. 12, pp. 4927-4945, 2017.
- [16] I. Moradi, J. Beauchamp, and R. Ferraro, "Radiometric correction of observations from microwave humidity sounders," *Atmospheric Measurement Techniques*, vol. 11, no. 12, pp. 6617-6626, 2018.

- [17] C. L. Bennett, G. F. Smoot, M. Janssen et al., “COBE differential microwave radiometers,” *Astrophysical Journal*, vol. 391, 1992.
- [18] A. Matsuoka, C. T. Russell, S. Tanaka et al., “Earth and moon observations by thermal infrared imager on Hayabusa2 and the application to detectability of asteroid 162173 Ryugu,” *Planetary and Space Science*, vol. 158, 2018.

Research Article

Lunar Radiometric Measurement Based on Observing China Chang'E-3 Lander with VLBI—First Insight

SongTao Han ^{1,2,3}, ZhongKai Zhang,³ Jing Sun,² JianFeng Cao,¹ Lue Chen,¹ Weitao Lu,¹ and WenXiao Li²

¹National Key Laboratory of Science and Technology on Aerospace Flight Dynamics, Beijing Aerospace Control Center, Beijing 100094, China

²National Astronomical Observatories, Chinese Academy of Sciences, Beijing 100012, China

³Institute of Geodesy and Geoinformation, University of Bonn, Nussallee 17, 53115 Bonn, Germany

Correspondence should be addressed to SongTao Han; songtaohanbonn@gmail.com

Received 9 February 2019; Accepted 28 April 2019; Published 2 June 2019

Guest Editor: Jing Li

Copyright © 2019 SongTao Han et al. This is an open access article distributed under the Creative Commons Attribution License, which permits unrestricted use, distribution, and reproduction in any medium, provided the original work is properly cited.

China Chang'E-3 performed soft landing at the plains of Sinus Iridum on lunar surface on December 14th 2013 successfully; it opened a new window for observing lunar surface with radiometric tracking which many lunar scientific researchers always pursue for. Since July 2014, OCEL (Observing Chang'E-3 Lander with VLBI) project has been conducted jointly by IVS (International VLBI Service of Geodesy and Astrometry) and BACC (Beijing Aerospace Control Center), a global IVS R&D network augmented with two China Deep Space Stations configured for OCEL. This paper presents the current status and preliminary result of the OCEL and mainly focuses on determination of the lander position, which is about 7 meter in height and 14 meter in plane of lunar surface with respect to LRO (Lunar Reconnaissance Orbiter). Based on accuracy analysis, further optimized OCEL sessions will make use of this target-of-opportunity, the Chang'E-3 lunar lander, as long as it is working. With higher accurate radiometric observables, more prospective contribution to earth and lunar science is expected by combining with LLR.

1. Introduction

The Moon has always been a prime object of human space exploration, as it holds the distinctions of being the nearest remote celestial object to the earth. Since the first successful spacecraft “lunar 2” reached lunar surface by Soviet Union in 1959, more than 100 missions have been undertaken to research the Moon [2]. In 1969, the Apollo program started a new era for studying the Moon, such as determining parameters of the lunar orbit, physical librations, interior structure, and Earth-Moon dynamics [3]. Since then, LLR (Lunar Laser Ranging) Operation has been conducted to the retroreflector arrays at the Apollo 11, 14, and 15 sites plus the French-built reflector on the Soviet Lunokhod 1 and 2. Two sites, McDonald in USA and Grasse in France, conducted most LLR [4]; especially, Grasse site can even do LLR in day time and in new moon as well as in full moon days. The LLR data collected has significantly contributed to a large scientific domain [5–7].

LRM (Lunar Radiometric Measurement), including Ranging, Doppler tracking and VLBI (Very Long Baseline Interferometry), is another technique conducted in the Moon research. Based on ranging measurement, the LLR data is more sensitive to most of the dynamics, especially the orbital motion of the moon. While earth-based VLBI data has the potential to tie lunar movement to the inertial celestial reference frame [8]. In fact, VLBI measurement to radio beacon on lunar surface existed for less than five years totally in the nearly 50-years-long history of LLR. Though many suggestions and proposals were appealed [9, 10], none came into application until China Chang'E-3 Lander landed on plains of Sinus Iridum of lunar surface on Dec 14th, 2013.

In this paper, we will give an introduction and preliminary analysis of the first LRM with China Chang'E-3 Lander. The paper is organized as follows: Section 2 gives a review of LRM in history; introduction of OCEL (Observing Chang'E-3 Lander with VLBI) project is given in Section 3;

Section 4 discusses the preliminary result of OCEL; based on the analysis and discussion, conclusion and suggestions are given in Section 5.

2. LRM in History

The first earth-based radiometric measurement to lunar lander could be recalled back to nearly 50 years ago, the Apollo era [16]. NASA (National Aeronautics and Space Administration) designed and launched the Apollo program to land humans on the Moon and bring them safely back to the earth [17]. With five of the successful Apollo missions, ALSEP (Apollo Lunar Surface Experiments Package) was carried out, which was designed to continuously monitor the environment of each Apollo landing site for a period of at least a year after the astronauts had departed [18]. Within a set of scientific instruments, two research groups conducted scientific experiment with radiometric transmitters of the Apollo landers.

2.1. ALSEP Double-Differential VLBI Program. MIT (Massachusetts Institute of Technology) research group observed ALSEP S-band radio transmitters by VLBI to improve determination of the positions of the ALSEPs and the parameters governing the motion of the Moon about its center of mass [19]. In the ALSEP Double-Differential VLBI program, a new device, DDR (Differential Doppler Receiver), was installed in six stations of NASA STDN (Spaceflight Tracking and Data Network) to support the project [20].

Tracking stations observed at least two of the five ALSEPs in each scan (Figure 1). Double differential observable is sensitive to the relative position of the two ALSEP transmitters, while is insensitive to other error sources, such as earth troposphere's effect on radio signal [21]. The program was formally conducted from March, 1973, and the first scientific result was based on observations conducted in about 130 days evenly distributed during the 16-month period. Based on ALSEP Double-Differential VLBI program, the uncertainties of the relative coordinates of ALSEP transmitter are 30m in the radial direction and 10m in the transverse plane, and values of lunar libration parameters have smaller uncertainty than the solution with only LLR data [22].

2.2. ALSEP-Quasar VLBI Program. The program ALSEP-Quasar VLBI was carried out by JPL (Jet Propulsion Laboratory) to accurately tie the lunar orbit to the new inertial quasar reference frame [23]. The program employed a "4-antenna" technique [24], a large antenna at each end of baseline observed the reference quasar, while smaller antenna which was attached to the large dish observed ALSEP (Figure 2). The advantage of 4-antenna technique is that the differential interferometric phase of each source without ambiguity for the length of the experiment is obtained; then, the differential phase could be used to derive angular separation between the reference quasar and the ALSEP transmitters on lunar surface. The precision is comparable to LLR, but is more sensitive in right ascension and declination instead of range [25].

Slade [26, 27] conducted covariance analysis for combining LLR data and 19 Δ VLBI experiments over 37 months; the 19 Δ VLBI experiments constrained the parameters twice as much as the 1600 laser range determinations over the same time span. However, the ALSEP were terminated since September 30th, 1977 [28]; then, no further reports about LRM with ALSEP were published to public.

3. OCEL Project

3.1. China Chang'E-3. China Chang'E-3 (Figure 3) soft landing on lunar surface is a key stone in CLEP (China Lunar Exploration Program), which stands for perfect finish of the phase II of CLEP [14, 29]. The X-band transmitter deployed on the lander opened up a new window for observing lunar surface with radiometric measurement from the earth.

Compared with LRM in Apollo era, precision of LLR has increased from orders of decimeters to less than 2 cm [3, 30]. Errors in the coordinates of the lunar beacons of ALSEPs 14 and 15 on the other hand are closer to 1m, and ALSEPs 12, 16, and 17 may have errors as large as 30m [31]. Moreover, during the past few years, lunar ephemeris has been improved by nearly three orders, and a several-orders-of-magnitude improvement of the variations in the Moon's rotation has been made [32]. It seems a big challenge to contemporary LRM for benefiting the Moon scientific research.

Nevertheless, the Chang'E-3 lander as an ideal radiometric beacon on lunar surface is a chance many lunar scientific researchers always pursue for. If the lander tracked accurately from the earth, landed spacecraft can be positioned with enough accuracy and would be useful for lunar geodesy [33]. Initially, observing X-band Chang'E-3 lander transmitter with VLBI could tie the lunar orbit to ICRF accurately [34]. An interesting fact about ALSEP is that, the original proposal, though not adopted, about applying VLBI to study the Moon by MIT is to deploy an X-band wideband (50MHz) noise source as the beacon, and the scientific objectives include determining the motion of the moon's center of mass against extragalactic radio sources [35]. Furthermore, the lunar librations are currently mainly calculated with LLR data, e.g., LLR data from 1970 to 2007 were used for the computation of the JPL DE421 and librations after 2007 are obtained by extrapolations [36]. As VLBI is more sensitive to the transverse plane, it could benefit correction to the three Euler angles which describe the lunar librations in principle, especially the angle between the direction of the Moon center to the Equinox and the intersection line of the Moon equator and the Earth equator [37, 38]. Additionally, with more accurate observable and enough tracking arc through experiment schedule, LRM data could be combined with LLR data in many aspects on earth and lunar science, including lunar ephemeris, lunar physics, and the Moon's interior [39].

3.2. Observing Chang'E-3 Lander with IVS Stations. The concept of OCEL (Observing the Chang'E-3 Lander with VLBI) was firstly introduced in the 8th IVS (International VLBI Service of Geodesy and Astrometry) General Meeting in 2014. Following observing proposal which was jointly

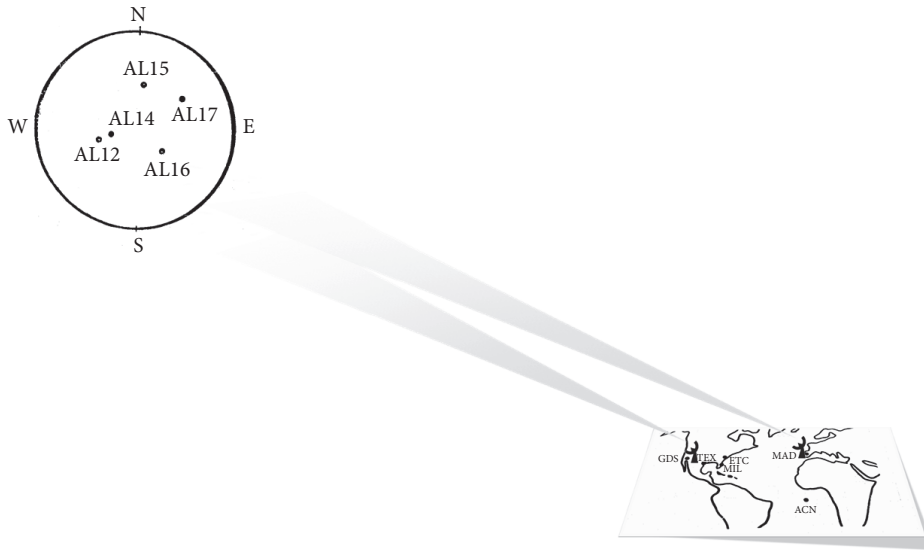


FIGURE 1: ALSEP Double-Differential VLBI program by MIT.

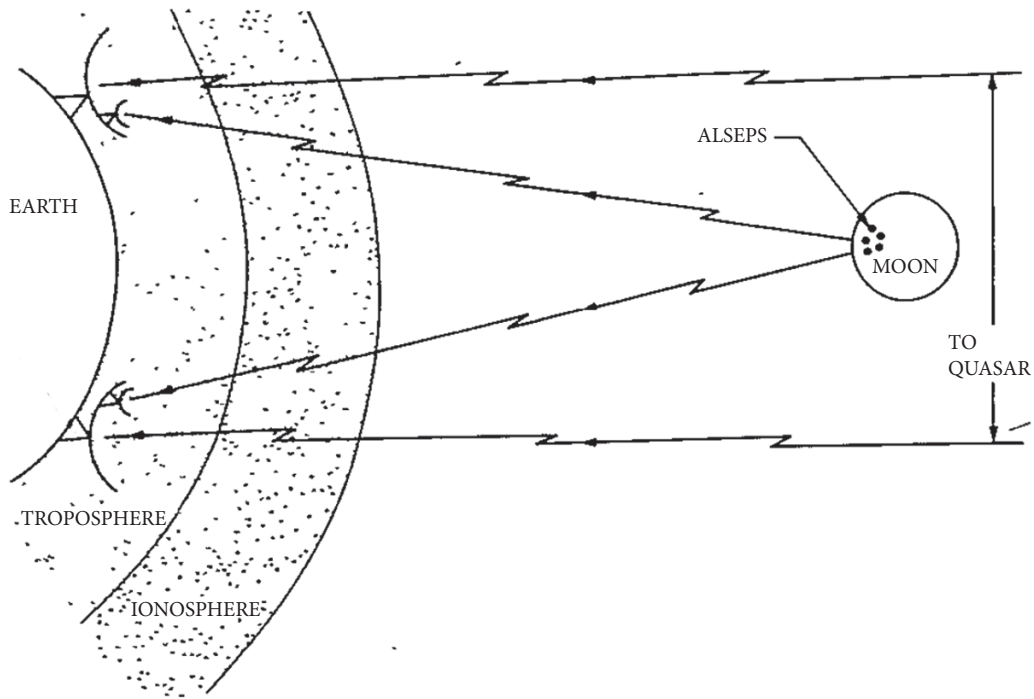


FIGURE 2: ALSEP-Quasar VLBI program by JPL [1].

drafted by BACC (Beijing Aerospace Control Center) and IVS Bonn Correlator Center to the OPC (Observing Program Committee) of IVS, OCEL was conducted by a global IVS R&D network (involving networks with 7 to 12 worldwide distributed IVS stations) (Figure 4) augmented with two China Deep Space Stations since 2014. The three LRM projects in history are compared in Table 1.

In the first 3-years observation (called phase I) of OCEL, Sweden Onsala Observatory is responsible for the schedule file where Δ DOR [40] mode is adopted, and the antennas

track the lander and compact extragalactic reference quasar alternatively. In order to minimize the effect on other regular geodetic observation, OCEL observation is scheduled within IVS R&D session. The general scheduling strategy adopts alternating observing blocks of primarily 30 minutes length, where the observations are scheduled either geodetic observation or OCEL of each half an hour [41]. As strategies of frequency set-up, we schedule reference quasar and system attenuation changed across different sessions to find optimal OCEL observing system characteristic. The first phase of

TABLE 1: Comparison of different LRM.

	Agency	Tracking stations	Target	Frequency Band	Observable	Period & Span
ALSEP Double-Differential VLBI	MIT	STDN (Spacecraft Tracking and Data Network) 6 stations	ALSEP 12/14/15/16/17	S	phase (delay)	Mar 1973~Jul 1974 more than 130 days
ALSEP-Quasar VLBI	JPL	DSN (Deep Space Network) 3 stations Plus 'Apollo' station of STDN subsets of the IVS observing network	ALSEP 12/14/15/16/17	S	Phase (delay)	Sep 1974~Sep 1977 19 Δ VLBI
OCEL (phase I)	IVS & BACC	totally 15 stations participate	Chang'E-3 Lander	X	group delay	Jun 2014~Dec 2016 12 sessions

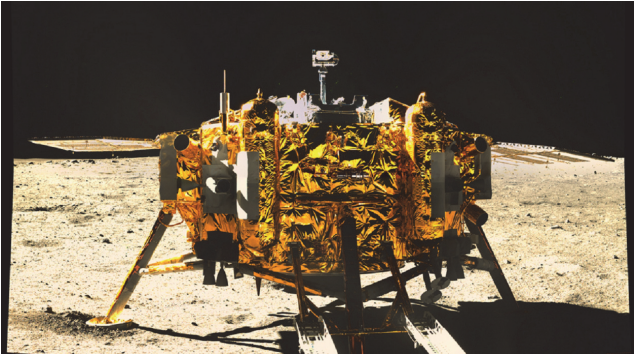


FIGURE 3: Picture of Chang'E-3 lander by Yutu Rover.



FIGURE 4: Distribution of IVS stations participating in OCEL.

OCEL finished at the end of 2016 and totally 12 observing sessions has been conducted successfully (Table 2). Taking session rd1601 (OCEL09) as an example, Figure 5 shows the quasar used for calibration and sky plot of station Onsala for the schedule file.

4. Preliminary Results and Discussion

4.1. Processing Strategy. BSCS (BACC Software Correlator System) is adopted for data correlation and fringe fitting

in BACC [42]. IVS Bonn Correlator Center deploys DiFX [43] and CALCII for computing a priori model of near field target. The standard fringe fitting program used in connection with geodetic correlators is the HOPS (Haystack Observatory Processing Software) component “fourfit” [44], and a refreshed version “fourfit-DOR” is developed which extends the fringe fitting algorithm of “fourfit” to allow for processing of DiFX correlation output of DOR tones [45].

Δ DOR theorem and application are widely discussed [15, 46]; in OCEL, geodetic observations with different systematic frequency altered each half an hour, and the change in channel parameter caused delay offsets. So each block with continuous scans (usually half an hour) within a session is calibrated separately, and meteorological data recorded in tracking stations is used to improve the accuracy of a priori atmospheric delay. After calibration with reference quasar, observable of the lander is used for analysis.

4.2. Position Determination. Position determination of the radiometric beacon is the foundation of scientific analysis. The theoretical basis of estimating parameters with the observables by weighted least-square fitting is widely discussed and adopted [47], and the state matrix of partial derivatives with elements of VLBI is analyzed in detail [11, 48].

As VLBI observable is less sensitive to radial direction (similar to X-axis), two strategies are induced to make the results more stable and reliable. One approximate method is that, as the area of the landing site with reliable height information is deemed as flat, then a self-constrain strategy is induced [36].

$$\sqrt{X^2 + Y^2 + Z^2} = \sqrt{X_0^2 + Y_0^2 + Z_0^2} \quad (1)$$

where X, Y, Z are the 3-dimensional coordinates of the lander and X_0, Y_0, Z_0 are the default coordinate values from LRO (Lunar Reconnaissance Orbiter). The other more reliable method is that UXB (Unified X-Band) observables are combined. In our analysis, one-hour arc of two-way ranging observable from KASHI Deep Space station is combined with observables in OCEL to make position determination. The reason is that ranging tracking is conducted continuously just before Chang'E-3 soft landing, during EDL (Entry Decent Landing) and the first one hour after landing on lunar surface, so the ranging systematic error is stable during the whole tracking arcs. The accuracy of orbit determination for

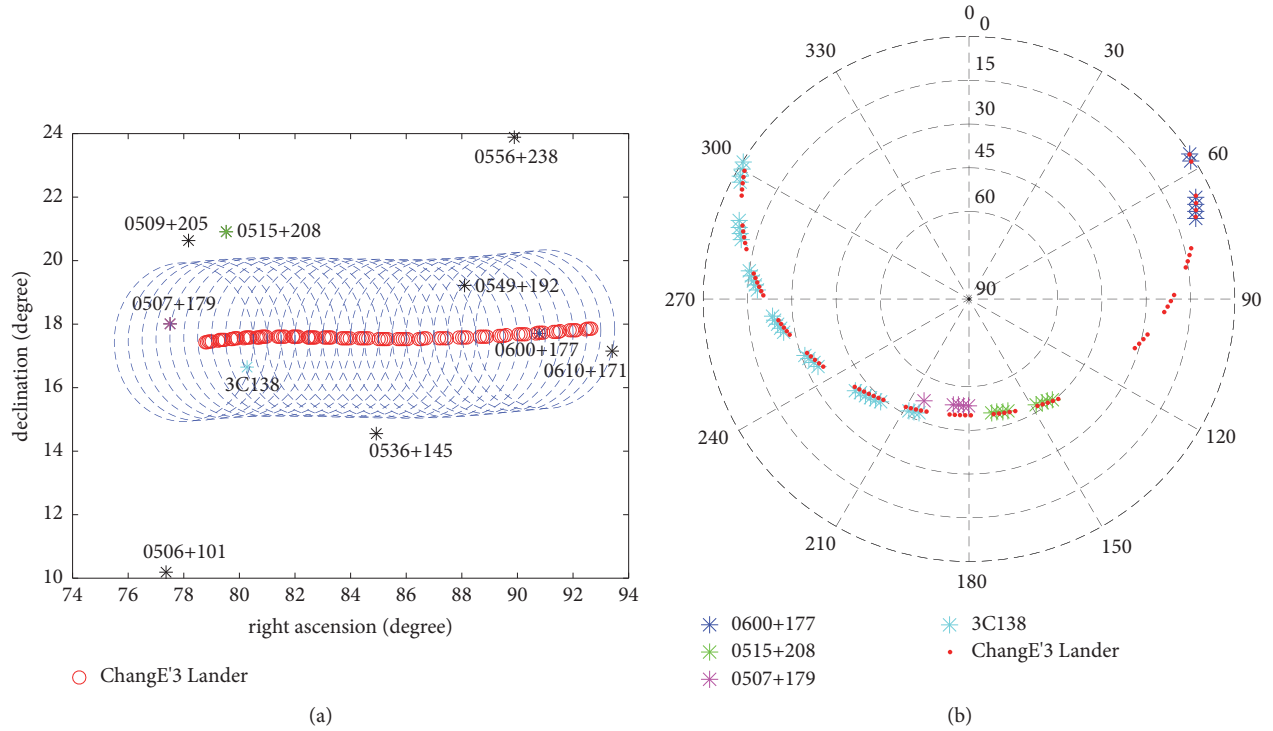


FIGURE 5: ChangE'3 lander position and sky plot of Onsala within session rd1601.

TABLE 3: Correction of coordinates.

Observable type	$\Delta X(m)$	$\Delta Y(m)$	$\Delta Z(m)$
VLBI	-501.954	-44.021	-32.299
VLBI+self-constrain	15.448	-3.231	-16.115
VLBI+Ranging	13.837	-2.483	-4.007

TABLE 4: Coordinates comparison.

	Latitude($^{\circ}$)	Longitude($^{\circ}$)	H(m)
LRO	44.1214	340.4884	-2640
[11]	44.1188	340.4874	--
[12]	44.1219	340.4887	--
[13]	44.1213	340.4885	--
[14]	44.1206	340.4876	-2632
[15]	44.1189	340.4907	-2637.6
this paper	44.1210	340.4882	-2632.8

circular orbit is better than 20 meters, and the accuracy in radial is in the order of meter (better than 5 meters) [48], which could restrain ranging accuracy better than 5 meters with systematic error removed. Besides, positioning result of GSFC (Goddard Space Flight Center) by LRO is deemed as a default value [12]. Table 3 shows the correction of the lander coordinates in Principle Axis with different resolution strategy.

The result is compared with other published results, as listed in Table 4. Consistence of positioning results by remote image matching is affected by the basic reference image

adopted, and it could be identified that literature [13] is a little different from LRO/[49]/[50], as the reference image is acquired by Chang'E-2.

Figure 6 shows the positioning results with maximum ranging systematic error (5m) existed. The height varies about 3.46m caused by ranging systematic error, while tangent plane on lunar surface is about 3.04m (Figure 6). The difference of positioning results from LRO is about 7.2 meters in height and about 14 meters in plane on lunar surface.

4.3. Data Process Analysis. Accuracy analysis of ΔDOR is shown in literatures [51]. In phase I of OCEL, there is the first observation for most IVS radio telescopes which are set up almost exclusively for observations of faint signals of natural radio sources, so adjustments of channel frequency and bandwidth parameter setting up are sometimes being carried on during the whole OCEL phase I. Based on our analysis, main sources which deteriorate the accuracy may be grouped into three general categories in OCEL.

The contrast in signal strength between reference quasar and the lunar lander might be challenging for the receiving system. Though the higher power signal of lander does not saturate the VLBI-systems which adjust attenuation with automatic gain control or with an experienced value, phase offset may exist in an alternating scan mode for some stations (Figure 7).

The phase offset will deteriorate group delay accuracy if not compensated properly, so stations without PCAL (phase calibration instrument) and sessions within which PCAL is not active are not reliable for observable analysis.

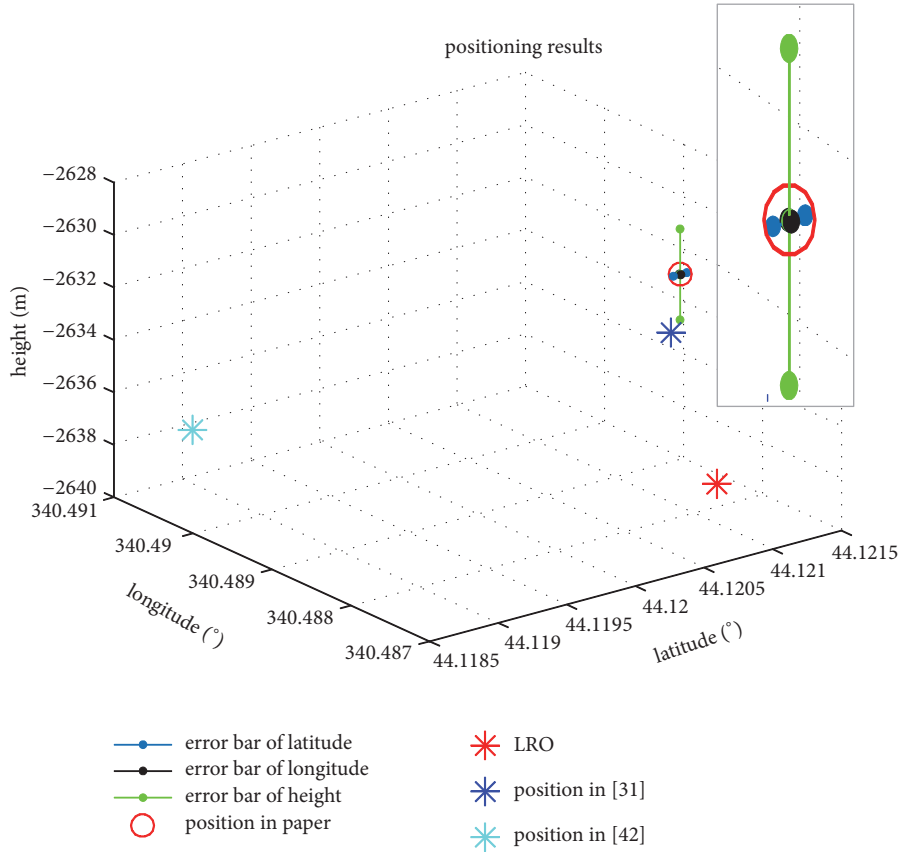


FIGURE 6: Comparison of positioning results with respect to ranging systematic error.

In OCEL, geodetic observations were carried out within each session with half-an-hour interval. Geodetic observation of the first ten sessions was carried out with a frequency set-up used in routine IVS-sessions, which was different from lunar observation. The change in channel frequency set-up caused delay offsets in some baselines (Figure 8).

The systematic offset limits the length of tracking arc of reference quasar used for parameter estimation, such as clock offset, clock drift, and residual tropospheric delay, including dry and wet component. In the case of reference quasar with lower SNR within half-an-hour short arc, the reliability of parameters estimated from reference quasar becomes lower, which will deteriorate the accuracy of the lander observable at last.

Besides, the SNR of reference quasar could also affect the accuracy of lander observable through residual systematic delay calibration. In OCEL, spanned bandwidth is less than 40MHz, compared with 720MHz in X-band of IVS general sessions; a conservative angular sensitivity would be worse by nearly 20 times. Higher SNR will benefit accuracy of reference quasar and also will improve lunar lander observables through Δ DOR. Statistics show that the random error of observable is about 1ns in OCEL. Figure 9 shows X-band SNR of reference quasar of all baselines in OCEL09, calculated using the following equation:

$$\delta_{\tau} = \frac{1}{2\pi \cdot \sqrt{(1/N) \sum_{i=1}^N (f_i - f_{ave})^2} \cdot SNR} \quad (2)$$

where f_i is the frequency of channel used for bandwidth synthesis and f_{ave} is the average frequency.

Based on the experiment accuracy analysis, in order to enhance the contribution to Earth-Moon scientific topics where position accuracy better than 1 meter is needed [39], both the processing strategy and observing mode would be optimized. One of a prospective program is being researched. In this case, sites with two geodetic antennas or more will participate in the observation, such as Wettzell, Hartrao, and Hobart, and one antenna observes the lander while the other antenna observes a small angular-separated quasar with stronger flux. Firstly, the phase-delay observable is expected, which would improve the delay observable by two orders. Secondly, phase fluctuation caused by frequency standard could be eliminated if the two antennas share common maser. Thirdly, while the lander and the reference quasar with smaller separated angle are observed at the same time, time-varied error could be calibrated as much as possible. Last but not least, longer arc will be adopted in schedule which will benefit the systematic parameter calibration.

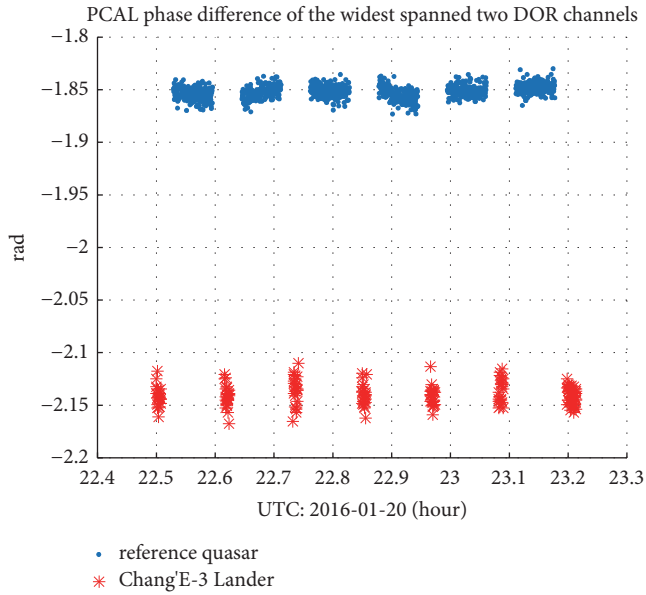


FIGURE 7: Phase offset between the altering scans of station NYALES20 in OCEL09. (In this case, the integration time is 1s, phase offset between reference quasar and lunar lander is as large as 16.5° , which equals 1.2ns offset in the group delay observable.)

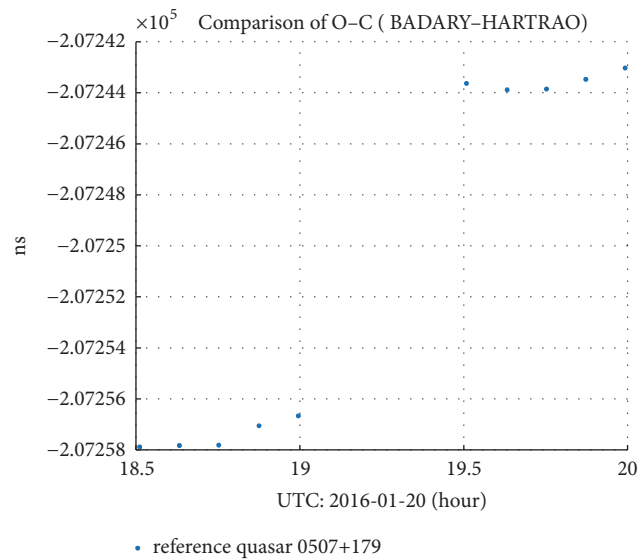


FIGURE 8: Delay offset caused by system channel setting up variation. (In this case, from 19:00~19:30 geodetic observation with different frequency set-up is conducted, when system parameters change back to OCEL observation, delay offset could be identified, most of O-C belongs to station clock.)

5. Conclusions

Observing lunar surface with radiometric tracking is always a pursuit in the field of Earth-Moon scientific since Apollo era. The successful Chang'E-3 soft landing makes it come true after nearly 50 years. The first phase of OCEL has been successfully conducted jointly by IVS and BACC. Performance and ability of IVS geodetic tracking stations are evaluated,

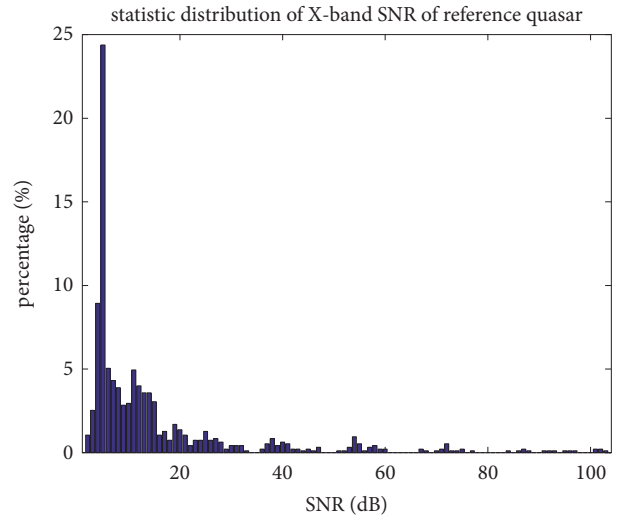


FIGURE 9: X-band SNR of reference quasar of all baselines in OCEL09. (In this case, 4 channels corresponding to DOR tones channel are used for bandwidth synthesis. Though designed SNR value is 35dB, SNR from 7dB to 15dB takes up nearly 40%, and most of lower SNR observables come from baselines combined with station FORTLEZA.)

correlation and data reduction algorithm are also refreshed for artificial satellite signals, and preliminary positioning result which could be consistent in the magnitude of 15 meters is analyzed and discussed. With optimized observing mode and processing strategy, further OCEL sessions will be conducted to make use of this target-of-opportunity as long as Chang'E-3 is working, which is expected to make progress on earth and lunar science.

Data Availability

Raw OCEL data could be available under the approval of the project organizer.

Conflicts of Interest

The authors declare that they have no conflicts of interest.

Acknowledgments

This work was supported by the National Natural Science Foundation of China (Grant No. 61401014), German Research Foundation (satellite observations with radio telescopes for linking reference systems), and China Scholarship Council Fellowship (201503170203). The authors would like to thank all of the contributors in OCEL, especially colleagues in IVS tracking stations.

References

- [1] M. A. Slade, R. A. Preston, A. W. Harris et al., "ALSEP-Quasar differential VLBI," *The Deep Space Network Progress Report 42-33*, pp. 37–54, 1976.

- [2] "Exploration of the Moon," https://en.wikipedia.org/wiki/Exploration_of_the_Moon.
- [3] C. Munghemzulu, L. Combrinck, and J. O. Botai, "A review of the lunar laser ranging technique and contribution of timing systems," *South African Journal of Science*, vol. 112, no. 3-4, pp. 1-9, 2016.
- [4] "Lunar laser ranging observations from 1969 to 30 december 2015," <http://polac.obspm.fr/lldatae.html>.
- [5] J. Chapront and G. Francou, "Lunar laser ranging: measurements, analysis, and contribution to the reference systems," *IERS Technical Note*, vol. 34, pp. 97-116, 2006.
- [6] J. Müller and L. Biskupek, "Variations of the gravitational constant from lunar laser ranging data," *Classical and Quantum Gravity*, vol. 24, no. 17, pp. 4533-4538, 2007.
- [7] T. Murphy, E. Adelberger, J. Battat et al., "APOLLO performance and data quality," in *Proceedings of the 19th International Workshop on Laser Ranging*, pp. 27-31, 2014.
- [8] G. S. Tang, J. F. Cao, S. T. Han et al., "Contributions of chang'E-3 radio beacon to selendesy," in *Proceedings of the 25th International Symposium on Space Flight Dynamics*, 2015.
- [9] P. L. Bender, J. E. Faller, J. L. Hall et al., "Microwave and optical lunar transponders," in *Proceedings of the Astrophysics from the Moon*, vol. 207, pp. 647-655, Annapolis, Maryland (USA).
- [10] J. O. Dickey, P. L. Bender, J. E. Faller et al., "Lunar laser ranging: a continuing legacy of the Apollo program," *Science*, vol. 265, no. 5171, pp. 482-490, 1994.
- [11] Y. Huang, S. Chang, P. Li et al., "Orbit determination of Chang'E-3 and positioning of the lander and the rover," *Chinese Science Bulletin*, vol. 59, no. 29-30, pp. 3858-3867, 2014.
- [12] <https://www.nasa.gov/content/nasa-images-of-change-3-landing-site/>.
- [13] Y. Jiang, S. C. Liu, M. L. Li et al., "ChangE-3 system pinpoint landing localization based on descent image sequence," *Chinese Science Bulletin*, vol. 59, pp. 1838-1843, 2014.
- [14] P. LI, Y. Huang, S. Chang et al., "Positioning for the Chang'E-3 lander and rover using Earth-based observations," *Chinese Science Bulletin (Chinese Version)*, vol. 59, no. 32, pp. 3162-3173, 2014.
- [15] Q. H. Liu, Q. B. He, X. Zheng et al., "Analysis of VLBI observation for Tianma radio telescope in Chang'E-3 orbit determination," *Scientia Sinica Physica, Mechanica & Astronomica*, vol. 45, no. 3, Article ID 039501, 2015.
- [16] M. A. Slade, P. F. MacDoran, and J. B. Thomas, "Very long baseline interferometry (VLBI) possibilities for lunar study," *JPL Technical Report 32-1526*, vol. XII, pp. 35-39, 1973.
- [17] W. D. Compton, *Where No Man Has Gone Before: A History of Apollo Lunar Exploration Missions*, The NASA historical series, 1988.
- [18] H. Lindsay, "ALSEP, Apollo-lunar surface experiments package, 19 November 1969 - 30 September 1977," *Apollo Lunar Surface Journal*, 2010, <https://www.hq.nasa.gov/alsj/HamishALSEP.html>.
- [19] C. C. Counselman, "VLBI observations of ALSEP transmitters, Technical Report," Tech. Rep., Massachusetts Institute of Technology, USA, 1977.
- [20] C. C. Counselman, H. F. Hinteregger, R. W. King et al., "Lunar baseline and libration from differential VLBI observations of ALSEPS," *The Moon*, vol. 8, pp. 484-489, 1973.
- [21] R. W. King, C. C. Counselman, and I. I. Shapiro, "Lunar dynamics and selenodesy: Results from analysis of VLBI and laser data," *Journal of Geophysical Research: Atmospheres*, vol. 81, no. 35, pp. 6251-6256, 1976.
- [22] R. W. King, *Precision selenodesy via differential very-long-baseline interferometry [Ph.D. thesis]*, Massachusetts Institute of Technology, 1975.
- [23] M. A. Slade, W. S. Sinclair, A. W. Harris, R. A. Preston, and J. G. Williams, "Alsep-quasar VLBI: complementary observable for laser ranging," in *Scientific Applications of Lunar Laser Ranging*, vol. 62, pp. 287-287, 1976.
- [24] M. A. Slade, R. A. Preston, A. W. Harris et al., "ALSEP-Quasar differential VLBI," in *Lunar Science VII*, vol. 821, 1976.
- [25] M. A. Slade, A. W. Harris, and R. A. Preston, "ALSEP-Quasar VLBI: development of an accurate astrometric technique," in *Bulletin of the American Astronomical Society*, vol. 8, p. 540, 1976.
- [26] M. A. Slade, R. A. Preston, A. W. Harris et al., "ALSEP-Quasar VLBI observations," in *Proceedings of the Lunar and Planetary Science Conference*, vol. 8, pp. 877-878, 1977.
- [27] M. A. Slade, R. A. Preston, A. W. Harris, L. J. Skjerve, and D. J. Spitzmesser, "ALSEP-quasar differential VLBI," *The Moon*, vol. 17, no. 2, pp. 133-147, 1977.
- [28] J. R. Bates, W. W. Lauderdale, and H. Kernaghan, "ALSEP termination report," *NASA Reference Publication*, vol. 1036, 1979.
- [29] Z. Z. Sun, Y. Jia, and H. Zhang, "Technological advancements and promotion roles of chang'E-3 lunar probe mission," *Science China Technological Sciences*, vol. 56, no. 11, pp. 2702-2708, 2013.
- [30] T. W. Murphy, "Lunar laser ranging: the millimeter challenge," *Reports on Progress in Physics*, vol. 76, no. 7, p. 076901, 2013.
- [31] M. E. Davies and T. R. Colvin, "Lunar coordinates in the regions of the Apollo landers," *Journal of Geophysical Research: Planets*, vol. 105, no. E8, pp. 20277-20280, 2000.
- [32] J. O. Dickey, P. L. Bender, J. E. Faller et al., *Invited Review Article submitted to Science*, 1994.
- [33] J. G. Williams, S. G. Turyshev, D. H. Boggs et al., "Lunar laser ranging science: gravitational physics and lunar interior and geodesy," in *Proceedings of the 35th COSPAR Scientific Assembly*, 2006.
- [34] G. S. Tang, J. F. Cao, S. T. Han et al., "Research on lunar radio measurement on chang'E-3," *Journal of Deep Space Exploration*, vol. 1, no. 3, pp. 236-240, 2014.
- [35] L. J. Kosofsky and C. C. Counselman, "Precision selenodesy and lunar libration through VLBI Observations of ALSEPS," Technical Report, 1975.
- [36] E. H. Wei, Z. Q. Li, C. J. Dong et al., "On the improvement of chang'E-3 lander position determination and lunar librations estimation with VLBI observations," *Bulletin of Surveying and Mapping*, vol. 8, pp. 1-5, 2016.
- [37] J. Yan, J. Ping, F. Li et al., "Chang'E-1 precision orbit determination and lunar gravity field solution," *Advances in Space Research*, vol. 46, no. 1, pp. 50-57, 2010.
- [38] J. G. Yan, S. Goossens, K. Matsumoto et al., "CEGM02: an improved lunar gravity model using Chang'E-1 orbital tracking data," *Planetary and Space Science*, vol. 62, no. 1, pp. 1-9, 2012.
- [39] G. S. Tang, J. F. Cao, S. T. Han et al., "Research on lunar radio measurements by chang'E-3," in *Proceedings of the 8th IVS General Meeting Proceedings*, pp. 473-477, 2014.
- [40] N. James, R. Abello, M. Lanucara, M. Mercolino, and R. Maddè, "Implementation of an ESA delta-DOR capability," *Acta Astronautica*, vol. 64, no. 11-12, pp. 1041-1049, 2009.

- [41] R. Hass, G. S. Tang, A. Nothnagel et al., "OCEL-observations of the changE lander with VLBI," in *Proceedings of the First International Workshop on VLBI Observations of Near-Field Targets*, 2016.
- [42] S. T. Han, G. S. Tang, L. Chen et al., "VLBI software correlator at the interferometric tracking center of the china deep space network," in *Proceedings of the 8th IVS General Meeting Proceedings*, pp. 482–484, 2014.
- [43] W. F. Brisken, "Near-field correlation with the DiFX correlator," in *Proceedings of the First International Workshop on VLBI Observations of Near-field Targets*, 2016.
- [44] A. Bertarini, *DiFX Correlation and Post-Correlation Analysis*, IVS VLBI School, 2013.
- [45] S. Han, A. Nothnagel, Z. Zhang, R. Haas, and Q. Zhang, "Fringe fitting and group delay determination for geodetic VLBI observations of DOR tones," *Advances in Space Research*, vol. 63, no. 5, pp. 1754–1767, 2019.
- [46] W. R. Wu, G. L. Wang, D. G. Jie et al., "High-accuracy VLBI technique using Δ DOR signals," *Science China: Information*, vol. 43, no. 2, pp. 185–196, 2013.
- [47] D. W. Marquardt, "An algorithm for least-squares estimation of nonlinear parameters," *Journal of the society for Industrial and Applied Mathematics*, vol. 11, no. 2, pp. 431–441, 1963.
- [48] J. F. Cao, Y. Zhnag, S. J. Hu et al., "An analysis of precise positioning and accuracy of the ce'3 lunar lander soft landing," *Geomatics and Information Science of Wuhan University*, vol. 41, no. 2, pp. 274–278, 2016.
- [49] B. Liu, K. C. Di, B. F. Wang et al., "Positioning and precision validation of Chang'E-3 Lander based on multiple LRO NAC images," *Chinese Science Bulletin*, vol. 60, no. 28-29, pp. 2750–2757, 2015.
- [50] R. V. Wagner, M. S. Robinson, E. J. Speyerer et al., "Locations of anthropogenic sites on the moon," in *Proceedings of the 45th Lunar and Planetary Science Conference*, 2014.
- [51] G. S. Tang, *Radiometric Measurement Technique for Deep Space Navigation*, National Defense Industry Press, China, Beijing, 2012.

Research Article

Study of Chang'E-2 Microwave Radiometer Data in the Lunar Polar Region

Fan Yang , Yi Xu , Kwing Lam Chan, Xiaoping Zhang, Guoping Hu, and Yong Li

State Key Laboratory of Lunar and Planetary Sciences, Macau University of Science and Technology, Macau 999078, China

Correspondence should be addressed to Yi Xu; yixu@must.edu.mo

Received 5 February 2019; Accepted 7 April 2019; Published 24 April 2019

Guest Editor: Jing Li

Copyright © 2019 Fan Yang et al. This is an open access article distributed under the Creative Commons Attribution License, which permits unrestricted use, distribution, and reproduction in any medium, provided the original work is properly cited.

The Chang'E-2 (CE-2) four-channel microwave radiometer (MRM) data with frequencies of 3 GHz, 7.8 GHz, 19.35 GHz, and 37 GHz have been used to investigate the properties of lunar surface such as regolith thickness, dielectric constant, and titanium abundance within a depth of several meters in middle and low latitudes. The purpose of this work is to take a close look at MRM data in the polar regions of the Moon and analyze the characteristics of the brightness temperature (TB) in permanently shadowed regions (PSRs), especially where evidence of water ice has been found. First, the comparisons of brightness temperature values in the polar region and in low latitudes show that (1) the periodic diurnal (day/night) variation of TB becomes weak in high latitudes since topography plays a dominant role in determining TB in polar region and (2) seasonal effects are more recognizable in polar region than in low latitudes due to the weak illumination condition. Second, even without direct sun illumination, significant seasonal variations of TBs are observed in PSRs, probably caused by the scattering flux from neighboring topography. TB Ratio (TBR) between channel 1 and channel 4, which indicates the differences of TB at different depths of lunar regolith, is higher and shows stronger seasonal variation in PSR than regions with direct illumination. Third, overall the distribution of high TBR values is in consistency with the water ice distributions obtained by the Moon Mineralogy Mapper instrument, the LAMP UV spectra, and the Lunar Prospector Neutron Spectrometer. The proportion of the summation over area with water ice proof in the regions of interest is 0.89 and 0.56 in south pole and north pole, respectively. The causes of the correlation of high TBR between different microwave frequencies and stability of water ice deposits still require further investigation, but MRM data shows unique characteristic in PSRs and could provide important information about the upper few meters of lunar regolith.

1. Introduction

Since Selene, Chang'E, Chandrayaan-1, and Lunar Reconnaissance Orbiter have fulfilled their missions successfully, more and more questions about the Moon appear. Whether the water ice exists in the lunar polar region is an essential one among these problems since it has both important scientific significance and potential application value as an important resource for human beings in the future lunar explorations.

Watson et al. firstly put forward the idea of the possible existence of the water ice in the permanently shadowed regions (PSRs) on the Moon because of the small obliquity and the large variation in topographic relief near the poles [1]. However, Stacy et al. and Campbell et al. did not find any evidence of water ice deposits in the lunar southern polar

region, using the ground-based radar system to image the polar region [2, 3]. Nozette et al. found the presence of water ice after analyzing the Clementine bistatic radar data [4], but a reanalysis showed that radar data were not well-documented to demonstrate the existence of the water ice [5]. With the Miniature Radio Frequency (Mini-RF) radar data, Spudis discovered a different class of polar crater that exhibits high circular polarization ratio (CPR) which may associate with the presence of water ice [6]. However, Fa et al. found that the enhanced CPR is probably caused by rocks rather than ice deposits [7].

Analysis result from the Lunar Prospector (LP) neutron spectrometer indicated abundant hydrogen, which cannot be identified as water ice or other hydrogenated compounds, existing in PSRs [8, 9]. In 2009, water was detected after

the spacecraft of the Lunar Crater Observation and Sensing Satellite (LCROSS) impacted the Cabeus crater [10]. In addition, Hayne et al. had shown the location of the anomalous ultraviolet (UV) albedo consistent with water ice in the southern polar region, based on the Lyman Alpha Mapping Project (LAMP) UV spectra [11]. Recently, Li found the direct evidence of the surface exposed water ice in the lunar polar region with the Moon Mineralogy Mapper (M^3) instrument on the Chandrayaan-1 spacecraft [12].

Compared to infrared radiation, microwave signals originate from deeper layers and can reveal the physical properties of lunar regolith [13]. The microwave observation of the Moon started in 1946 [14, 15]. Then in Apollo era, a series of microwave ground-based observations of the Moon was made to obtain the physical parameters of the lunar surface by simulating the brightness temperature (TB) with theoretical models [16–22].

Lunar orbiters Chang'E-1 (CE-1) and Chang'E-2 (CE-2) were launched in 2007 and 2010, respectively. Both carried Microwave radiometer (MRM), which conducted passive microwave remote sensing measurements to obtain the TB of the lunar surface at 3, 7.8, 19.35, and 37 GHz (10, 3.84, 1.55, and 0.81 cm wavelengths) [23]. The first microwave map of the complete Moon was made by the CE-1 MRM data [24]. In polar region, CE-1 TB map shows some cold patches, where local temperature minima are independent of day and night due to absence of direct illumination in PSRs [13]. MRM data have also been utilized in inferring the properties of the upper few meters of lunar surface in low and middle latitudes; e.g., the thickness distribution of regolith was retrieved using the MRM data [25], the effective complex dielectric constant of lunar regolith as a function of the depth at different frequency channels [26], lunar ($\text{FeO} + \text{TiO}_2$) abundance [27], rock abundance, and others [28]. Also, people had studied basaltic volcanism of the Moon with MRM data [29].

The purpose of this work is to take a close look at MRM data in the polar regions of the Moon and analyze the characteristics of the TB in permanently shadowed regions, especially where plausible evidence of water ice has been found.

2. Chang'E TB Data

CE-2 observation covered the entire Moon by seven times and the local time coverage of the CE-2 data was over a complete lunation [30]. The total effective time of MRM data is 279818 min for 2401 tracks. The spatial resolutions of CE-2 MRM are 25 km and 17.5 km for 3 GHz and three remaining channels, respectively [31]. The absolute temperature accuracy is less than 0.5 K over the temperature range 100–350 K [30].

Note that MRM data have almost constant negative biases from theoretical results probably due to the heat contamination of cold reference antenna, but the variation trend of TB is still available [32, 33]. The microwave TB range is set as 30K–400K TB and points outside this range are considered as anomalous and excluded from this study [30]. Also, about $\sim 0.92\%$ of the total tracks were removed due to

visible errors. Approximately 8,506,115 measurement points were selected in this work.

3. Data Comparisons and Analysis

3.1. TB in Low Latitude and High Latitude. The TB differences are more significant between channel 1 and channel 4 comparing with the other two channels. In addition, TB data of channel 2 contains a certain deviation from previous studies [32]. Therefore, we extract the TB data of channel 1 (3 GHz) and channel 4 (37 GHz) in the latitude zones 20° N/S, 80° N/S, and 85° N/S to analyze the changes of TB data during the whole observation mission. The width of the zones was $\pm 0.1^\circ$ in latitude. The observation date varies from Oct. 15, 2010, to May 20, 2011. We analyze the TB in the daytime (6:00–18:00) and nighttime (0:00–6:00; 18:00–24:00) in the latitude zones 20° N/S. Here, the “hour angle” is used to define the lunar local time by Chan and Zheng [13, 24]. It is calculated from the solar incidence angle, the azimuth angle, and the latitude. The “hour angle” is converted into the “24-hour clock” local time.

The TB data at different latitude and their corresponding local time are shown in Figures 1(a)–1(g). In Figures 1(a)–1(d), we could observe, in low latitude, the changes of TB of channel 4 and channel 1 that are dominated by diurnal variation with lunar local time, although the diurnal variation of channel 1 is smaller than that of channel 4. Because channel 1 signal originates in deeper subsurface layer than channel 4, it is less sensitive to the sunlight and more stable during the lunation period. The effects of topography and physical properties of regolith also cause the vibrations of TB at the same local time, but they are masked by the effects of solar incidence. To extract the physical characteristics of lunar regolith or topography effects, the diurnal variation should be removed, e.g., with spherical harmonics fitting as proposed in [13, 30]. The TB of channel 4 between February and March in daytime is lower than that in nighttime mainly because of the fact that TB in the early morning is lower than that after dusk according to the result by Zheng [30]. The lunar local time of the data observed between February and March is almost around early morning (6:00 am to 8:00 am) and dusk (18:00 pm to 20:00 pm).

In Figures 1(a)–1(d), we also observe that the difference between latitudes 20° N and 20° S is within the range of 5% and the seasonal variations can be barely seen. It can be simply explained by the small obliquity of the Moon and the geographic symmetry. The illumination condition is almost the same between the southern and northern hemispheres in the low latitude area.

When latitude reaches 80° N/S, the ranges of TB diurnal variations largely reduce and are almost the same between channel 1 and channel 4 because of the decreasing solar illumination, as shown in Figure 1(e). TB variations caused by topography and other factors are similar to or even larger than diurnal variation. In high latitude, previously proposed spherical harmonics fitting method has limitations to fit TB variation curves and offset the changes of solar illumination and extract lunar regolith properties [13, 30]. Influences of topographic relief, scattering, and infrared radiation from

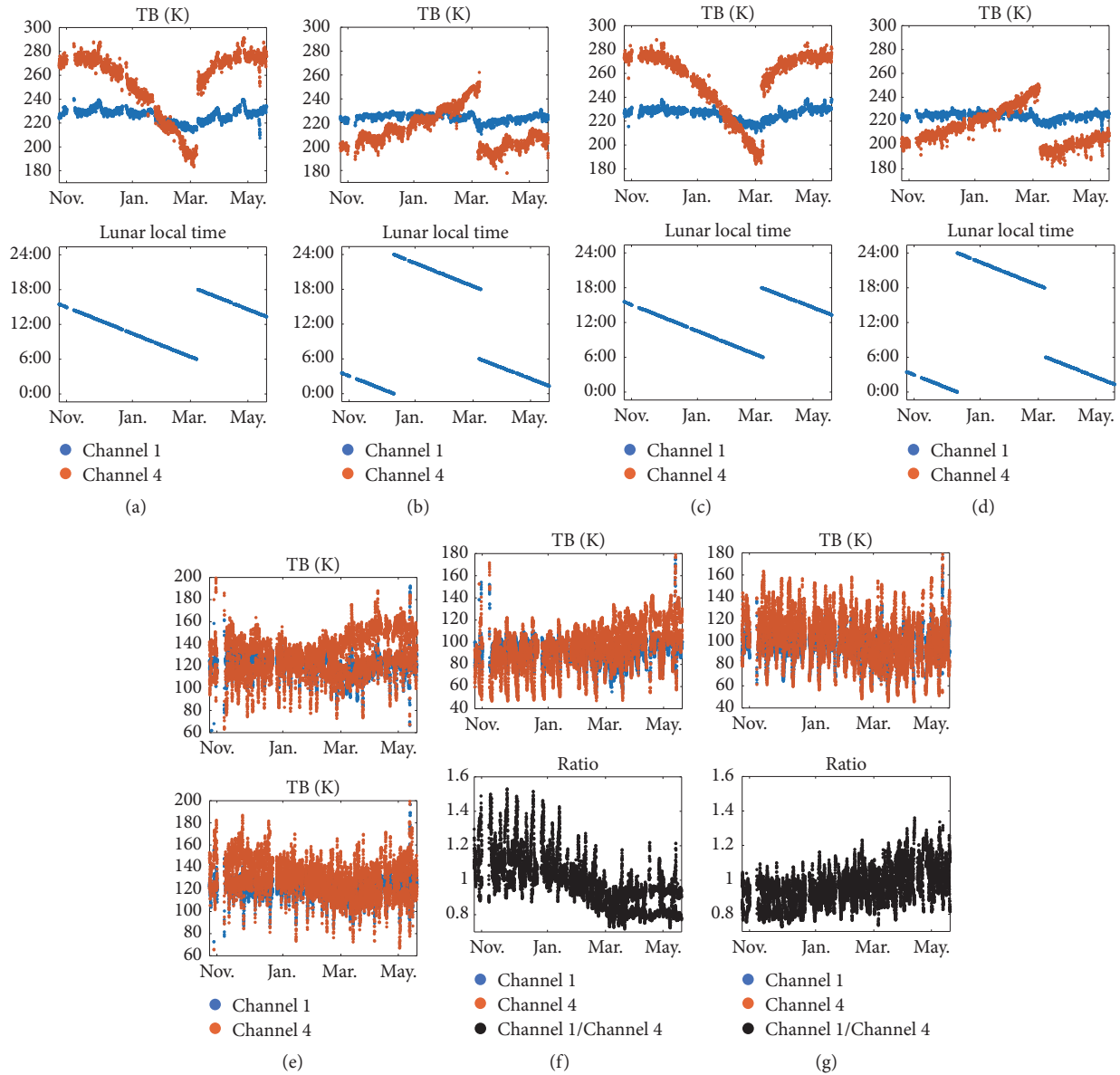


FIGURE 1: The data shown in (a)–(g) is selected in the latitude zones 20° N/S, 80° N/S, and 85° N/S, respectively. The upper part of (a)–(d) represents the fact that the TB of channel 1 and channel 4 varies during the whole observation period in daytime and nighttime at latitude 20° N ((a); (b)) and 20° S ((c); (d)), respectively. The bottom part of (a)–(d) shows the changes of lunar local time converted from “hour angle” of the corresponding TB data. Lunar local time varies with date nearly uniformly, so data diagram represents the TB variations in a half lunation cycle. The data shown in (e) represents the TB variations of channel 1 and channel 4 at 80° N and 80° S from top to bottom. The variations of TB and TB ratio between channel 1 and channel 4 are shown in (f) and (g) at 85° N (f) and 85° S (g) from top to bottom.

distant interior sunlit crater walls, etc., should be considered [34]. The trends of the TB variations in 80° N and 80° S are still almost the same, just like that in the low latitude.

The upper part in Figures 1(f) and 1(g) shows the TB variations at latitudes 85° N and 85° S, and the under part shows the TB Ration (TBR) variations between channel 1 and channel 4. Compared to low latitude area, the daytime and nighttime TB data in 85° N/S are less distinguished.

In addition, TB and TBR variations in 85° N and 85° S show opposite trends, especially the TBR. The TB increases slowly with the date in the north and decreases slowly in

the south as shown in Figures 1(f) and 1(g). The reason for the difference can be explained by the seasonal variations. The seasonal variations of TB in high latitude are recognizable because the seasonal changes of solar flux become comparable to the day and night variations in high latitude, while diurnal variation of solar flux dominates in low latitude regions.

The lunar solar flux on flat surface at different latitude from Oct 15, 2010 (start time of Chang'E-2 MRM data) to Oct 15, 2011, was obtained from the ephemeris as shown in Figure 2. We use the SPICE toolkit [35] with the geometry of

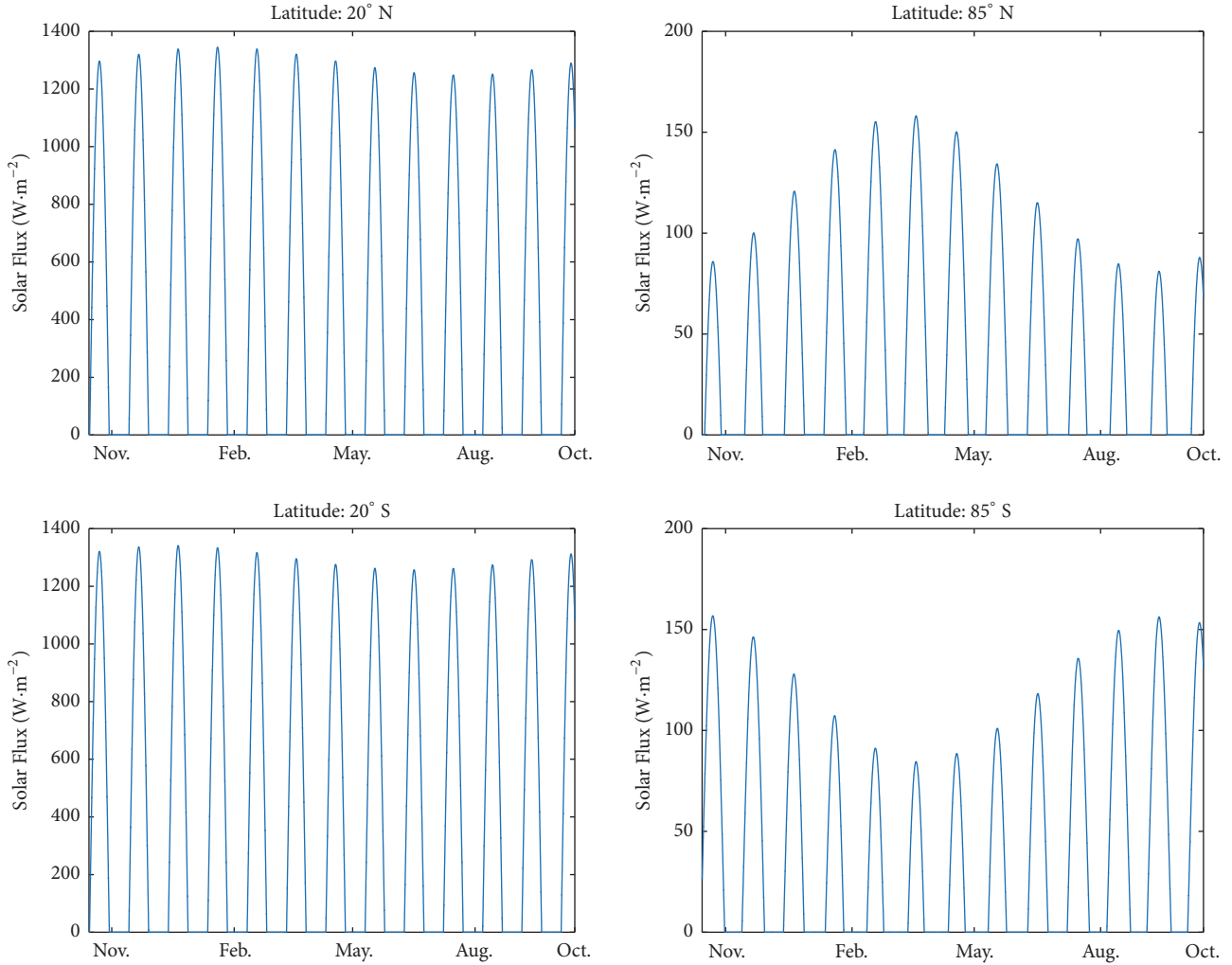


FIGURE 2: The solar flux varies from Oct 15, 2010 (start time of Chang'E-2 MRM data) to Oct 15, 2011, at latitudes $\pm 20^\circ$ and $\pm 85^\circ$.

the Sun obtained from DE421 ephemeris [36] to generate the solar illumination data. The monthly maximum lunar solar flux varies from $158.1 \text{ W}\cdot\text{m}^{-2}$ to $81.1 \text{ W}\cdot\text{m}^{-2}$ at the latitude 85° N and from $156.8 \text{ W}\cdot\text{m}^{-2}$ to $84.5 \text{ W}\cdot\text{m}^{-2}$ at 85° S ; the value varies from $1345.3 \text{ W}\cdot\text{m}^{-2}$ to $1248.2 \text{ W}\cdot\text{m}^{-2}$ at the latitude 20° N and from $1340.8 \text{ W}\cdot\text{m}^{-2}$ to $1257.3 \text{ W}\cdot\text{m}^{-2}$ at 20° S . The relative change of monthly maximum lunar solar flux is larger at high latitude comparing with that in low latitude. This leads to the significant seasonal variations in high latitude and diurnal variation is more recognizable in low latitude.

3.2. TB in PSRs and Non-PSRs of Polar Regions. Figure 3(a) shows the TB and TBR in one of PSRs, Haworth Crater (-1.3° E , 87.5° S), and the Non-PSR regions (150° E , 87.5° S) in the same latitude, marked by the two green circles in the upper part of Figure 3(a). Figure 3(b) provides another comparison between PSR Amundsen Crater (92.3° E , 83.7° S) and the Non-PSR region (105° E , 83.7° S) in the same latitude. The center latitude and longitude of footprint of microwave radiometer are selected within 0.25° to reduce contamination from Non-PSR regions.

The time coverage of the MRM data in observation region is not enough to show clear diurnal variation. As shown in Figures 3(a) and 3(b), the range of TB variations of channels 1 and 4 in PSRs is not smaller than that in non-PSRs, although PSRs do not receive direct sun illumination and channel 1 TB is less sensitive to sun light than channel 4 TB due to different skin depth. It means that the scattering flux and thermal radiation play an important role in determining TB in PSR. Another difference between PSRs and Non-PSRs is the changes of TBR. The TBR increases rapidly with date in PSRs while that almost stays the same in Non-PSRs. The PSRs show an obvious seasonal variation. The maximum TBR during the observation period in PSR is higher than those in non-PSRs in the same latitude. Other comparisons between PSRs and non-PSRs show similar results.

Although PSRs do not receive direct sun light, they are still illuminated by the scattering flux and thermal radiations from neighboring topography [34, 37], which have seasonal variations at high latitude as shown in Figure 2. In addition, the solar flux in PSR is much weaker than that in Non-PSR due to topography relief, leading to much lower TB which

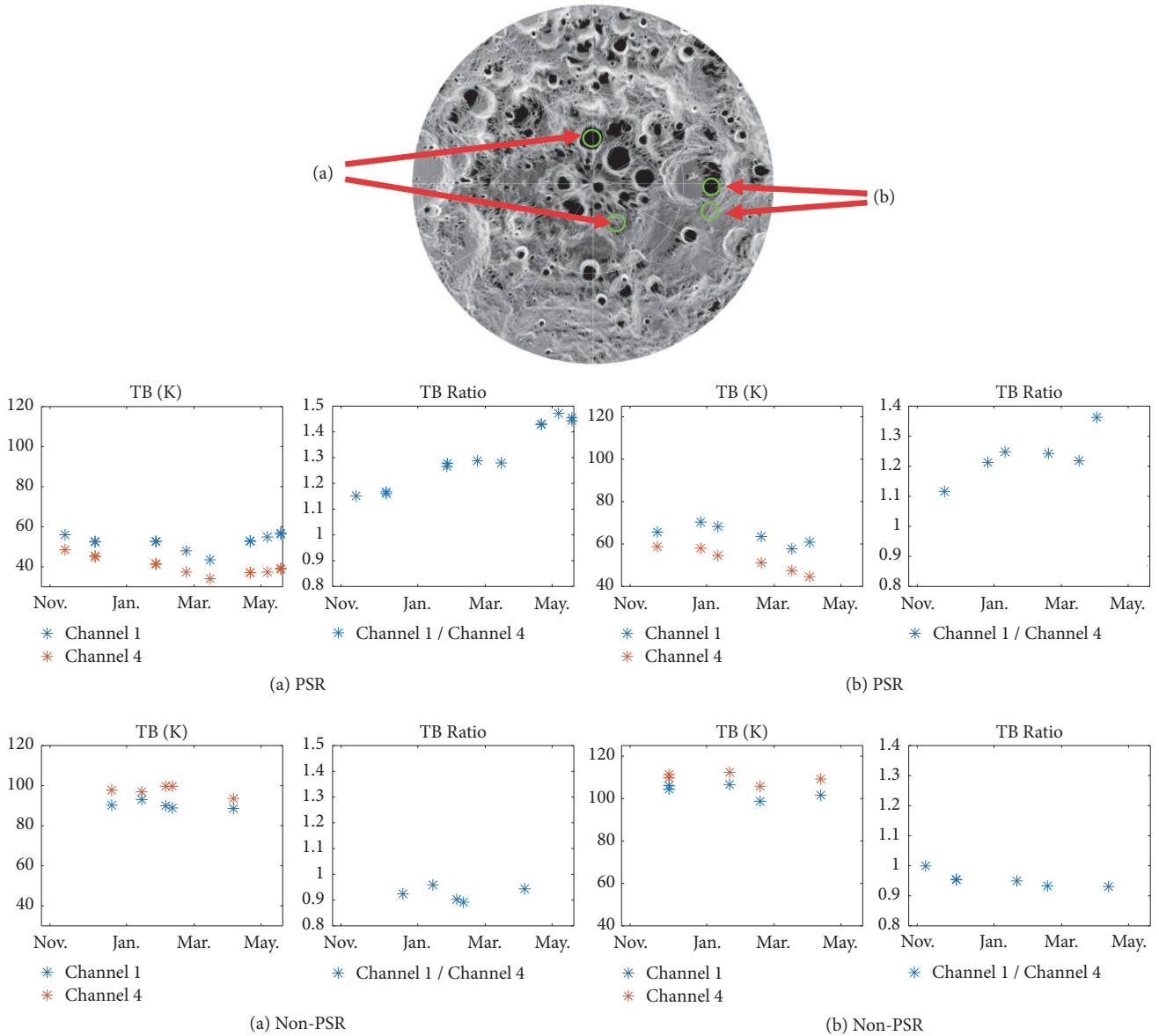


FIGURE 3: TB and TBR variations in Haworth Crater (PSR crater: -1.3° E, 87.5° S) and Non-PSR crater (150° E, 87.5° S) in the same latitude of Polar Regions; (b): TB and TBR variations in Amundsen Crater (PSR crater: 92.3° E, 83.7° S) and Non-PSR crater (105° E, 83.7° S) in the same latitude. The data is selected during the whole observation period. The green circles in the base map show the regions we selected. The base map is the Diviner annual maximum temperature map that varies from 30 K (black) to 345 K (white) in the Polar Regions (<https://ode.rsl.wustl.edu/moon/indexDatasets.aspx>).

is more sensitive to fluctuation of solar flux. Furthermore, although we select PSR with relatively large area to study characteristics of TB, the contamination of Non-PSR is unavoidable due to the large size of the footprint of the CE-2 microwave radiometer, which also contributed to the seasonal variations of TB in PSR. TB in channel 4 shows significant seasonal variations while TB in channel 1 is relative stable due to different penetration depth. Therefore, TBR between channel 1 and channel 4 also shows significant seasonal variations.

3.3. TB in PSR with Plausible Ice Evidence and Other PSRs. We analyzed the TB and TBR data in PSRs with plausible ice

evidence and other PSRs in this section. Except for two large PSR craters mentioned in the previous section, here we select other three large PSR craters with plausible ice evidence and one large PSR crater without water ice observation at present [11, 12], considering the area of the PSR craters and the spatial resolution of CE-2 MRM data [37]. The red dots in the base map present the water ice distribution in the polar regions constrained by M^3 , LOLA, and Diviner [12]. In Figure 4, the green circle in the base map shows the regions we selected.

Even TB values are lower than 100 K in all the observation regions, and TBR of those with plausible water ice could reach some high value such as 1.35, while the TBR varies from about 0.95 to 1.1 in Idel son L Crater, PSR crater without the plausible

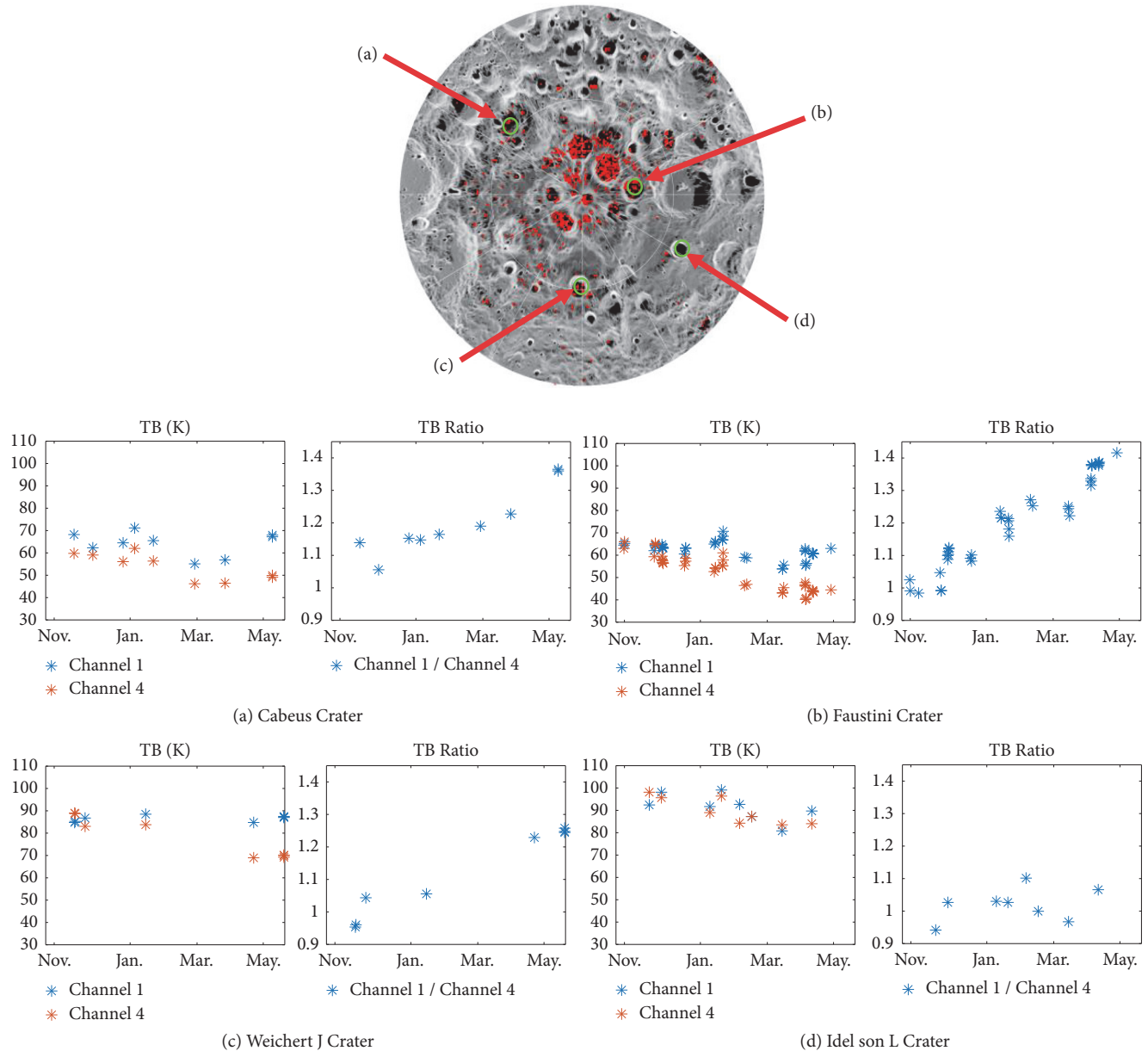


FIGURE 4: The TB and TBR variations during the whole observation period in (a) Cabeus Crater, (b) Faustini Crater, (c) Weichert J Crater, and (d) Idel son L Crater. The base map is the Diviner annual maximum temperature map that varies from 30 K (black) to 345 K (white) in the Polar Regions (<https://ode.rsl.wustl.edu/moon/indexDatasets.aspx>). The red dots in the base map present the water ice distribution in the polar regions constrained by M^3 , LOLA, and Diviner [12]. The green circle in the base map shows the regions we selected.

ice evidence. The TBR reflects the TB differences between channel 1 and channel 4. Microwave signals in channel 1 and channel 4 originate from several meters and several centimeters depth of the lunar regolith, respectively. We could observe that high TBR resulted by relatively stable channel 1 TB and low channel 4 TB, which is easily affected by direct or indirect solar illumination and decreases with largely reduced solar flux in PSRs.

After measuring TBR of MRM data within 80° latitudes, the maximum value is below 1.35, which is selected as a threshold to generate high TBR distribution map as shown in Figures 5(a) and 5(b) to analyze if there is any correlation

between the high TBR value distribution and water ice distribution constrained by other remote sensing data in the polar regions.

Figure 5 shows high MRM ratio value distribution maps, comparing with result using M^3 data by Li et al. [12]. In addition, Hayne et al. also found a high value of the off/on albedo ratio in Haworth crater and Faustini crater using the LAMP datasets, and the high value of the ratio represents the existence of the water ice [11]. Elphic et al. discovered high concentration of hydrogen in Haworth crater, Shoemaker crater, and Faustini crater using the LP neutron spectrometer data [38]. These craters are all PSR craters and they are

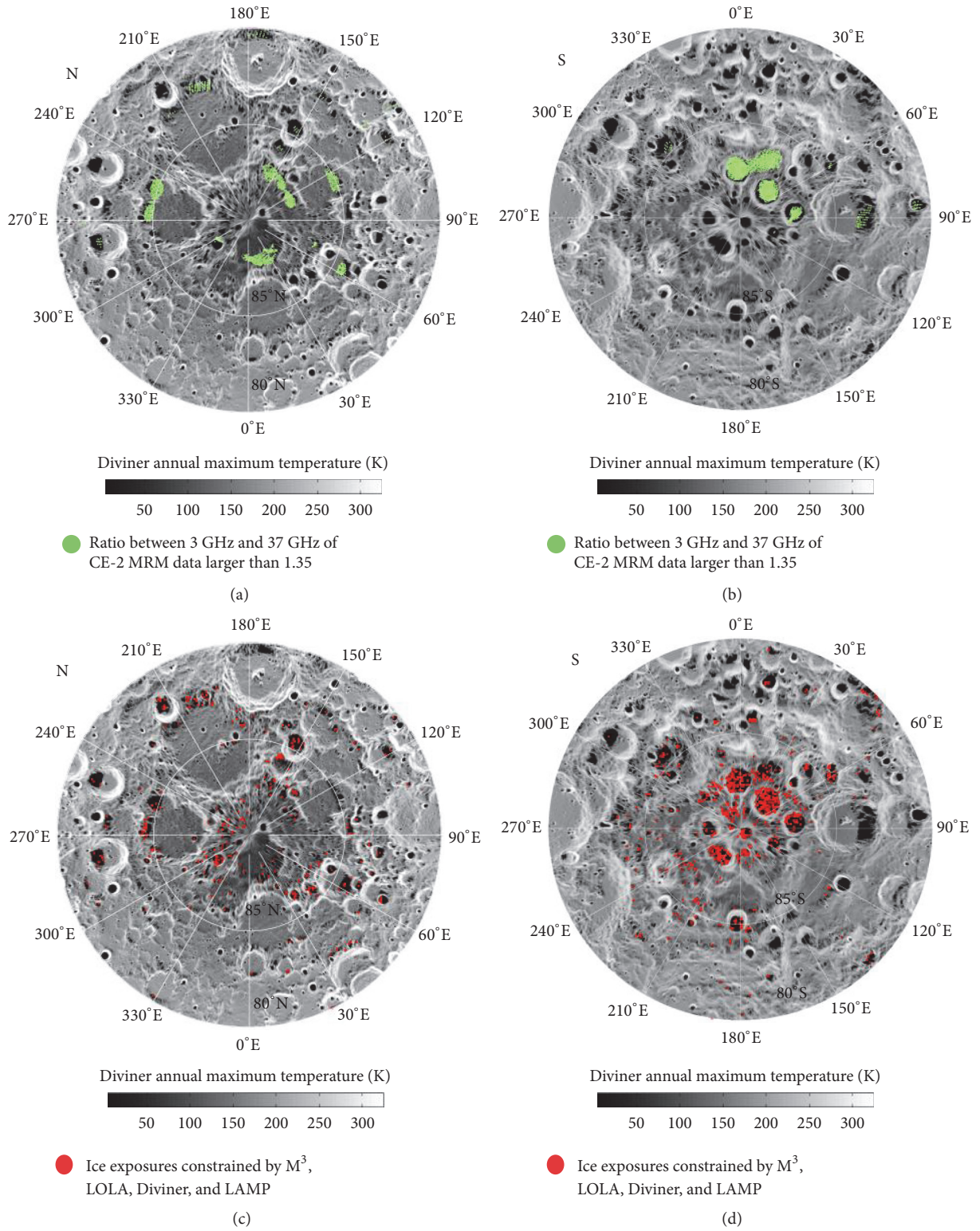


FIGURE 5: ((a) and (b)) Distribution of the ratio scattering points where it is no less than 1.35 overlain on the Diviner annual maximum temperature for the northern (a) and southern (b) polar regions; ((c) and (d)) Distribution of the water-ice-bearing pixels constrained by M³, LOLA, and Diviner, overlain on the Diviner annual maximum temperature for the northern (c) and southern (d) polar regions [12].

potential places where water ice might exist. As we can see from Figure 5, the result using CE-2 MRM data has a good consistence with other instruments data to some extent.

The green dots indicating high TBR shown in Figures 5(a) and 5(b) are mainly concentrated in the dark areas where the temperature is lower than 100K, just like the results in (c) and (d), but not appearing in all the PSRs. Figures 5(a) and 5(c) show the distribution map in the northern polar region. Li gave an example in northern polar region where they got the direct evidence of the surface exposed water ice [12]. M^3 spectra data of Rozhdestvenskiy crater in the northern polar region implies that the surface exposed water ice could exist. The result of CE-2 MRM data in Rozhdestvenskiy crater also showed high ratio between 3 GHz and 37 GHz TB. There are some places that show different results. In Plaskett crater (180°E, 80°N), the top edge of Figures 5(a) and 5(c), no evidence from M^3 spectra data shows the existence of water ice, but CE-2 MRM data show high ratio there.

Figures 5(b) and 5(d) show the distribution maps in southern polar region. As we can see in the figure, high ratio of MRM (b) and the signature of water ice from M^3 all appear in the PSR areas. LAMP [11] and LP neutron spectrometer [38] showed the same results as well. For example, MRM data shows high TBR in the Cabeus crater (315°E, 84.5°S) where the water ice has been proved to be existing after the LCROSS impact experiment, so do the other three instruments which present the signature of water ice in this region. Some different results also appear among these data. LAMP shows low off/on albedo ratio in Shoemaker crater (48°E, 88°S) which means the low probability of the existence of the water ice. But high TBR of MRM and evidence of the water ice from M^3 and LP neutron spectrometer all present in this crater. High TBR of MRM and signature of water ice after analyzing data of LAMP and LP neutron spectrometer appear in the right part of Amundsen crater (90°E, 83.5°S), but the M^3 instrument shows different result. All the instruments present the signature of water ice in De Gerlache crater (270°E, 88.2°S) except that TBR value does not reach the threshold, which is 1.27.

To obtain the quantity value of the correlation between the water ice distribution retrieved from M^3 data [12] and distribution of TBR where it is no less than 1.35 in polar regions (80° N/S-90° N/S), we calculate the proportion of the summation over area with the M^3 data in the regions of interest for south pole and north pole, respectively.

The Chang'E-2 (TBR \geq 1.35) and M^3 data in the study area are collected in 15 \times 15 km² bins. The boundaries of the disks in Figures 5(a)–5(d) are within the 80° latitude circle. The conditional correlation is defined as $C = N_{M^3 \cap CE-2} / N_{CE-2}$, N_{CE-2} which denotes the summation of the bins where TBR is no less than 1.35, and $N_{M^3 \cap CE-2}$ denotes the summation of the bins where TBR is no less than 1.35; M^3 data with water ice proof exists. The results are 0.74 and 0.56 in south and north poles, respectively. Amundsen crater is considered as place with water ice since evidence was provided by LP neutron spectrometer and LAMP, but M^3 data indicates that no water ice exists here. If we consider the Amundsen crater as the case with water ice, the results are 0.89 and 0.56 in

south pole and north pole, respectively. Note that only the regions where the TBR is no less than 1.35, not the whole pole regions, are included in the calculation to minimize the impact of the “irrelevant” areas with no water ice. Therefore, high TBR regions are found to coincide well with the water ice deposits areas. For data validation, we use different bin sizes to calculate correlation between M^3 water ice results and our TBR data. Changing the bins into 25 \times 25 km², the conditional correlation is 0.74 and 0.76 in south and north poles considering the Amundsen crater without water ice. The results still show high correlation between two sets of data, similar to results generated with 15 \times 15 km² bins. The data and the correlation method are validated. The M^3 data that indicates that the water ice exists in the lunar polar region is given by Li [12].

One of the possibilities to explain the correlation between high TBR and water ice deposits could be the fact that water ice deposits are stable in the low temperature environment. Thus, we statistically study high TBR distribution and low TB distribution of channel 4. Based on statistic results, high maximum TBR (\geq 1.35) always appears in the places where TB of channel 4 is lower than 100 K, which also indicates low physical temperature. However, only 1.37% locations with low TB of channel 4 (< 100 K) can reach high maximum TBR. Hence, in addition to low temperature, obtaining high maximum TBR has other requirements such as the fact that area of PSR is larger than certain threshold, which is related with MRM data spatial resolution. Another scenario is that in regions with plausible water ice proof channel 4 TB usually is lower than channel 1 TB, which indicates low mobility of water molecules in these regions so that water molecules deposits will not diffuse below the surface and can be detected by remote sensing experiments at the surface of the Moon such as the imaging spectrometer M^3 [39]. Other speculations of such correlation include the fact that the presence of water ice deposits changes the average physical properties of lunar regolith, e.g., thermal inertia, dielectric constant, which results in large TB variations at different depths. Simulation of TB with physical parameters of lunar regolith and accurate solar flux in PSRs is necessary to provide proof for such speculation; however, the difficulty in obtaining the thermophysical parameters of lunar regolith at extreme low temperature and unknown rock abundance, etc., would result in the uncertainties of results [40]. Whether the temperature resolution of MRM data is enough to detect the presence of ice deposits is also questionable.

4. Conclusions

The comparisons of the TB variations in different latitudes show that the periodic diurnal variation of TB is dominant in the low latitude and becomes weak in the polar region. Second, in polar region, the topographical influences cause significant TB variations and seasonal effects are recognizable due to the weak illumination and the small obliquity of the Moon. Therefore, previous TB normalization method for latitude and local time is no longer suitable for polar regions. Third, even without the direct sun illumination, obvious seasonal variations of TBs are observed in PSRs,

probably caused by the scattering flux and thermal radiations from neighboring topography. Fourth, TBR between channel 1 and channel 4, which indicates TB variation at different depths of lunar regolith, shows stronger seasonal variation in PSR than others in the same latitude. Also, TBR in the PSRs with plausible water ice evidence could reach relatively high value. Overall, the distribution of high TBR is in good consistence with potential water ice distribution obtained by other types of equipment, e.g., LAMP, LP, and M³. The areas with anomaly high value of TBR mainly appear in PSRs, such as Haworth crater, Shoemaker crater, Faustini crater, and Cabeus Crater where ice water most likely exists according to remote sensing data, but not vice versa.

The correlation between distribution of high TBR and plausible water ice proofs could be due to the low temperature environment indicated by high TBR. However, high TBR implies other conditions such as large PSR area. It also means that temperature of the surface is lower than that several meters deeper, which keeps water molecules on the surface instead of diffusing to the subsurface layers.

Data Availability

The data used to support the findings of this study are available from the corresponding author upon request.

Conflicts of Interest

The authors declare that they have no conflicts of interest.

Acknowledgments

This work is supported by Macao Science and Technology Development Fund in Macao Special Administrative Region: 0042/2018/A2 and 0089/2018/A3. The Chang'E data was supported by National Astronomical Observatories, Chinese Academy of Sciences. The authors would like to thank Li Shuai from University of Hawaii who provided the water ice distribution map generated with M³ data. They also thank Dr. Xiongyao Li from Institute of Geochemistry of Chinese Academy of Sciences for the valuable comments and suggestions.

References

- [1] K. Watson, B. C. Murray, and H. Brown, "The behavior of volatiles on the lunar surface," *Journal of Geophysical Research*, vol. 66, no. 9, pp. 3033–3045, 1961.
- [2] N. J. S. Stacy, D. B. Campbell, and P. G. Ford, "Arecibo radar mapping of the lunar poles: a search for ice deposits," *Science*, vol. 276, no. 5318, pp. 1527–1530, 1997.
- [3] D. B. Campbell, B. A. Campbell, L. M. Carter, J.-L. Margot, and N. J. S. Stacy, "No evidence for thick deposits of ice at the lunar south pole," *Nature*, vol. 443, no. 7113, pp. 835–837, 2006.
- [4] S. Nozette, C. L. Lichtenberg, P. Spudis et al., "The Clementine bistatic radar experiment," *Science*, vol. 274, no. 5292, pp. 1495–1498, 1996.
- [5] R. A. Simpson and G. L. Tyler, "Reanalysis of Clementine bistatic radar data from the lunar South Pole," *Journal of Geophysical Research: Planets*, vol. 104, no. E2, pp. 3845–3862, 1999.
- [6] P. D. Spudis, D. B. J. Bussey, S. M. Baloga et al., "Evidence for water ice on the moon: results for anomalous polar craters from the LRO Mini-RF imaging radar," *Journal of Geophysical Research: Planets*, vol. 118, no. 10, pp. 2016–2029, 2013.
- [7] W. Fa and Y. Cai, "Circular polarization ratio characteristics of impact craters from Mini-RF observations and implications for ice detection at the polar regions of the moon," *Journal of Geophysical Research: Planets*, vol. 118, no. 8, pp. 1582–1608, 2013.
- [8] W. C. Feldman, S. Maurice, A. B. Binder, B. L. Barraclough, R. C. Elphic, and D. J. Lawrence, "Fluxes of fast and epithermal neutrons from lunar prospector: evidence for water ice at the lunar poles," *Science*, vol. 281, no. 5382, pp. 1496–1500, 1998.
- [9] W. C. Feldman, D. J. Lawrence, R. C. Elphic et al., "Chemical information content of lunar thermal and epithermal neutrons," *Journal of Geophysical Research: Planets*, vol. 105, no. E8, pp. 20347–20363, 2000.
- [10] A. Colaprete, P. Schultz, J. Heldmann et al., "Detection of water in the LCROSS ejecta plume," *Science*, vol. 330, no. 6003, pp. 463–468, 2010.
- [11] P. O. Hayne, A. Hendrix, E. Sefton-Nash et al., "Evidence for exposed water ice in the Moon's south polar regions from Lunar Reconnaissance Orbiter ultraviolet albedo and temperature measurements," in *Proceedings of the Annual Meeting of the Lunar Exploration Analysis Group*, vol. 1820, Laurel, MD, USA, 2014.
- [12] S. Li, P. G. Lucey, R. E. Milliken et al., "Direct evidence of surface exposed water ice in the lunar polar regions," *Proceedings of the National Academy of Sciences of the United States of America*, vol. 115, no. 36, pp. 8907–8912, 2018.
- [13] K. L. Chan, K. T. Tsang, B. Kong, and Y.-C. Zheng, "Lunar regolith thermal behavior revealed by Chang'E-1 microwave brightness temperature data," *Earth and Planetary Science Letters*, vol. 295, no. 1-2, pp. 287–291, 2010.
- [14] R. H. Dicke, "The measurement of thermal radiation at microwave frequencies," in *Classics in Radio Astronomy*, pp. 106–113, Springer, Dordrecht, Netherlands, 1946.
- [15] R. H. Dicke and R. Beringer, "Microwave radiation from the sun and moon," in *Classics in Radio Astronomy*, pp. 218–219, Springer, Dordrecht, Netherlands, 1946.
- [16] S. J. Keihm, "Effects of subsurface volume scattering on the lunar microwave brightness temperature spectrum," *Icarus*, vol. 52, no. 3, pp. 570–584, 1982.
- [17] S. J. Keihm, "Interpretation of the lunar microwave brightness temperature spectrum: feasibility of orbital heat flow mapping," *Icarus*, vol. 60, no. 3, pp. 568–589, 1984.
- [18] S. J. Keihm and M. G. Langseth, "Lunar microwave brightness temperature observations reevaluated in the light of Apollo program findings," *Icarus*, vol. 24, no. 2, pp. 211–230, 1975.
- [19] S. J. Keihm and M. G. Langseth, "Microwave emission spectrum of the moon: mean global heat flow and average depth of the regolith," *Science*, vol. 187, no. 4171, pp. 64–66, 1975.
- [20] S. J. Keihm and J. A. Cutts, "Vertical-structure effects on planetary microwave brightness temperature measurements: Applications to the lunar regolith," *Icarus*, vol. 48, no. 2, pp. 201–229, 1981.
- [21] S. J. Keihm, K. Peters, M. G. Langseth, and J. L. Chute Jr., "Apollo 15 measurement of lunar surface brightness temperatures: thermal conductivity of the upper 1 1/2 meters of regolith," *Earth and Planetary Science Letters*, vol. 19, no. 3, pp. 337–351, 1973.

- [22] D. D. Morabito, W. Imbriale, and S. Keihm, "Observing the moon at microwave frequencies using a large-diameter deep space network antenna," *IEEE Transactions on Antennas and Propagation*, vol. 56, no. 3, pp. 650–660, 2008.
- [23] Y. Zheng, Z. Ouyang, C. Li, J. Liu, and Y. Zou, "China's lunar exploration program: present and future," *Planetary and Space Science*, vol. 56, no. 7, pp. 881–886, 2008.
- [24] Y. Zheng, K. Tsang, K. Chan, Y. Zou, F. Zhang, and Z. Ouyang, "First microwave map of the Moon with Chang'E-1 data: the role of local time in global imaging," *Icarus*, vol. 219, no. 1, pp. 194–210, 2012.
- [25] W. Fa and Y. Jin, "Analysis of microwave brightness temperature of lunar surface and inversion of regolith layer thickness: primary results of Chang-E 1 multi-channel radiometer observation," *Science in China Series F: Information Sciences*, vol. 53, no. 1, pp. 168–181, 2010.
- [26] X. Gong, D. A. Paige, M. A. Siegler, and Y.-Q. Jin, "Inversion of dielectric properties of the lunar regolith media with temperature profiles using chang'e microwave radiometer observations," *IEEE Geoscience and Remote Sensing Letters*, vol. 12, no. 2, pp. 384–388, 2015.
- [27] Z. Meng, G. Yang, J. Ping, Z. Cai, A. Gusev, and E. M. Osei, "Influence of (FeO+TiO₂) abundance on the microwave thermal emissions of lunar regolith," *Science China Earth Sciences*, vol. 59, no. 7, pp. 1498–1507, 2016.
- [28] R. Bugiolacchi, G. Hu, and K. L. Chan, "A new look at the Moon using Chang'e-2 microwave radiometer data," in *Proceedings of the European Planetary Science Congress*, vol. 12, Berlin, Germany, 2018.
- [29] Z. Meng, S. Hu, T. Wang, C. Li, Z. Cai, and J. Ping, "Passive microwave probing mare basalts in mare imbrium using CE-2 CELMS data," *IEEE Journal of Selected Topics in Applied Earth Observations and Remote Sensing*, vol. 11, no. 9, pp. 3097–3104, 2018.
- [30] Y. Zheng, K. L. Chan, K. T. Tsang et al., "Analysis of Chang'E-2 brightness temperature data and production of high spatial resolution microwave maps of the Moon," *Icarus*, vol. 319, pp. 627–644, 2019.
- [31] Z. Z. Wang, Y. Li, X. H. Zhang et al., "Calibration and brightness temperature algorithm of CE-1 Lunar Microwave Sounder (CELMS)," *Science China Earth Sciences*, vol. 53, no. 9, pp. 1392–1406, 2010.
- [32] G.-P. Hu, K. L. Chan, Y.-C. Zheng, K. T. Tsang, and A.-A. Xu, "Comparison and evaluation of the Chang'E microwave radiometer data based on theoretical computation of brightness temperatures at the Apollo 15 and 17 sites," *Icarus*, vol. 294, pp. 72–80, 2017.
- [33] M. A. Siegler and J. Feng, "Microwave remote sensing of lunar subsurface temperatures: reconciling Chang'e MRM and LRO diviner," in *Proceedings of the Lunar and Planetary Science Conference*, vol. 48, The Woodlands, TX, USA, 2017.
- [34] D. A. Paige, M. Siegler A, J. Zhang A et al., "Diviner lunar radiometer observations of cold traps in the Moons south polar region," *Science*, vol. 330, no. 6003, pp. 479–482, 2010.
- [35] C. H. Acton Jr., "Ancillary data services of NASA's navigation and ancillary information facility," *Planetary and Space Science*, vol. 44, no. 1, pp. 65–70, 1996.
- [36] J. G. Williams, "DE421 lunar orbit, physical librations, and surface coordinates," 2008, ftp://ssd.jpl.nasa.gov/pub/eph/planets/ioms/de421.Moon_coord_iom.pdf.
- [37] E. Mazarico, G. A. Neumann, D. E. Smith, M. T. Zuber, and M. H. Torrence, "Illumination conditions of the lunar polar regions using LOLA topography," *Icarus*, vol. 211, no. 2, pp. 1066–1081, 2011.
- [38] R. C. Elphic, V. R. Eke, L. F. A. Teodoro, D. J. Lawrence, and D. B. J. Bussey, "Models of the distribution and abundance of hydrogen at the lunar south pole," *Geophysical Research Letters*, vol. 34, no. 13, 2007.
- [39] R. O. Green, C. Pieters, P. Mouroulis, and T. Koch, "The Moon Mineralogy Mapper (M3) imaging spectrometer for lunar science: instrument description, calibration, on-orbit measurements, science data calibration and on-orbit validation," *Journal of Geophysical Research: Planets*, vol. 116, no. E10, 2011.
- [40] R. Woods-Robinson, M. A. Siegler, and D. A. Paige, "Developing a new thermophysical model for lunar regolith soil at low temperatures," in *Proceedings of the AGU Fall Meeting Abstracts*, San Francisco, Calif, USA, 2016.